DISCRETE-TIME QUANTUM WALK OF A BOSE-EINSTEIN CONDENSATE IN MOMENTUM SPACE

By

SIAMAK DADRASMARANI

Bachelor of Science in Physics

K.N. Toosi University of Technology

Tehran, Iran

2002

Master of Science in Photonics

Shahid Beheshti University

Tehran, Iran

2005

Submitted to the Faculty of the

Graduate College of the

Oklahoma State University

in partial fulfillment of

the requirements for the degree of

DOCTOR OF PHILOSOPHY

May, 2018

DISCRETE-TIME QUANTUM WALK OF A BOSE-EINSTEIN CONDENSATE IN MOMENTUM SPACE

Dissertation Approved by:

Professor Gil S. Summy

Dissertation Advisor

Professor Albert T. Rosenberger

Commitee Member

Professor Mario F. Borunda

Commitee Member

Professor Eric Abraham

Commitee Member

Professor James E. Stine

Outside Commitee Member

Acknowledgments [1]

First and foremost, I would like to thank my outstanding adviser Professor Gil Summy for his invaluable instructions throughout the course of my PhD. His insights, encouragement, support, and friendship have been a great source of inspiration for this work. His immense knowledge on atomic physics had helped me a lot in generating new ideas and implementing them. By challenging me and expecting more from me, Gil shaped my professional identity and built confidence in me. He has supported me through every research endeavor, and he has taught me to be a critical and sincere researcher. Thank you Gil for your generous support and guidance.

I am also grateful to my graduate committee menbers, Dr. Albert Rosenberger, Dr. Mario Borunda, Dr. Eric Abraham (OU) and Dr. James Stine for all their help and support. I would like to express my sincere gratitude to my collaborator, Dr. Sandro Wimberger, in University of Heidelberg, Germany. It was a fruitful collaboration with him and his students, Alexander Gresch and Caspar Groiseau.

I am proud to have been a part of BEC and Quantum Chaos group at OSU for its great research environment and wonderful colleagues who I interacted with. I must thank past and present members of this group, Jiating Ni, Wakun Lam, Amruthaa Sundararaj, and Jarry Clark, not just for their technical feedback but also for their friendly support and assistance.

I would like to extend my sincere thanks to the nicest staff of the Department of Physics. Susan, Alisha, Beth, Charles, and former members, Sandra and Tamra always worked in favor of students and were the friendliest staff I ever met. My thanks also go to the technical staff of Physics Department, Larry, Charles, Warren, Wes, Randy, and Garry. I would also like to acknowledge Melissa Edwards, the undergraduate lab coordinator, for her kindest cooperation during the tight schedules.

Last but not the least, thanks to my family and my amazing parents for their love, encouragement, and support to lift me over obstacles. You are far away, but I have always felt you here with me. I thank my beautiful wife Dr. Samira Ataei for her patience during the course of my PhD. Samira, you are the reason behind this accomplishment and the stimuli to this emission! Thank you for your endless love and support.

[1] Acknowledgements reflect the views of the author and are not endorsed by committee members or Oklahoma State University.

Name: SIAMAK DADRASMARANI

Date of Degree: MAY 2018

Title of Study: DISCRETE-TIME QUANTUM WALK OF A BOSE-EINSTEIN CONDENSATE IN MOMENTUM SPACE

Major Field: PHOTONICS

Abstract: Randomness is the essence of many processes in nature and human society. It can provide important insights into phenomena as diverse as disease transmission, financial markets, and signal processing. Quantum randomness is intrinsically different from classical stochasticity since it is affected by interference and entanglement. Quantum walks profit from the entanglement that is built up between a walker's position and the "coin" degree of freedom that determines the direction of a walker's motion. This entanglement makes quantum walks promising candidates for the implementation of quantum computational algorithms and as a detector of quantum behavior. While several proof-of-principle quantum walk experiments have recently been implemented, the walk scheme we demonstrate here involves the synthesis of the atom-optics kicked rotor with the dynamics of a state selective ratchet realized with a Bose-Einstein condensate. Here we present a discrete-time quantum walk that uses the momentum of ultra-cold rubidium-87 atoms as the walk space and two internal atomic states as the coin degree of freedom. To implement each step of the walk, i.e. a coin toss followed by a unitary shift operator, we use a microwave pulse, which produces a superposition of two internal states, and a resonant quantum ratchet, which entangles the internal and external degrees of freedom. Our quantum ratchet, whose direction at each step depends on the result of the coin toss, is realized by the atom-optics kicked rotor. We demonstrate the principle features of a standard quantum walk, contrasting them to the behavior of a classical walk. In addition, by manipulating either the walk or coin operator we show how the walk dynamics can be biased or reversed. Furthermore, we show the quantum-to-classical transition in our walk, via randomizing the mixing between the two internal states during each coin toss. Our walk offers distinct advantages arising from the robustness of its dynamics in momentum space, extendability to higher dimensions, and possible dependence on many-body correlations.

Contents

List of Figures

List of Tables

Chapter 1

Introduction

The idea that computational devices based on the laws of quantum mechanics can be more powerful than those based on classical mechanics has been around for more than three decades [1, 2]. Widespread research has been performed on quantum computation algorithms after the discovery by Shor that a quantum computer could factor numbers exponentially faster than could be done on a classical computer [3]. Since then, several attempts have been made to find new quantum algorithms which are more effective than their classical counterparts, yet physically feasible with existing technologies. One major direction of research, followed in this regard, involves looking at effective classical algorithmic techniques, and trying to adapt them to quantum computation [4]. For instance, Grover has devised an algorithm which can, in principle, search an unsorted database quadratically faster than any classical algorithm [5]. Another promising feature of a quantum walk on a hypercube, namely an exponentially faster hitting time as compared to a classical random walk, has been found (numerically) by Yamasaki $et\ al.$ [6] and (analytically) by Kempe [7].

Classical random walks play a key role in modeling stochastic processes and represent a basic component of diffusion phenomena and nondeterministic motion. Hence it is not surprising that they have broad application in various fields as diverse as astronomy, solid-state physics, polymer chemistry, and biology to mathematics and computer science [8, 9]. For a review of the theory and applications for classical random walks, see for example Barber and Ninham [10]. Quantum walks are the quantum mechanical analogs of the classical random walk process, describing the propagation of quantum particles on periodic potentials [11, 12, 13]. While the basic procedure for producing a quantum random walk can be outwardly similar to its classical counterpart, the dynamics of a quantum walk are com-

pletely different and can lead to applications unavailable classically. Unlike classical objects, particles performing a quantum walk can be in a superposition state and take all possible paths through their environment simultaneously, leading to faster propagation and enhanced sensitivity to initial conditions [14]. These properties have generated considerable interest in using quantum walks for the study of quantum dynamics and for quantum information processing [15]. For example, it has been shown theoretically that quantum walks can be a building block in probabilistic algorithms for universal quantum computing [16, 17, 18, 19, 20, 21]. Two distinct models of quantum walk with similar physical behavior were devised: (i) the discrete-time quantum walk [11], in which the particle propagates in discrete steps determined by a dynamic internal degree of freedom, and (ii) the continuous-time quantum walk [12], in which the dynamics is described by a time-independent lattice Hamiltonian.

The walk we describe here is an adoption of the discrete-time classical random walk into the quantum regime, and hence it consists of two degrees of freedom; a space in which the walk takes place, and a "coin" which selects the path of the system through the walker's space [11, 22]. The key concept that differentiates the classical from a quantum walk is that a quantum coin can produce a superposition of two (or more states) and therefore there exists an entanglement between the degrees of freedom in the latter case [23]. Hence the quantum walk can be heavily affected by this entanglement leading to the interference between the multitude of paths that a walker may take to arrive at a given location in the walk space.

Several different experimental quantum walk schemes have either been proposed or implemented. For example, walks have been carried out with atoms [14, 24, 25, 26, 27, 28, 29], ions [4, 30, 31, 32], or photons [33, 34, 35, 36, 37, 38, 39, 40]. As might be expected, the variety of different possible walker species leads to the walks themselves taking on an assortment of different forms. For example, walks with photons are most conveniently done in the time domain [34, 36] or in angular momentum [33], while for atoms and ions the walks are usually performed in spatial [14, 28] or phase [30, 31] degrees of freedom. However, up to now, no experimental realization of a quantum walk has been reported in momentum space which we will argue has several important benefits.

In this work, we implement a robust and controllable discrete walk in momentum space using ultracold ^{87}Rb atoms in a pulsed optical lattice. One of the major benefits of our quantum walk is that it provides straightforward access to both internal and external degrees of freedom of the walker. In our system these degrees of freedom are atomic hyperfine states and the center-of-mass momentum

of the atoms. Each step of our quantum walk consists of a microwave (MW) coin operator $\hat{\mathbf{M}}$ which produces a superposition of two internal states, followed by a unitary shift operator $\hat{\mathbf{T}}$ which entangles the internal and external degrees of freedom ($\hat{\mathbf{U}}_{step} = \hat{\mathbf{T}}\hat{\mathbf{M}}$). Our shift operator is a quantum ratchet derived from the atom-optics kicked rotor (AOKR), a system that has been the backbone of quantum chaos experiments for many years [41, 42, 43, 44, 45, 46, 47, 48, 49, 50, 51, 52].

Another advantage of our momentum-based quantum walk is that it can be extended to higher dimensions. Multi-dimensional walks could be implemented using lattices with more than a single spatial dimension, or perhaps more straightforwardly, by the introduction of additional spatial frequency components to the 1-dimensional lattice which is the basis of the momentum shift operator. Our current setup allows for a realization of discrete walks up to 20 steps which compares favorably with those achieved in other implementations. However, this can be improved further by relatively minor changes to our atom detection system so that a wider range of momenta can be observed. With our current experiment we can clearly differentiate between classical and quantum walks, and can observe the quantum-to-classical transition [53, 54] by applying noise to one or both degrees of freedom.

We can also steer the direction of the walks by manipulating either the internal or external degrees of freedom [23, 55, 56, 57]. For example, the composition of the hyperfine state superposition at each coin toss, or the relative strength of the atom-light interaction with the hyperfine levels, both provide a way of steering the walk. The controllability that we achieve is a direct consequence of implementing the walk with an atomic system in momentum space. Another distinct control feature of our quantum walk is its reversibility arising from the entanglement between the internal and external degrees of freedom. We show that, since the quantum walk evolves coherently and unitarily, it is possible to manipulate the walk operators to reverse all steps and recover the initial state of the system. This feature may have applications in atomic interferometers [26, 27, 33, 58, 59] and quantum-state search algorithms (using the coin to manipulate the momentum distribution) [5, 60, 61]. Furthermore we implement our quantum walks using a Bose-Einstein condensate (BEC) which, unlike the single-particle systems [28, 30, 31, 35], can be extended to realize many-body walks by taking atom-atom interactions into account. Finally, a recent proposal has described how our quantum walks can provide a platform for the realization of topological phases [62, 63].

Our experimental realization of the quantum walk was founded based on the ^{87}Rb BEC. Thus we begin Chapter 2 with an overview of the theory of Bose-Einstein condensation and a detailed discussion

on the magneto-optical trap (MOT) and evaporative cooling techniques to realize the BEC.

In Chapter 3 we elaborate the discrete-time quantum walk by highlighting the key aspects that differentiate this walk from its classical version. We describe in detail the two components of the walk space, the internal and external degrees of freedom, and show how the walk takes place by repeatedly applying the coin and unitary shift operators, each addressing either of these degrees of freedom. We present the theoretical building blocks of the quantum walk and show how we use AOKR-based quantum resonant ratchets and MW pulses to realize the desired operators of the walk. We finish this chapter by describing the sequence of the operators to achieve the standard quantum walk as well as the walk reversal.

Details of our experimental setup to implement the quantum walk experiments are described in Chapter 4. This chapter starts with demonstrating various configurations on the "Laser Table" including the optical setups for preparing the frequency-stabilized MOT, Doppler cooling, imaging, and re-pump laser beams. Then it continues with the "BEC Table" with a detailed description on several different configurations set on this table. These include the setup for completing the MOT process, the CO_2 laser system for evaporative cooling, vacuum chamber and magnetic coils, kicking and imaging optical setups, and finally the MW setup. Details of the BEC creation process are also elaborated in this chapter.

In Chapter 5, we present the results of various experiments on the quantum walks and support our findings with simulation and theoretical discussions. We start with demonstrating the standard quantum walks and investigating the effects of various experimental parameters and limits on the behavior of the walk. We also elaborate the steered quantum walks and show how direction of the walk can be controlled by manipulating either internal or external degrees of freedom. Then we continue with the realization of quantum walk (and ratchet) reversals and show how the reversal and the system recovery can be limited by the qualitative features of the initial state of the system. We finish this chapter with our findings on the quantum-to-classical transition as a result of the noise enhancement in the walk process.

Finally, we conclude in Chapter 6 with a brief recap on our findings on the time-discrete quantum walks. We review how the BEC-based implementation of quantum walks in momentum space gives rise to various control features of the walk. We finally wrap up with pointing at some other advantages of our scheme that can be employed in further applications and extensions in multi-dimensional walks or quantum algorithms.

Chapter 2

Bose-Einstein Condensate

2.1 Fundamentals of Bose-Einstein Condensation

Quantum statistics is governed by the principle of indistinguishability of identical particles. Particles with integer spin are called bosons and half integer spins are called fermions. Photons are an example of bosons whereas the elementary particles such as electrons, protons, neutrons, quarks and neutrinos are examples of fermions. Thus an atom with an even number of total constituent particles is a boson. Bosons obey Bose-Einstein statistics in which there is no restriction on the occupation number of any single-particle state. However in the case of fermions, no more than one particle can occupy any single-particle state (Pauli's exclusion principle [64]). Moreover the many-body wave function of identical bosons is symmetric under the exchange of any two bosons. For identical fermions, such an exchange is anti-symmetric.

The possibility of accumulating a large fraction of bosons in a single quantum state makes the BEC a suitable choice for the realization of various quantum phenomena. This is because of the fact that the BEC displays quantum behavior on a macroscopic scale. More precisely, in a typical BEC $\sim$100,000 atoms can be encapsulated in the lowest energy level with sharing (approximately) the same wavefunction [65]. This helps one to easily trace an ensemble of atoms with a measurable size that behaves similar to a single atom.

The grand partition function, Ξ, of a system of particles with particle-number operator $\hat{N}$ and the Hamiltonian $\hat{H}$ is given by [66]:

$$\Xi = \mathrm{Tr}\ e^{-\beta'(\hat{H}-\mu\hat{N})}, \tag{2.1}$$

where $\beta' = 1/(k_B T)$ with k_B and T the Boltzman constant and temperature respectively, and μ is the chemical potential which serves as the Lagrange multiplier. For an ideal Bose gas (i.e. noninteracting identical bosons) with the dispersion relation $\epsilon_k = \hbar^2 k^2/2M$ one can write

$$\hat{H} - \mu\hat{N} = \sum_k (\epsilon_k - \mu)\hat{n}_k, \tag{2.2}$$

where $\hat{n}_k$ is the number operator of a particle with wave vector k. Thus Eq. (2.1) can be written as

$$\Xi = \prod_k \sum_{n_k=0}^{\infty} [e^{\beta'(\mu-\epsilon_k)}]^{n_k}. \tag{2.3}$$

This is a geometric series which converges only if $e^{\beta'(\mu-\epsilon_k)}$ is less than one. It requires $\mu < 0$ provided $\epsilon_k \geq 0$. Then Eq. (2.3) becomes

$$\Xi = \prod_k \frac{1}{1 - e^{\beta'(\mu-\epsilon_k)}}. \tag{2.4}$$

With this grand partition function the thermodynamic potential can be defined as

$$\Omega = -\frac{1}{\beta'} \ln \Xi = \sum_k \frac{1}{\beta'} \ln(1 - e^{\beta'(\mu-\epsilon_k)}). \tag{2.5}$$

This leads to the Bose-Einstein distribution function

$$N = \sum_k \bar{n}_k = \sum_k \frac{1}{e^{\beta'(\epsilon_k-\mu)} - 1}, \tag{2.6}$$

where $\bar{n}_k = -\frac{\partial \Omega_k}{\partial \mu}$ is the average number of particles with wave vector k and N is the average total number of bosons. In the thermodynamic limit in which both the volume V and N are infinitely large, the sum in Eq. (2.6) can be replaced by an integral, i.e. $\sum_k \to \frac{V}{(2\pi)^3} \int \mathrm{d}^3 k$, then Eq. (2.6) becomes

$$\frac{N}{V} = \frac{1}{(2\pi)^3} \int \mathrm{d}^3 k \frac{1}{e^{\beta'(\epsilon_k-\mu)} - 1}. \tag{2.7}$$

If the temperature is reduced maintaining the particle number density, $n = N/V$ a constant, the value of chemical potential increases and becomes zero at some temperature T_c. Substituting $\mu = 0$ and

$\epsilon_k = \hbar^2 k^2/2M$ one obtains

$$n = 2.612 \left(\frac{M k_B T_c}{2\pi\hbar^2} \right)^{3/2}, \tag{2.8}$$

where we have used the formula $\int_0^\infty \frac{x^{a-1}}{e^{x-1}} = \Gamma(a)\xi(a)$. Here $\xi(a)$ is the Riemann zeta function with $\xi(\frac{3}{2}) = 2.612$ and $\Gamma(\frac{3}{2}) = \frac{\sqrt{\pi}}{2}$. Now one can calculate the transition temperature for BEC, which from Eq. (2.8) is

$$k_B T_c = \frac{3.31\hbar^2}{M} n^{2/3}. \tag{2.9}$$

For $T < T_c$, a nonzero fraction of bosons condense into the lowest-energy state. Note that the particles with $\epsilon = 0$ do not contribute to the integral. For $T < T_c$, we can write a quantity called normal fraction as $\frac{N_{\epsilon>0}}{N} = \left(\frac{T}{T_c}\right)^{3/2}$. Thus the fraction of condensate atoms can be written as

$$\frac{N_{\epsilon=0}}{N} = 1 - \left(\frac{T}{T_c} \right)^{3/2}. \tag{2.10}$$

BEC occurs when quantum degeneracy sets in, i.e. when the thermal de Broglie length defined as $\lambda_{dB} = \frac{h}{\sqrt{2\pi M k_B T}}$, of individual bosons begins to overlap. Using this expression for the de Broglie length in Eq. (2.8), the phase space density, ρ, of Bose gas at $T = T_c$ can be written as

$$\rho = n\lambda_{dB}^3 \simeq \left(\frac{\lambda_{dB}}{d} \right)^3 \simeq 2.612. \tag{2.11}$$

This shows that an ideal Bose gas undergoes BEC at a phase space density of 2.612 [67] and that at the transition temperature, the thermal de Broglie length is on the order of the average interparticle distance d. To provide such a condition, since $\rho \propto \frac{1}{T^{3/2}}$, one needs to decrease the temperature below the transition temperature. In addition, since the phase space density is proportional to the number density ($\rho \propto n$), a large number of atoms ($n \sim 10^{13}$) should be provided. In this regard the optical molasses technique can be used to cool the atoms down to ~ 100 μK as described in Section 2.2.1. Then the density can be enhanced and temperature can be reduced further as will be explained in Section 2.2.3 to reach the phase space density required for the BEC.

2.2 Laser Cooling and Trapping

2.2.1 Optical Molasses (Doppler Cooling)

The interaction of atoms with the light field of a laser can cause a force on atoms due to the scattering of photons. The average force is defined as the expectation value of the quantum mechanical force operator,

$$\hat{F} = -\nabla \hat{H}, \tag{2.12}$$

where $\hat{H} = \hat{H}_0 + \hat{H}'(t)$ is the total Hamiltonian of the system with $\hat{H}_0$, the field-free time independent Hamiltonian and $\hat{H}'(t)$, the time dependent interaction Hamiltonian. The expectation value of $\hat{F}$ is given by

$$\langle \hat{F} \rangle = \mathrm{Tr}(\hat{\rho}\hat{F}), \tag{2.13}$$

where $\hat{\rho}$ is the density matrix and its time evolution is given by,

$$\frac{\mathrm{d}\hat{\rho}}{\mathrm{d}t} = -\frac{i}{\hbar}[\hat{H}, \hat{\rho}]. \tag{2.14}$$

Here the operator $\hat{H}_0$ has eigenvalues $E_n = \hbar\omega_n$ and eigenfunctions $\phi_n(\vec{r})$. Also the eigenfunctions are linearly independent forming a complete set. In order to calculate the force on the atoms by the laser field, a good starting point is the solution of the time-dependent Schrödinger equation,

$$\hat{H}\psi(\vec{r}, t) = i\hbar\frac{\partial\psi(\vec{r}, t)}{\partial t}, \tag{2.15}$$

where the wavefunction $\psi(\vec{r}, t)$ can be expanded in terms of $\phi_n(\vec{r})$ as

$$\hat{H}\psi(\vec{r}, t) = [\hat{H}_0 + \hat{H}'(t)]\sum_k c_k(t)\phi_k(\vec{r}). \tag{2.16}$$

Multiplying by $\phi_j^*(\vec{r})$ after applying Eq. (2.16) to Eq. (2.15) and integrating over spatial coordinates $\vec{r}$ one obtains

$$i\hbar\frac{\mathrm{d}c_j(t)}{\mathrm{d}t} = c_j(t)E_j + \sum_k c_k(t)\hat{H}'_{jk}(t), \tag{2.17}$$

where $\hat{H}'_{jk}(t) = \langle\phi_j|\hat{H}'(t)|\phi_k\rangle$. When considering a simple two state atom the problem is known as the Rabi two-level problem [68] and has just two coupled differential equations

$$i\hbar\frac{\mathrm{d}c_g(t)}{\mathrm{d}t} = c_g(t)[E_g + \hat{H}'_{gg}(t)] + c_e(t)\hat{H}'_{ge}(t), \tag{2.18}$$

and

$$i\hbar\frac{\mathrm{d}c_e(t)}{\mathrm{d}t} = c_e(t)[E_g + \hat{H}'_{ee}(t)] + c_g(t)\hat{H}'_{eg}(t). \tag{2.19}$$

The subscripts g and e refer to ground and excited states respectively and $\hat{H}'_{ge} = \hat{H}'^{*}_{eg}$. The interaction term is given by $\hat{H}'_{ge} = -\vec{\mu}.\vec{E}(\vec{r},t)$ [69]. Here $\vec{E}(\vec{r},t)$ is the electric field and $\vec{\mu} = q\langle e|\vec{r}|g\rangle$ is the induced dipole moment of the atom, where q is the electronic charge, and $\vec{r}$ is the position. Also due to the odd parity of $\hat{H}'$, only opposite parity atomic states can couple through the dipole interaction ($\hat{H}'_{gg}(t) = \hat{H}'_{ee}(t) = 0$) giving the final form of the Hamiltonian matrix as

$$\hat{H} = \begin{pmatrix} 0 & -\vec{\mu}.\vec{E}^{*}(\vec{r},t) \\ -\vec{\mu}.\vec{E}(\vec{r},t) & \hbar\omega_e \end{pmatrix}. \tag{2.20}$$

Using Eq. (2.20) in Eq. (2.14) one can now calculate the time evolution of the density matrix which becomes

$$\begin{pmatrix} \dot{\rho}_{gg} & \dot{\rho}^{*}_{eg} \\ \dot{\rho}_{eg} & \dot{\rho}_{ee} \end{pmatrix} = i\begin{pmatrix} \Omega^{*}(\vec{r},t)\rho_{eg} - \Omega(\vec{r},t)\rho^{*}_{eg} & \omega_e\rho^{*}_{eg} - \Omega^{*}(\vec{r},t)u \\ -\omega_e\rho_{eg} + \Omega(\vec{r},t)u & -\Omega^{*}(\vec{r},t)\rho_{eg} + \Omega(\vec{r},t)\rho^{*}_{eg} \end{pmatrix}, \tag{2.21}$$

where $\Omega(\vec{r},t) = \vec{\mu}.\vec{E}(\vec{r},t)/\hbar$ is the Rabi frequency and $u = \rho_{gg} - \rho_{ee}$ is the population difference. For a closed two level system, the total population is conserved, i.e. $\rho_{ee} + \rho_{gg} = 1$, and $\rho_{eg} = \rho^{*}_{ge}$. Then the optical Bloch equations can be written as [65]:

$$\frac{\mathrm{d}\rho_{eg}(t)}{\mathrm{d}t} = -\frac{\gamma}{2}\rho_{eg} - i\omega_e\rho_{eg} + i\Omega(\vec{r},t)u, \tag{2.22}$$

and

$$\frac{\mathrm{d}u}{\mathrm{d}t} = \gamma(1-u) + i[\Omega^{*}(\vec{r},t)\rho_{eg} - \Omega(\vec{r},t)\rho^{*}_{eg}], \tag{2.23}$$

where the spontaneous emission rate is $\gamma = \frac{\omega_l^3 \mu^2}{3\pi\epsilon_0 \hbar c^3}$, with ω_l the laser frequency. The first term in the equations is introduced to account for the effect of spontaneous emission in the evolution of the density matrix. Let us write $\rho_{eg} = \sigma_{eg} e^{-i\omega_l t}$ and $\vec{E}(\vec{r}, t) = \vec{E}(\vec{r}) \cos(\omega_l t)$, then Eqs. (2.22) and (2.23) reduce to

$$\frac{\mathrm{d}\sigma_{eg}}{\mathrm{d}t} = -(\gamma/2 - i\delta)\sigma_{eg} + \frac{iu\Omega^*(\vec{r})}{2}, \tag{2.24}$$

and

$$\frac{\mathrm{d}u}{\mathrm{d}t} = \gamma(1-u) + i[\Omega^*(\vec{r})\sigma_{eg} - \Omega(\vec{r})\sigma_{eg}^*], \tag{2.25}$$

where the rotating wave approximation is used (we ignore the terms with high frequencies ($2\omega_l$) because they average to zero) and $\delta = \omega_l - \omega_e$ is the laser frequency detuning from the atomic transition. The steady state solutions of Eqs. (2.24) and (2.25) are

$$\sigma_{eg} = \frac{2\Omega(-\delta + i\frac{\gamma}{2})}{\gamma^2 \left[1 + \left(\frac{2\delta}{\gamma}\right)^2 + 2\left(\frac{\Omega}{\gamma}\right)^2\right]}, \tag{2.26}$$

and

$$u = \frac{1 + \left(\frac{2\delta}{\gamma}\right)^2}{\left[1 + \left(\frac{2\delta}{\gamma}\right)^2 + \left(\frac{2\Omega}{\gamma}\right)^2\right]}, \tag{2.27}$$

where $\Omega = \vec{\mu}.\vec{E}(\vec{r})/\hbar$ is the Rabi frequency. Using the conservation of total population, we can explicitly calculate ρ_{gg} and ρ_{ee} and thus the force operator. For a special case, where electric field is produced by a traveling wave propagating in z-direction, $E(z) = E_0 \cos(kz - \omega_l t)$, the force operator can be written as

$$\hat{F} = \begin{pmatrix} 0 & \mu\frac{\partial E^*(z)}{\partial z} \\ \mu\frac{\partial E(z)}{\partial z} & 0 \end{pmatrix}. \tag{2.28}$$

Now Eq. (2.13) can be rewritten as

$$\langle \hat{F} \rangle = \mathrm{Tr}(\hat{\rho}\hat{F}) = \mu\frac{\partial E}{\partial z}\sigma_{eg}^* e^{i\omega_l t} + \mu\frac{\partial E^*}{\partial z}\sigma_{eg} e^{-i\omega_l t}. \tag{2.29}$$

After substituting Eq. (2.26) in Eq. (2.29), the force on a stationary atom will be

$$F = \frac{\hbar k \gamma s}{2\left[1 + \left(\frac{2\delta}{\gamma}\right)^2 + s\right]} \tag{2.30}$$

where $s = \frac{2\Omega^2}{\gamma^2}$, is the saturation parameter. It is also defined as $s = I/I_s$, where I and $I_s = \frac{\pi hc}{3\lambda^3 \tau}$, with τ the upper state life time, are the laser light intensity and saturation intensity respectively. Now we can extend this result to a moving atom. An atom moving with velocity v will see a Doppler shift of $\pm kv$ in the laser frequency, where the plus (minus) sign refers to an atom moving in the opposite (same) direction to the laser beam. Thus an atom sees the laser frequency detuned by $\delta \pm kv$ and the force on a moving atom is given by

$$F = \pm \frac{\hbar k \gamma s}{2\left[1 + \left(\frac{2(\delta \mp kv)}{\gamma}\right)^2 + s\right]}, \tag{2.31}$$

where the plus (minus) refers to the force experienced by an atom moving along (opposite) the direction of light field. Let us consider the case of an atom interacting with two counter-propagating beams in z-direction, then the total force on an atom will be

$$F = \frac{\hbar k \gamma s}{2\left[1 + \left(\frac{2(\delta - kv)}{\gamma}\right)^2 + s\right]} - \frac{\hbar k \gamma s}{2\left[1 + \left(\frac{2(\delta + kv)}{\gamma}\right)^2 + s\right]}. \tag{2.32}$$

In the limit of Doppler shift small compared to δ, the above equation results in a velocity-dependent (therefore non-conservative) force $F = -\beta v$, where β is a damping coefficient given by

$$\beta = \frac{8\hbar k^2 s \delta}{\gamma\left[1 + \left(\frac{2\delta}{\gamma}\right)^2 + s\right]}, \tag{2.33}$$

This equation can be interpreted as follows. If the laser frequency is detuned below the resonant frequency, i.e. $\delta < 0$, atoms moving towards the laser beam see the laser's frequency Doppler shifted closer to resonance, while the atoms moving in the same direction to the laser beam see it shifted further away from the resonance. Thus the atoms will preferentially absorb photons from the laser beam toward which it is moving and then spontaneously re-emit this photon in a random direction (assuming low light intensity and hence no stimulated emission). Because of the spatial symmetry of the emitted

fluorescence, there is a net zero average momentum transfer from a large number of such fluorescence events. However, because the laser is detuned below resonance, slightly more energy is released than absorbed (the atom re-emits at the resonance frequency). This energy loss finally leads to a decrease in the atoms' velocity and their cooling as a result [65].

By using three pairs of counter-propagating beams in three orthogonal directions the atoms will feel a damping force in three dimensions regardless of the direction of the atom's motion. By implementing this scheme, the motion of atoms in the intersection region can be suppressed in all three dimensions, and many atoms can therefore be cooled in a small volume. This damping mechanism, called optical molasses, is one of the basic tools of laser cooling. The experimental implementation of this theory to cool atoms was first done by Chu et al. [70]. In rubidium Doppler cooling, the six laser beams are tuned below the $5^2S_{1/2}, F = 2 \rightarrow 5^2P_{3/2}, F' = 3$ transition ($\sim$780 nm) [71] to create the optical molasses [72].

From Eq. (2.32) one would assume that the damping force could reduce the atomic velocities to zero, giving rise to an absolute temperature of zero. However, the cooling is limited in the optical molasses with the Doppler limit when the heating due to emission balances the cooling due to absorption. In other words, while the average momentum transfer of many spontaneous emissions is zero, their rms value is finite and results in the heating as the number of scattering photons increase. This steady state temperature, called Doppler temperature, is given by

$$T_D = \frac{\hbar\gamma}{2k_B}, \tag{2.34}$$

where k_B is the Boltzman constant and γ is the natural broadening linewidth of the excited state. For ^{87}Rb, $\gamma = 2\pi \cdot 5.9$ MHz giving a Doppler temperature about 146 μK [72].

However, temperatures below the Doppler limit have been achieved by manipulating the polarization of counter-propagating laser beams. In a $\sigma^+ - \sigma^-$ configuration, the cooling is due to different probabilities of absorbing a σ^+ or a σ^- photon due to Clebsch-Gordan coefficients [73]. This mechanism allows for temperatures below the Doppler limit until the cooling is limited by the recoil temperature ($\sim$360 nK for ^{87}Rb). This limit results from the recoil energy the atoms absorb from spontaneous emission, defined by [66]:

$$k_B T_r = \frac{\hbar^2 k^2}{2M}. \tag{2.35}$$

2.2.2 Magneto-Optical Trap

In the previous sections, the theory of laser cooling was explained, but in order to trap the atoms, light alone is not sufficient. An atom can diffuse out of the system, since the force of light acting on the atoms is strictly velocity-dependent (see Eq. (2.32)). By adding a quadrupole magnetic field, and using opposite, circular polarization cooling beams, one can address this issue by introducing an additional position-dependent force. In this technique, called magneto-optical trapping (MOT), the optical and magnetic fields are employed to cool and trap the neutral atoms at the same time [65, 74]. The operation of a MOT depends on both a spatially varying magnetic field and a proper arrangement of laser beams tuned below the atomic resonance. The basic concept can be explained using an atom with a ground state, $J_g = 0$, and an excited state, $J_e = 1$, subjected to a linearly inhomogeneous magnetic field $B(z) = B_0 z$. This magnetic field splits the excited state into three Zeeman components $M_e = -1$, 0, and $+1$ as shown in Figure 2.1. Adding two counter-propagating laser beams of opposite circular polarization, each detuned below the zero field atomic transition completes the requirement to create a MOT.

Because of the Zeeman shift, for $B > 0$, the excited state $M_e = +1$ is shifted up and $M_e = -1$ is shifted down. The shift of $M_e = \pm 1$ is reversed for $B < 0$. At a positive z in Figure 2.1, the magnetic field gradient tunes the $\Delta M = -1$ transition closer to the resonance and the $\Delta M = +1$ transition further away from the resonance. If the polarization of the laser beam incident from the right (left) is σ^- (σ^+), then the atoms absorb more light from the σ^- beam than from the σ^+ one. As a result the atoms are pushed towards the center where there is no magnetic field. On the left-hand side, the negative magnetic field tunes the $\Delta M = +1$ transition closer to the resonance. Thus the atoms absorb more light from the σ^+ beam, drifting towards the center of the trap. This technique finally leads to the trapping and cooling of atoms at the same time. It can be seen that in the MOT, the damping force due to the Doppler effect applies on position space rather than the velocity space, which is the case for optical molasses. A 3D extension of MOT can be obtained by using three pairs of counter-propagating beams in orthogonal directions [65]. The detuning of each laser beam in the presence of the magnetic field is given by

$$\delta_\pm = \delta \mp \vec{k} \cdot \vec{v} \pm \mu' B/\hbar, \tag{2.36}$$

where the effective magnetic moment is $\mu' = \mu_B(g_e M_e - g_g M_g)$, with μ_B the Bohr magneton and g

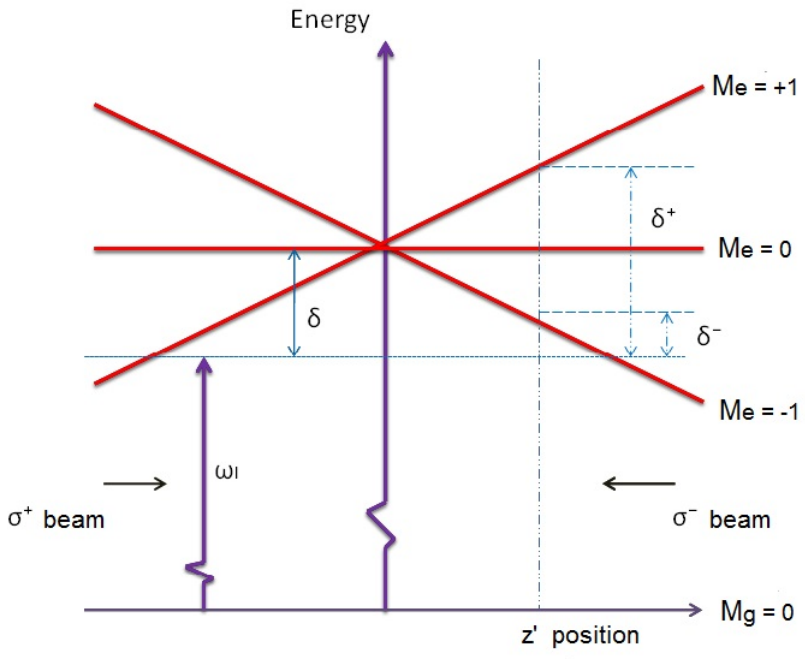

Figure 2.1: Arrangement of a 1D MOT. The detuning δ is for atoms at rest at the trap's center. Due to the Zeeman shift of magnetic sublevels, and the arrangement of laser polarizations, atoms are driven to the trap's center. Spatial confinement and cooling are obtained simultaneously.

the Landé g-factor. Thus the total force on the atom is

$$F_{\pm} = \pm \frac{\hbar \vec{k} \gamma}{2} \frac{s_0}{1 + s_0 + \left(\frac{2\delta_{\pm}}{\gamma}\right)^2}, \tag{2.37}$$

where $s_0 = 2|\Omega|^2/\gamma^2 = I/I_s$.

2.2.3 Evaporative Cooling

In order to observe the BEC transition, the phase space densities, ρ, should be greater than 2.612 [67]. For ordinary gases at room temperature and pressure, $\rho \sim 10^{-6}$ and for an atomic beam $\rho \sim 10^{-10}$. In optical molasses, the achievable phase space density can be enhanced to $10^{-5} - 10^{-4}$ corresponding to the recoil temperature. Therefore, laser cooling alone is not the most likely route for achieving BEC. In this respect, evaporative cooling is a way to increase the phase space density further [75].

The idea of evaporative cooling is based on the preferential removal of atoms with energy higher than the average from a trap, followed by rethermalization of the remaining atoms by elastic collisions

[75]. Therefore both temperature and volume decrease leading to a notable increase in the phase space density. For evaporative cooling of atoms, magnetic fields or far-off-resonant optical fields have been used. In the latter case, the effect of the laser beam on the atoms can be considered as that of a static electric field. This electric field induces a dipole moment on the atoms which then interacts with the electric field of the radiation. This $\vec{\mu} - \vec{E}$ coupling therefore creates an attractive potential given by [72]:

$$U = -\frac{1}{2}\alpha_g E^2, \tag{2.38}$$

where, α_g is the ground state polarizabity of the atom. For a Gaussian beam propagating in the z-direction, the trapping potential can be approximated as a harmonic potential given by ($z \ll z_R$)

$$U \approx -\frac{1}{2}\alpha_g E_0^2 \left(1 - \frac{2x^2}{w_0^2} - \frac{2y^2}{w_0^2} - \frac{z^2}{z_R^2}\right), \tag{2.39}$$

where w_0 is the beam waist size at the focus and z_R is the Rayleigh range which gives the axial extent of the trap. The depth of the trap is inversely proportional to the detuning of the laser from the atomic transition ($U \approx \hbar I/4\delta_l$), whereas the spontaneous scattering rate is inversely proportional to the square of detuning ($\gamma \approx \Gamma I/4\delta_l^2$, where Γ is the spontaneous emission rate of the atom) [76]. This means that to achieve an efficient evaporative cooling, it is preferable to apply a far-off-resonance optical potential, because the scattering rate drops faster than the potential depth at larger detunings.

Chapter 3

Discrete-Time Quantum Walk

Quantum walks, similar to their classical counterparts, can take many different forms, starting from the simple discrete random walk on a line [77], to random walks on a circle [78], to continuous-time random walks [12], such as Brownian motion. In this work we only consider discrete-time quantum walks, in which the particle propagates in discrete steps determined by a dynamic internal degree of freedom. In the two following sections, we review the simple models of random walks on a line highlighting the differences between the classical and quantum versions. The classical walks are Gaussian, and therefore can be described by their standard deviations [4]. The quantum walks are highly non-Gaussian, however we analyze the standard deviations of these walks as well, in order to make a fair comparison with the classical walks.

3.1 Classical Walk vs. Quantum Walk

3.1.1 Classical Walk on a Line

Imagine a person standing at the origin of a line with a coin in their hand. They flip the coin, and if it comes up heads, they take a step to the right, if it is tails, they take a step to the left. They then repeat this procedure, flipping the coin, and taking a step based on the result. The probability $P(j,d)$ of being in a position d after j steps is [24]

$$P(j,d) = \frac{1}{2^j} \begin{pmatrix} j \\ \frac{d+j}{2} \end{pmatrix}. \tag{3.1}$$

j/d	-4	-3	-2	-1	0	1	2	3	4
0					1				
1				$\frac{1}{2}$	0	$\frac{1}{2}$			
2			$\frac{1}{4}$	0	$\frac{1}{2}$	0	$\frac{1}{4}$		
3		$\frac{1}{8}$	0	$\frac{3}{8}$	0	$\frac{3}{8}$	0	$\frac{1}{8}$	
4	$\frac{1}{16}$	0	$\frac{4}{16}$	0	$\frac{6}{16}$	0	$\frac{4}{16}$	0	$\frac{1}{16}$

Table 3.1: The probability of being found at position d after j steps of the classical random walk on the line.

Note that if j is even (odd), only even (odd) positions are occupied. Table 3.1 contains the probabilities for the first few values of j. The nonzero elements of the distribution are simply terms from Pascal's triangle, divided by the appropriate factor of two. The distribution of this walk can be well illustrated with the help of Galton's board (also called Quincunx) in Figure 3.1. There are a few features of this random walk that one can compare to the quantum analog. First, after each coin toss, unlike the quantum version, there is no correlation between the positions left. The other property of this walk that we are interested in is the fact that its limiting distribution on the line (for large number of iterations j) approaches a Gaussian distribution. The mean of this distribution is zero, that is intuitively obvious; we are using a fair coin, so we are as likely to step left as we are to step right. It is also not hard to calculate that the standard deviation of this distribution, σ_c, is given by $\sigma_c = \sqrt{j}$ [4].

3.1.2 Quantum Walk on a Line

Now let us consider a quantum version of the walk on a line. In quantum jargon, the coin can be considered as a qubit. Here we will be representing the two levels of the qubit with the quantum states $|1\rangle$ and $|2\rangle$. If we start with the qubit in the $|1\rangle$ state, and apply a coin toss operation $\hat{\mathbf{M}}$, we get an equal superposition of $|1\rangle$ and $|2\rangle$,

$$\hat{\mathbf{M}} = \frac{1}{\sqrt{2}} \begin{pmatrix} 1 & i \\ i & 1 \end{pmatrix}, \qquad \hat{\mathbf{M}}|1\rangle = \frac{1}{\sqrt{2}} \left(|1\rangle + i|2\rangle\right). \tag{3.2}$$

If we were to measure the qubit, and step left or right depending upon the result, we would obtain exactly the classical walk described in Section 3.1.1. Now, rather than a person holding a coin, suppose we have a particle, whose motion is confined to one dimension. We can now treat the particle as a

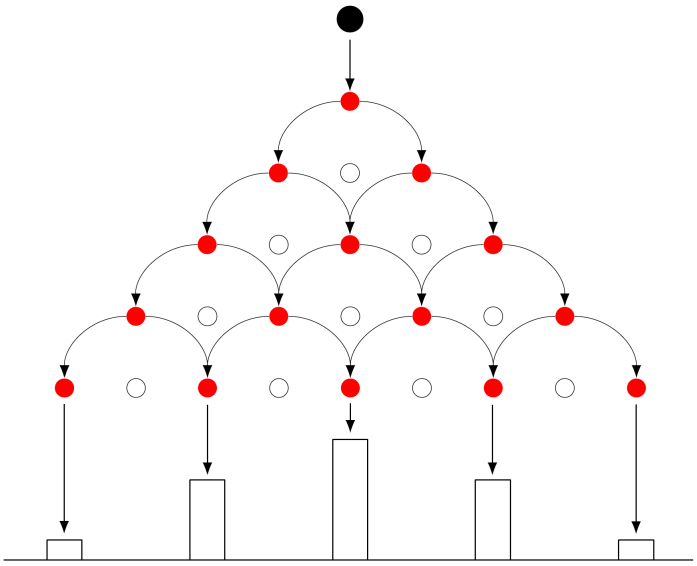

Figure 3.1: Galton's Board (Quincunx): the Quincunx is a device which allows a bead to drop through an array of pins stuck in a board. The pins are equally spaced in a number of rows and when the bead hits a pin it is equally likely to fall to the left or the right. It then lands on a pin in the next row where the process is repeated. After passing through all rows it is collected in a slot at the bottom. The distribution of beads approaches a Gaussian after many rows of pins and many beads.

quantum system, and perform the quantum walk as follows. During each iteration, we apply the coin toss operation, followed by the operation which steps right if the qubit is $|1\rangle$, and steps left if the qubit is $|2\rangle$. That is, we apply the operator, $\hat{\mathbf{U}}_{\text{step}} = \hat{\mathbf{M}}\hat{\mathbf{T}}$ where $\hat{\mathbf{T}}$ is the shift operator whose direction depends on the result of the coin operator $\hat{\mathbf{M}}$. Therefore, the state of the system after j steps will be

$$|\Psi_j\rangle = \left(\hat{\mathbf{U}}_{\text{step}}\right)^j |\Psi_0\rangle, \tag{3.3}$$

where $|\Psi_0\rangle$ is the initial state of the system. The mean of the distribution produced by this quantum random walk is not necessarily zero. It is dependent upon the initial state of the qubit. For example, choosing the initial state of the qubit to be $|1\rangle$ gives a nonzero mean after the second step. For the remainder of this work, we will only be considering the distribution created with the initial qubit state $|\Psi_0\rangle = \frac{1}{\sqrt{2}}(|1\rangle + |2\rangle)$ which has a mean of zero for all values of j. Table 3.2 contains the probability distribution associated with the first few states $|\Psi_j\rangle$. The nonzero elements of the distribution are no longer simply terms from Pascal's triangle, which arose in the classical case.

In the quantum random walk we of course do not measure the coin register during intermediate iterations, but rather keep the quantum correlations between different positions and let them interfere

j/d	-4	-3	-2	-1	0	1	2	3	4
0					1				
1				$\frac{1}{2}$	0	$\frac{1}{2}$			
2			$\frac{1}{4}$	0	$\frac{1}{2}$	0	$\frac{1}{4}$		
3		$\frac{1}{8}$	0	$\frac{3}{8}$	0	$\frac{3}{8}$	0	$\frac{1}{8}$	
4	$\frac{1}{16}$	0	$\frac{6}{16}$	0	$\frac{2}{16}$	0	$\frac{6}{16}$	0	$\frac{1}{16}$

Table 3.2: The probability of being found at position d after j steps of the quantum walk on the line, with the initial qubit state $|\Psi_0\rangle = \frac{1}{\sqrt{2}}(|1\rangle + |2\rangle)$.

in subsequent steps [13]. This interference results in a radically different behavior of the quantum walk. In particular we see that the limiting distribution of the walk on the line does not approach a Gaussian, but it appears as a pair of "horns" diverging ballistically by the number of iterations as shown in Figure 3.2. Now it is no longer simple to calculate the standard deviation of the distribution. However, numerical simulations reveal that the standard deviation, σ_q, is almost independent of the initial state of the qubit, and is approximately linear; $\sigma_q \sim j$ [4]. Thus, the standard deviation in a quantum walk grows significantly faster than that of a classical walks on a line.

In the following, we explain in detail how we implement a discrete-time quantum walk in momentum space. In our experiments, a coin operator $\hat{\mathbf{M}}$ producing a superposition of two internal states, followed by a unitary shift operator $\hat{\mathbf{T}}$, implements each step of the walk $\hat{\mathbf{U}}_{\text{step}} = \hat{\mathbf{M}}\hat{\mathbf{T}}$.

3.2 Coin Operator

The idea of the quantum coin operator can be realized in an atomic system (e.g. a BEC) using a balanced superposition of two hyperfine states of alkali atoms. Unlike a classical coin that produces only one state at a time (e.g. either head or tail), the quantum coin operator, can produce a superposition of two or more states and, therefore, the direction of the subsequent shift is affected by the interference between these states. We realize the coin operator using resonant microwave radiation that addresses the two components of the internal degree of freedom, i.e. two of the states in the ground ($5^2S_{1/2}$) hyperfine levels of the ^{87}Rb atoms. These two states are the $|F = 1, m_F = 0\rangle$ and the $|F = 2, m_F = 0\rangle$ that, in this section, we denote them by $|g\rangle$ and $|e\rangle$ respectively. To understand the mechanism of generating the desired superposition, a brief review of the MW transition with an approach to the Bloch vector and Rabi oscillation is useful.

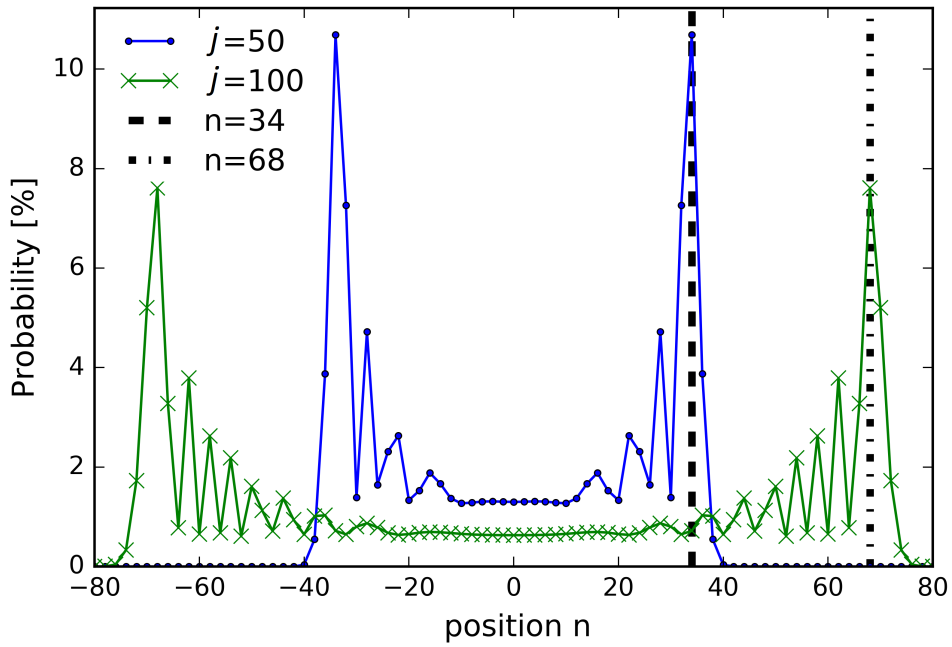

Figure 3.2: Probability distribution of a quantum walk initiated with a state $|\Psi_0\rangle = \frac{1}{\sqrt{2}}(|1\rangle + |2\rangle)$ and evolved under the coin toss operators given in Eq. (3.2). Distributions are plotted for $j = 50$ and $j = 100$ number of steps. The characteristic standard deviation of the distribution at either case is $\sim j$.

3.2.1 Bloch Vector

In alkali atoms, the hyperfine interaction between the electron spin and the nuclear spin splits the ground state into two levels whose frequency difference is in the order of several GHz [71]. Those two levels can be treated as a two-level atom, since the energy difference between them and the first excited state corresponds to hundreds of THz [68]. The two-level atomic system (e.g. ^{87}Rb) can be represented by the Bloch sphere (Figure 3.3). The north and the south poles of that unit sphere represent the two pure states $|g\rangle$ and $|e\rangle$, corresponding to the ground and the excited states of the two-level atom. Any other point on the sphere represents a superposition state, namely [79],

$$|\Psi\rangle = \cos\frac{\theta}{2}|g\rangle + e^{i\phi}\sin\frac{\theta}{2}|e\rangle, \tag{3.4}$$

where θ and ϕ are the spherical coordinates and the evolution of the atomic state over time is expressed by the variation of these coordinates. The Bloch vector can be also represented in Cartesian coordinates

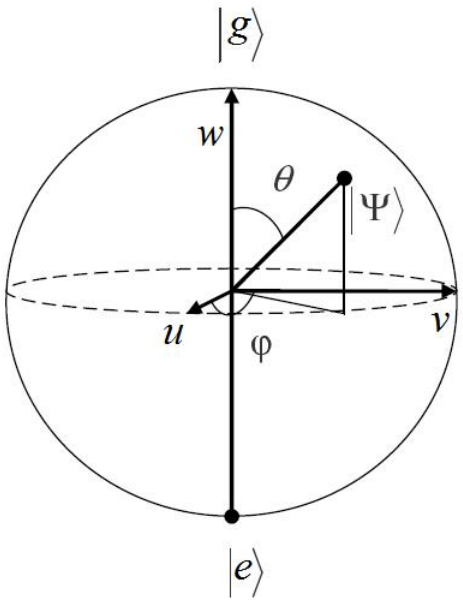

Figure 3.3: The Bloch sphere.

as [79]:

$$\hat{\nu}^B = (u, v, w) = (\sin\theta\cos\phi,\ \sin\theta\sin\phi,\ \cos\theta) \tag{3.5}$$

One can deduce the following information from the Bloch vector components: First, the population of the states can be derived from the component w (ranging from -1 to 1) as $P_g = (1 + w)/2$ and $P_e = (1 - w)/2$ ranging from 0 to 1, while the components u and v indicate "coherence" between the states. Second, the Bloch vector will describe a pure state if and only if $u^2 + v^2 + w^2 = 1$. Otherwise, it will describe a mixed state representing a dephasing or decoherence process. Geometrically, a mixed state will be described by a vector with precession inside the Bloch sphere rather than its surface.

3.2.2 Rate Equations

The time-dependence of the atom's state function can be shown as the superposition of the two orthogonal states [80]:

$$|\Psi(t)\rangle = C_g(t)|g\rangle + C_e(t)|e\rangle \tag{3.6}$$

In the absence of an external force ($\hat{H}(t) = \hat{H}_0$), the system is stationary, and the probability of finding the system in any one of the states is constant. It follows that the dependence of the amplitude C_i on

time is only in the phase, and Eq. (3.6) can be written as

$$|\Psi(t)\rangle = e^{-i\frac{E_g t}{\hbar}} C_g(0)|g\rangle + e^{-i\frac{E_e t}{\hbar}} C_e(0)|e\rangle. \tag{3.7}$$

Now in case of adding a time-dependent interaction ($\hat{H}(t) = \hat{H} + \hat{V}(t)$), the coupling between the two states due to the interaction can be described by calculating the matrix elements of $\hat{V}(t)$ in the basis of $\hat{H}_0$:

$$V_{ij} = \langle \psi_i | \hat{V} | \psi_j \rangle. \tag{3.8}$$

Introducing Eq. (3.6) into the Schrödinger equation, $i\hbar\frac{\partial|\Psi(t)\rangle}{\partial t} = \hat{H}(t)|\Psi(t)\rangle$, the rate equations for the amplitudes $C_i(t)$ can be derived as:

$$i\hbar\frac{\mathrm{d}}{\mathrm{d}t}\begin{pmatrix} C_g(t) \\ C_e(t) \end{pmatrix} = \begin{pmatrix} E_g + V_{gg}(t) & V_{ge}(t) \\ V_{eg}(t) & E_e + V_{ee}(t) \end{pmatrix}\begin{pmatrix} C_g(t) \\ C_e(t) \end{pmatrix}. \tag{3.9}$$

Once $\hat{V}(t)$ and the initial conditions are specified, this equation provides the evolution of a two-state system subjected to an external interaction which gives rise to the population of each state.

3.2.3 Rabi Oscillations

The hyperfine interaction between the electron spin and nuclear spin splits the ground state $5^2S_{1/2}$ of ^{87}Rb into two hyperfine levels $F = 1$ and $F = 2$. This splitting is $\Delta\nu_{\mathrm{HFS}} = 2\pi \cdot 6.834682610$ GHz and each of these levels consists of different Zeeman sublevels (m_F) as shown in Figure 3.4 [71]. Direct coupling of each pair of these sublevels (those fulfilling the selection rules $\Delta m_F = 0, \pm 1$), through a one-photon transition is thus realized using the MW radiation.

Since both states have spherical symmetry (the electric dipole is zero) this transition is governed by the dipole potential created by the magnetic field of the MW radiation

$$V = (\vec{\mu}_{\mathrm{L}} + \vec{\mu}_{\mathrm{S}} + \vec{\mu}_{\mathrm{I}}) \cdot \vec{B}, \tag{3.10}$$

where, $\vec{\mu}_{\mathrm{L}} = \mu_{\mathrm{B}} g_{\mathrm{L}} \vec{L}/\hbar$, $\vec{\mu}_{\mathrm{S}} = \mu_{\mathrm{B}} g_{\mathrm{S}} \vec{S}/\hbar$ and $\vec{\mu}_{\mathrm{I}} = \mu_{\mathrm{B}} g_{\mathrm{I}} \vec{I}/\hbar$ are respectively the orbital, spin and nucleus magnetic moments. Also $\mu_{\mathrm{B}} = e\hbar/2m_e$ is the Bohr magneton and $\vec{L}$, $\vec{S}$ and $\vec{I}$ are the orbital,

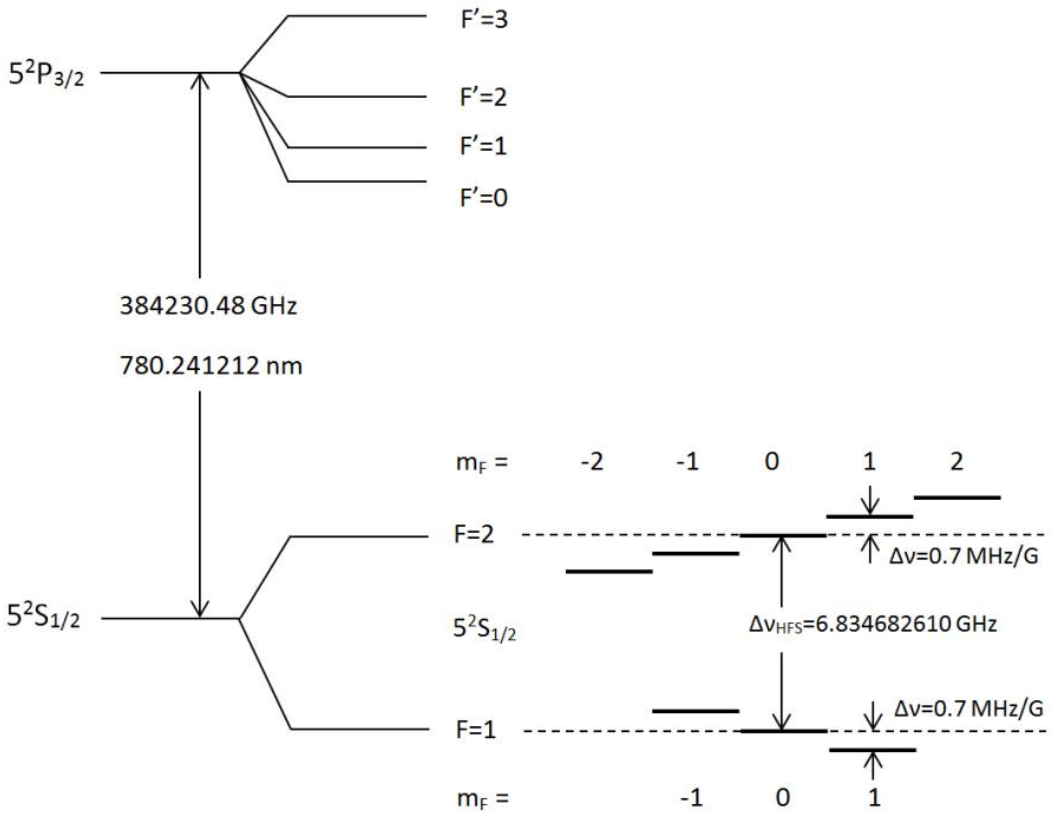

Figure 3.4: ^{87}Rb D_2 transition hyperfine structure, with frequency splittings between the hyperfine energy levels. Each level consists of different sublevels (m_F) splitting in the presence of a magnetic field.

spin and nuclear spin angular momenta [71].

Since the ground state hyperfine levels are both s-states ($\vec{L} = 0$), assuming that the magnetic field has a linear polarization ($\vec{B} = B_1 \cos(\omega t)\hat{z}$), the interaction potential will take the form

$$\hat{V}(t) = \frac{B_1}{\hbar}(\mu_{\mathrm{B}} g_{\mathrm{S}} S_{\mathrm{z}} + \mu_{\mathrm{B}} g_{\mathrm{I}} I_{\mathrm{z}}) \cos(\omega t). \tag{3.11}$$

The matrix elements of $\hat{V}(t)$ can be calculated between two Zeeman sublevels by using the Clebsch-Gordon coefficients in the basis $\{I_{\mathrm{z}}, S_{\mathrm{z}}\}$. For the $|F = 1, m_F = 0\rangle \leftrightarrow |F = 2, m_F = 0\rangle$ transition these elements will be

$$\begin{aligned} V_{eg} &= \langle F = 1, m_F = 0 | V | F = 2, m_F = 0 \rangle \\ &= \frac{B_1}{2\hbar} \cos(\omega t) \left[\langle \frac{1}{2}, -\frac{1}{2} | + \langle -\frac{1}{2}, \frac{1}{2} | \right] (\mu_{\mathrm{B}} g_{\mathrm{S}} S_{\mathrm{z}} + \mu_{\mathrm{B}} g_{\mathrm{I}} I_{\mathrm{z}}) \left[| \frac{1}{2}, -\frac{1}{2} \rangle + | -\frac{1}{2}, \frac{1}{2} \rangle \right] \\ &= \frac{-B_1}{2} \cos(\omega t)(\mu_{\mathrm{B}} g_{\mathrm{S}} - \mu_{\mathrm{B}} g_{\mathrm{I}}), \end{aligned} \tag{3.12}$$

and for the other $\Delta m_F = 0$ transitions

$$V_{eg} = \langle 1, 1 | V | 2, 1 \rangle = \langle 1, -1 | V | 2, -1 \rangle = \frac{-\sqrt{3} B_1}{4} \cos(\omega t)(\mu_{\mathrm{B}} g_{\mathrm{S}} - \mu_{\mathrm{B}} g_{\mathrm{I}}). \tag{3.13}$$

Since we took the MW field to be linearly polarized, the matrix element is zero for $\Delta m_F \neq 0$. Now the temporal evolution of the atomic states (the population) can be calculated by inserting the matrix elements of each Δm_F transition into the rate equations (Eq. (3.9)) derived from the Schrödinger equation. Assuming that the system is initially in the ground state and the MW frequency is detuned from the atomic transition by $\delta = \omega - \omega_0$ and also knowing that $V_{ee} = V_{gg} = 0$ and $V_{ge} = V_{eg}^*$, one can obtain the population of the excited state as

$$P_e(t) = |C_e(t)|^2 = \frac{1}{2} \frac{|\Omega|^2}{\bar{\Omega}^2} \left[1 - \cos(\Omega t) \right]. \tag{3.14}$$

Eq. (3.14) predicts that the system will undergo oscillations between the two states at a rate determined by the generalized Rabi frequency $\bar{\Omega} = \sqrt{|\Omega|^2 + \delta^2}$ in which the Rabi frequency can be expressed for

the $|F=1, m_F=0\rangle \leftrightarrow |F=2, m_F=0\rangle$ transition as

$$\Omega = \frac{-B_1}{2\hbar}(\mu_{\mathrm{B}} g_{\mathrm{S}} - \mu_{\mathrm{B}} g_{\mathrm{I}}), \tag{3.15}$$

and for the other $\Delta m_F = 0$ transitions as

$$\Omega = \frac{-\sqrt{3}B_1}{4\hbar}(\mu_{\mathrm{B}} g_{\mathrm{S}} - \mu_{\mathrm{B}} g_{\mathrm{I}}). \tag{3.16}$$

3.2.4 Rabi Pulses

Focusing on the resonant case ($\delta = 0$), the precession of the Bloch vector due to an interaction applied for a time t can be described as [81]

$$\hat{\nu}^B(t) = \hat{\Theta}_\theta(t)\ \hat{\nu}^B(0), \tag{3.17}$$

where $\hat{\Theta}_\theta(t)$ is a 3×3 matrix describing a rotation with angle $\theta(t)$ around the u-axis:

$$\hat{\Theta}_\theta(t) = \begin{pmatrix} 1 & 0 & 0 \\ 0 & \cos\theta(t) & \sin\theta(t) \\ 0 & -\sin\theta(t) & \cos\theta(t) \end{pmatrix}, \tag{3.18}$$

where $\theta(t) = \Omega \cdot t$. In the state vector representation, a resonant pulse of duration t is expressed by the application of a unitary operator $\hat{\mathbf{M}}(t)$ to the state vector:

$$|\Psi(t)\rangle = \hat{\mathbf{M}}(t)|\Psi(0)\rangle \tag{3.19}$$

A derivation of $\hat{\mathbf{M}}(t)$ is presented in [81], which yields:

$$\hat{\mathbf{M}}\left(\theta(t), \chi\right) = \begin{pmatrix} \cos\frac{\theta(t)}{2} & e^{-i\chi}\sin\frac{\theta(t)}{2} \\ -e^{i\chi}\sin\frac{\theta(t)}{2} & \cos\frac{\theta(t)}{2} \end{pmatrix}, \tag{3.20}$$

where χ is the offset phase of the resonant pulse. If a $\pi/2$ pulse ($\theta(t_M) = \Omega \cdot t_M = \pi/2$) is applied on a system initially in the ground state, the Bloch vector will rotate to

$$\hat{\nu}^B_{\pi/2} = \hat{\Theta}_{\pi/2}\, \hat{\nu}^B_0 = \begin{pmatrix} 1 & 0 & 0 \\ 0 & 0 & 1 \\ 0 & -1 & 0 \end{pmatrix} \begin{pmatrix} 0 \\ 0 \\ 1 \end{pmatrix} = \begin{pmatrix} 0 \\ 1 \\ 0 \end{pmatrix} \tag{3.21}$$

If the Bloch vector initially lies on the sphere's surface in w-direction, corresponding to a full concentration of the population in the ground state, a $\pi/2$ pulse will take the vector halfway, to point in the v-direction. This means that the system will be in an equal superposition of the energy states as can be derived using the evolution operator in state vector picture:

$$\begin{aligned} |\Psi_{\pi/2}\rangle &= \hat{\mathbf{M}}\,(\pi/2, \chi)\ \ |g\rangle \\ &= \frac{1}{\sqrt{2}} \begin{pmatrix} 1 & e^{-i\chi} \\ -e^{i\chi} & 1 \end{pmatrix} \begin{pmatrix} 1 \\ 0 \end{pmatrix} = \frac{1}{\sqrt{2}} \begin{pmatrix} 1 \\ -e^{i\chi} \end{pmatrix} \\ &= \frac{1}{\sqrt{2}}(|g\rangle - e^{i\chi}|e\rangle). \end{aligned} \tag{3.22}$$

Thus the probability of finding the atom at either internal state will be:

$$\begin{aligned} P_g &= |C_g|^2 = |\frac{1}{\sqrt{2}}|^2 = \frac{1}{2}, \\ P_e &= |C_e|^2 = |\frac{-1}{\sqrt{2}} e^{i\chi}|^2 = \frac{1}{2}. \end{aligned} \tag{3.23}$$

Also by applying a π pulse, one can switch the state of the atom from one internal state to another:

$$\begin{aligned} |\Psi_{\pi}\rangle &= \hat{\mathbf{M}}\,(\pi, \chi)\ \ |g\rangle \\ &= \begin{pmatrix} 0 & e^{-i\chi} \\ -e^{i\chi} & 0 \end{pmatrix} \begin{pmatrix} 1 \\ 0 \end{pmatrix} = \begin{pmatrix} 0 \\ -e^{i\chi} \end{pmatrix} \\ &= -e^{i\chi}|e\rangle. \end{aligned} \tag{3.24}$$

i.e. the initial probability distribution, $P_g = 1$, $P_e = 0$ will change to

$$\begin{aligned} P_g &= 0, \\ P_e &= |-e^{i\chi}|^2 = 1. \end{aligned} \tag{3.25}$$

In this study, as we will see in Section 3.4, we apply different schemes of MW pulses to achieve equal (Hadamard gate and coin toss) and unequal (biased and swapped) superpositions of internal states to implement the desired walk. At this point however, it is sufficient to emphasize two useful operators that produce 50-50 combinations of internal states (hereafter denoted by $|1\rangle$ and $|2\rangle$):

$$\text{Gate}: \qquad \hat{\mathbf{M}}(\pi/2, \pi) = \frac{1}{\sqrt{2}} \begin{pmatrix} 1 & -1 \\ 1 & 1 \end{pmatrix} \tag{3.26}$$

$$\text{Coin}: \qquad \hat{\mathbf{M}}(\pi/2, -\pi/2) = \frac{1}{\sqrt{2}} \begin{pmatrix} 1 & i \\ i & 1 \end{pmatrix} \tag{3.27}$$

3.3 Unitary Shift Operator

To make a step for our walk contingent upon the result of a coin toss, we apply the unitary operator

$$\hat{\mathbf{T}} = \exp\left(i\hat{X}\Delta P/\hbar\right)|1\rangle\langle 1| + \exp\left(-i\hat{X}\Delta P/\hbar\right)|2\rangle\langle 2|, \tag{3.28}$$

which produces $\pm\Delta P$ shift in momentum space depending on whether the atom resides in the internal state $|1\rangle$ or $|2\rangle$ [23, 52]. We realize this conditional momentum shift by destroying the spatial-temporal symmetry using a quantum ratchet [45, 47, 82, 83, 84] and employing quantum resonance conditions on the dynamics [83, 85]. Implementation of a biased shift using a quantum ratchet is based on the dynamics of the AOKR. This system has a well-characterized model in momentum-space and from the day of its realization [41, 42, 43] it has been the workhorse for the study of various quantum mechanical phenomena [44, 45, 46, 47, 48, 49, 50, 51, 52]. To understand the mechanism of quantum resonant ratchet, a brief review on quantum resonant AOKR is instructive.

3.3.1 Atom-Optics Kicked Rotor

One of the systems of choice for studying crossover between classical and quantum behavior is the so-called kicked rotor. This paradigm is a promising tool in both classical and quantum regimes [86] to investigate the quantum signatures of the known classical dynamics, especially the deterministic chaos in periodically driven systems [41, 42, 43]. The classical kicked rotor can be described as a particle of mass M, constrained to move in a circle of radius R, which is exposed to a periodic constant force referred as kicks as shown in Figure 3.5. The effect of a kick depends sinusoidally on the azimuthal angular displacement θ. The kicked rotor is therefore described by the Hamiltonian [86]

$$\hat{H} = \frac{J'^2}{2I} + V_0 \cos(\theta) \sum_{j \in \mathbb{Z}} \delta(t - jT), \tag{3.29}$$

where J' is the angular momentum, and $I = MR^2$ is the moment of inertia of the particle. Also, V_0 is the kicking potential and δ is the Dirac delta function which represents the temporal periodicity of the kicks; it becomes nonzero only when the time t is an integer multiple of the time between the kicks, T. Dynamics of the kicked rotor, using the rescaled variables $J = J'T/I$ and $K = TV_0/I$, are described by the standard map [86, 87]:

$$\begin{aligned} \theta_{j+1} &= \theta_j + J_{j+1} \\ J_{j+1} &= J_j + K \sin\theta_j. \end{aligned} \tag{3.30}$$

The quantum counterpart of classical kicked rotor, i.e. the AOKR, is typically realized with a sample of ultra-cold atoms subject to a series of short pulses of a 1D far-off-resonant optical lattice (standing wave). The small initial temperature necessary to resolve the single momentum peaks is most easily reached using a BEC. The AOKR can be described by the Hamiltonian [86]

$$\hat{H} = \frac{\hat{P}^2}{2M} + \hbar k \left[1 + \cos(G\hat{X})\right] \sum_{j \in \mathbb{Z}} \delta(t - jT), \tag{3.31}$$

where $\hat{P}$ is the momentum, $\hat{X}$ is the position, $G = 2\pi/\lambda_G$ is the grating wave vector with λ_G the spatial period of the standing wave. The factor $\hbar k \left[1 + \cos(G\hat{X})\right]$ shows the combination of a DC and a periodic potential introduced by the interference of the two counter-propagating optical waves. Other quantities

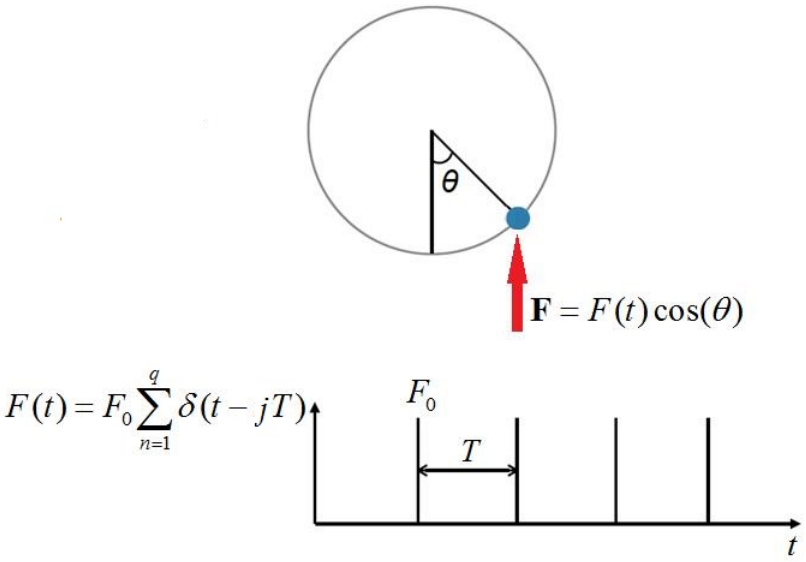

Figure 3.5: The classical kicked rotor; a particle of mass M and angular momentum J', that is constrained to move in a circle of radius R, is subjected to periodic pulses of force $F(t)$.

are t, the continuous time variable (integer units), j, the number of kicks with period T, and

$$k = \frac{\Omega^2 \Delta t}{8\delta_L} \tag{3.32}$$

the dimensionless strength of the kick. In the latter, Ω signifies the Rabi frequency between the ground and excited state, and Δt ($\ll T$) and δ_L are respectively the pulse length, and the detuning of the laser frequency from the atomic transition. Using dimensionless variables, the quantum dynamics of the center of mass of the atoms are then described by the following single-particle Hamiltonian [41, 83]:

$$\hat{\mathcal{H}}(\hat{x}, \hat{p}, \mathfrak{t}) = \frac{\hat{p}^2}{2} + k[1 + \cos(\hat{x})] \sum_{j \in \mathbb{Z}} \delta(\mathfrak{t} - j\tau), \tag{3.33}$$

in which $\hat{\mathcal{H}} = \frac{M\hat{H}}{\hbar^2 G^2}$, $\hat{x} = G\hat{X}$, $\hat{p} = \frac{\hat{P}}{\hbar G}$, $\mathfrak{t} = \frac{t\hbar G^2}{M}$, and $\tau = \frac{\hbar G^2 T}{M}$ are the dimensionless Hamiltonian, position, momentum, time, and kicking period respectively. The periodicity (time symmetry) of the kicks allows us to introduce a characteristic time called Talbot time, $T_T = 2T_{1/2} = \frac{4\pi M}{\hbar G^2}$ to reproduce the temporal analogy for the Talbot effect [88], in which the atomic matter wave, diffracted by a train of optical standing waves, will re-image itself at integer multiples of the time interval T_T.

It is convenient to write the momentum into discrete and continuous components as $p = n + \beta$,

where n is an integer multiple of the two-photon recoil in units of $\hbar G$, and β takes on values between 0 and $\hbar G$. Since the potential is periodic with spatial period of $\lambda_G = 2\pi/G$, only the transitions between the momenta that differ by integer multiples of $\hbar G$ are allowed. This periodicity allows the connection between a particle and the kicked rotor where the position of the particle can be folded into an angular coordinate $\hat{\theta} = \hat{x} \bmod (2\pi)$. The solutions are invariant under the translation of the wave function by one period of the potential and hence by the Bloch theorem [89] the quasimomentum is conserved. The dynamics of the rotor are then described in Raman-Nath regime [90], by a one-period evolution operator called the Floquet operator, given by [83]

$$\hat{\mathcal{U}} = \hat{\mathcal{U}}_{\mathrm{f}}\hat{\mathcal{U}}_{\mathrm{k}} = e^{-i\tau(\hat{\mathrm{N}}+\beta)^2/2}e^{-ik[1+\cos(\hat{\theta})]}. \tag{3.34}$$

Here $\hat{\mathrm{N}} = -i\frac{\mathrm{d}}{\mathrm{d}\theta}$ is the (angular) momentum operator with periodic boundary conditions. The first exponential on the right of Eq. (3.34), $\hat{\mathcal{U}}_{\mathrm{f}}$, is the free evolution of the atomic wave function between two consecutive pulses and the second factor, $\hat{\mathcal{U}}_{\mathrm{k}}$, represents the "kick" by each pulse. The e^{-ik} part of this operator merely introduces a "global" phase to the system by each kick, that we avoid carrying it through our derivations until we address it when writing the walk operators in Section 3.4.1. However, the periodic part of this operator, $e^{-ik\cos(\hat{\theta})}$, acts on the atoms as a thin phase grating. If we let $|\Psi_j\rangle$ be the wavefunction before a pulse and $|\Psi_{j+1}\rangle$ be the wavefunction immediately after the pulse:

$$|\Psi_{j+1}\rangle = \hat{\mathcal{U}}_{\mathrm{k}}|\Psi_j\rangle = e^{-ik\cos(\hat{\theta})}|\Psi_j\rangle \tag{3.35}$$

Mathematically, the fact that the standing light wave acts as a diffraction grating can be seen when we expand Eq. (3.35) as a series of Bessel functions using the identity $e^{iz\cos\theta} = \sum_{m=-\infty}^{\infty} i^m J_m(z)e^{im\theta}$. The result is

$$|\Psi_{j+1}\rangle = \sum_m (-i)^m J_m(k)|p_m\rangle, \tag{3.36}$$

where J's are the m^{th} order Bessel functions of the first kind, and $|p_m\rangle = e^{-im\hat{\theta}}$ represents a momentum state with momentum in the grating direction of $p_m = m\hbar G$. Here the Bessel functions give the coupling amplitudes between an initial n and final m momentum states. The properties of these functions are such that this amplitude will decay rapidly as the difference $|m-n|$ increases [85]. In fact, for $k \sim 1$ in an AOKR, only nearest neighbor momentum states are coupled such that $m = n \pm 1$.

The standing wave required for the kicking of the cold atoms can be made up using two counter-propagating linearly polarized Gaussian laser beams of the same wavelength and intensity. The resulting standing wave has intensity nodes separated by $\lambda_G = \lambda/(2\sin\theta_k)$ where θ_k is the angle that each kicking beam makes with the vertical (when the beams are not completely counter-propagating). This oscillatory intensity pattern translates into a periodic optical potential experienced by the atoms given by

$$U(r,z) = U_0 e^{-2r^2/w^2(z)} \cos^2(\pi z/\lambda_G), \tag{3.37}$$

where the z-axis is in the direction of the standing wave, r is the radial coordinate, and $w(z)$ is the beam waist. Figure 3.6 shows a schematic of an optical standing wave. By applying a short pulse of such a wave, the atoms will diffract to different momentum states with a distribution represented by Eq. 3.36. Also, the depth U_0 of this one-dimensional periodic potential depends on both the ground state polarizability and the laser intensity as [91]

$$U_0 = -\frac{8\pi}{c}\alpha_g(\omega) I. \tag{3.38}$$

Polarizability of the ground state is given by

$$\alpha_g(\omega) = |\langle g|\mathbf{D}\cdot\hat{\epsilon}\,|e\rangle|^2 \cdot \left(\frac{2\omega}{\omega^2-\omega_0^2}\right), \tag{3.39}$$

where ω is the laser frequency, $|g\rangle$ and $|e\rangle$ are the ground and excited states separated with the frequency ω_0, and $\mathbf{D}$ and $\hat{\epsilon}$ are the electric dipole matrix and the polarization vector respectively [91]. Eqs. (3.38) and (3.39) show that the kicking strength ($\propto U_0\Delta t$) depends on the laser detuning, the coupling between dipole moment and electric field, and the kicking pulse length, which is consistent with the definition of dimensionless kicking strength in Eq. (3.32).

Quantum Resonance

The evolution of the wave function from one kick to immediately after the next kick is given by the Floquet operator (Eq. (3.34)). Thus the wave function after j kicks is given by

$$|\Psi(j\tau)\rangle = \hat{\mathcal{U}}^j|\Psi(0)\rangle. \tag{3.40}$$

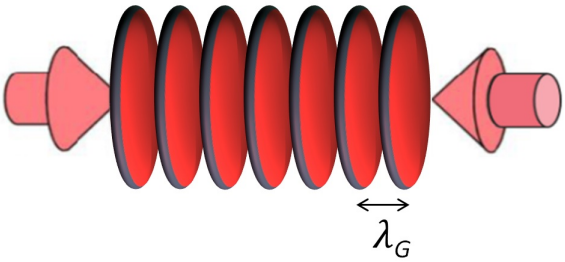

Figure 3.6: Schematic of an optical standing wave. Two counter-propagating laser beams create a one-dimensional periodic optical potential with intensity maxima separated by λ_G.

When the kicking period τ is an integer multiple of 4π, this corresponds to the Talbot time [92, 93]. In this case the free evolution operator will be unity and the effect of all the kicks add coherently which is equivalent to a single kick of strength $j \cdot k$. This is a quantum resonance and the Floquet operator after j kicks takes the form

$$\hat{\mathcal{F}} = \hat{\mathcal{U}}_{\mathrm{k}}^{j} = e^{-ijk\cos(\hat{\theta})}. \tag{3.41}$$

Assuming an initial momentum state $|0\rangle$, the probability for a momentum state $|n\rangle$ to be populated in the final state after j kicks is given by

$$\begin{aligned} P_n &= |\langle j|\hat{\mathcal{U}}^{j}|0\rangle|^2 \\ &= |\langle j|e^{-ijk\cos(\hat{\theta})}|0\rangle|^2 \\ &= J_n^2(jk) \end{aligned} \tag{3.42}$$

Then the mean energy of the ensemble at the end of jth kick is given by

$$\begin{aligned} \langle E\rangle &= \sum_{n=-\infty}^{\infty} n^2 P_n \\ &= \sum_{n=-\infty}^{\infty} n^2 J_n^2(jk) \\ &= \frac{1}{2} j^2 k^2. \end{aligned} \tag{3.43}$$

This shows that for a kicked rotor starting from the zero momentum state, the mean energy grows quadratically in time, a characteristic of the quantum resonance. Now we consider the evolution dynamics of a kicked rotor with a kicking period equal to the half-Talbot time, $T_{1/2}$, i.e. $\tau = 2\pi$ or any

odd multiple of 2π. Thus the wave function after a one-period evolution can be written as

$$\begin{aligned}
|\Psi(\tau = T_{1/2}\rangle &= e^{-ik\cos(\hat{\theta})} e^{-i\tau\hat{p}^2/2} |\Psi(0)\rangle \\
&= \sum_{n=-\infty}^{\infty} (-i)^n J_n(k) e^{-i\pi n^2} e^{-in\hat{\theta}} |\Psi(0)\rangle \\
&= \sum_{n=-\infty}^{\infty} (i)^n J_n(k) e^{-in\hat{\theta}} |\Psi(0)\rangle \\
&= \sum_{n=-\infty}^{\infty} (i)^{-n} J_{-n}(k) e^{in\hat{\theta}} |\Psi(0)\rangle \\
&= \sum_{n=-\infty}^{\infty} (i)^n J_n(k) e^{in\hat{\theta}} |\Psi(0)\rangle \\
&= e^{ik\cos(\hat{\theta})} |\Psi(0)\rangle, \qquad (3.44)
\end{aligned}$$

where the Bessel function property, $J_{-n}(k) = (-1)^n J_n(k)$ is used. Eq. (3.44) shows that when the kicking period is an odd multiple of half-Talbot time, the phase evolution between kicks changes the sign and results in a re-image of the grating transmission function which is inverse to the previous one. Thus the effect is that two kicks with a period equal to half-Talbot time cancel each other, recreating the original state and thus the mean energy will be oscillatory. This is called quantum anti-resonance. In general one can achieve the (anti-)resonance condition by imposing the condition $\tau = 2\pi\ell$, with positive integer ℓ and $\beta = 1/2 + l/\ell$, where $l = 0, 1, ..., \ell - 1$ [83, 85, 94]. Figure 3.7 shows the experimental results for the evolution of the momentum distribution of an AOKR at quantum resonance and anti-resonance, along with their corresponding temporal variations of the mean energy.

As we will see in the following sections, we employ the quantum resonance ratchet corresponding to an actual period of $T = T_T = 103$ μs, to have enough time to deliver the MW radiation required for a coin toss between the kicks (i.e. we have $t_M = 103$ μs in Eq. (3.20) as well).

3.3.2 Quantum Resonance Ratchet

A picture of the ratchet mechanism can be developed from a consideration of the gradient of the standing wave, which serves as a driving force on the wave function of atoms [45]. With this in mind, one can deduce that maximizing the wave function intensity at positions with larger potential gradients should

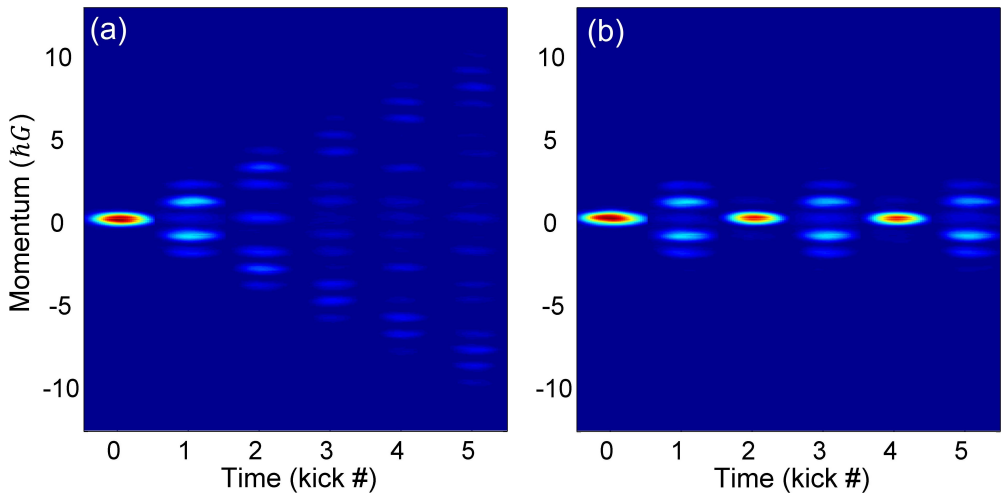

Figure 3.7: Experimental momentum distribution as a function of time (kick number) at (a) quantum resonance and (b) anti-resonance AOKR with $k = 1.8$.

result in a greater net force and accordingly higher possibility of ratchet creation [50]. In this picture, the sign of the potential gradient near the wave function's maxima will determine the direction of the ratchet. In order to create the spatially localized atomic wave function, an initial state composed of two or more plane waves can be utilized:

$$|\Psi\rangle = \sum_n e^{-in\phi}|n\rangle, \tag{3.45}$$

where $|n\rangle$ signifies the momentum state $|n\hbar G\rangle$, and ϕ is the offset phase [50]. The phase prefactors shift the maxima of the spatial wave function to where the potential gradient is greatest when $\phi = \pi/2$. It is also worth mentioning that setting the offset phases of each initial momentum states to be $e^{in\phi}$ is effectively equal to setting the offset phase of the potential to be ϕ.

Assuming that a single BEC has a narrow momentum width, its wave function in momentum space can be represented as $\Psi(p) = \delta p$, where p is the continuous momentum variable. This wave function can be Fourier transformed into position space to be studied in the frame of the standing wave. Thus the wave function in position space will be a plane wave a uniform spatial distribution ($|\Phi(x)| = \sqrt{G/2\pi}$), and according to the simple picture described above, no ratchet will be formed due to the absence of a net force on the atoms [50].

In contrast, if the initial state contains more than one plane waves, there will be the possibility of the

creation of a ratchet. The wave function of such a state can be written in position space as [50]:

$$\Phi(x) = A \sum_n e^{in\phi} e^{ip_n x/\hbar}, \tag{3.46}$$

where A is the normalization factor. In Figure 3.8.a we plot the population spatial distribution $|\phi(x)|^2$ and the standing wave potential together with $\phi = \pi/2$. This figure illustrates the population distribution for superpositions of two and seven consecutive plane waves. Note that, due to the $\phi = \pi/2$ offset phase, peaks of the population arise at positions where the standing wave happens to have the greatest gradient. As expected from a Fourier transformation, when the initial state is composed of more plane waves it becomes a more spatially localized wave function. That is the dashed line, corresponding to seven plane waves, shows a higher intensity with a noticeably reduced full width at half maximum (FWHM). As can also be inferred from Figure 3.8.b, where it can be seen that by increasing the number of consecutive plane waves in the initial state (that is, increasing the range of the momentum states of an initial state), the population peaks' FWHM decreases. These narrower wave functions not only experience a larger overall gradient, but also less gradient variation. Therefore a "cleaner" ratchet would be expected at higher number of plane waves in the initial superposition as can be seen in Figure 3.9.

As discussed above, the dynamics of the AOKR can be directed in $|n\rangle$ space (eigenvalues of momentum operator $\hat{\mathcal{N}}$, see discussion around Eq. (3.34)) by breaking the spatial-temporal symmetry of the problem [45, 82]. Experimentally, we realize this by the choice of the initial state:

$$|\Psi(n, \mathfrak{t} = 0)\rangle = \frac{1}{\sqrt{2}} \Big(|n = 0\rangle + e^{-i\phi} |n = 1\rangle \Big). \tag{3.47}$$

with $\phi = \pi/2$. To prepare this initial state, we apply a long (103 μs) far-off-resonant standing wave (Bragg pulse) on the initial external state of the BEC ($|n = 0\rangle$) [50, 51]. The Bragg pulse couples two momentum states with an interaction matrix given by

$$\hat{\mathbf{B}} = \begin{pmatrix} \cos(\frac{\Omega_B t_B}{2}) & e^{-i\phi_B} \sin(\frac{\Omega_B t_B}{2}) \\ -e^{i\phi_B} \sin(\frac{\Omega_B t_B}{2}) & \cos(\frac{\Omega_B t_B}{2}) \end{pmatrix}, \tag{3.48}$$

in which Ω_B is the effective Rabi frequency, t_B is the pulse length, and ϕ_B is the offset phase of the standing wave used for a Bragg diffraction. We achieve the equal superposition of external states given

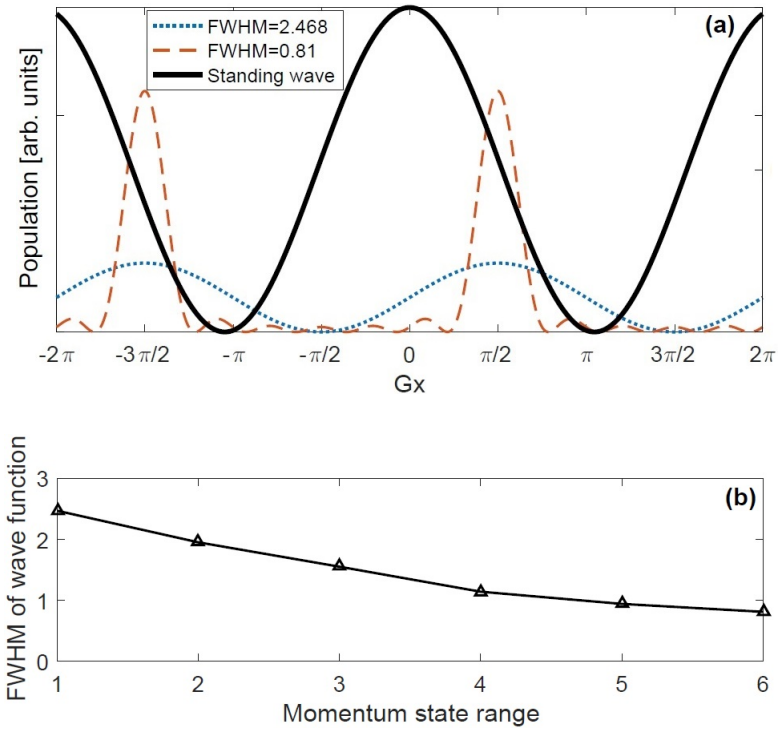

Figure 3.8: Panel (a) shows the atomic population for superpositions of two, $|n=0\rangle + e^{-i\pi/2}|n=1\rangle$ (dotted line), and seven, $\sum_{-3}^{3} e^{-in\pi/2}|n\rangle$ (dashed line) momentum states. The solid line represents the spatial distribution of the standing wave intensity (arbitrary unit). Panel (b) shows theoretical data for the atomic spatial distribution FWHM as a function of the number of consecutive momentum classes in the initial atomic state [50].

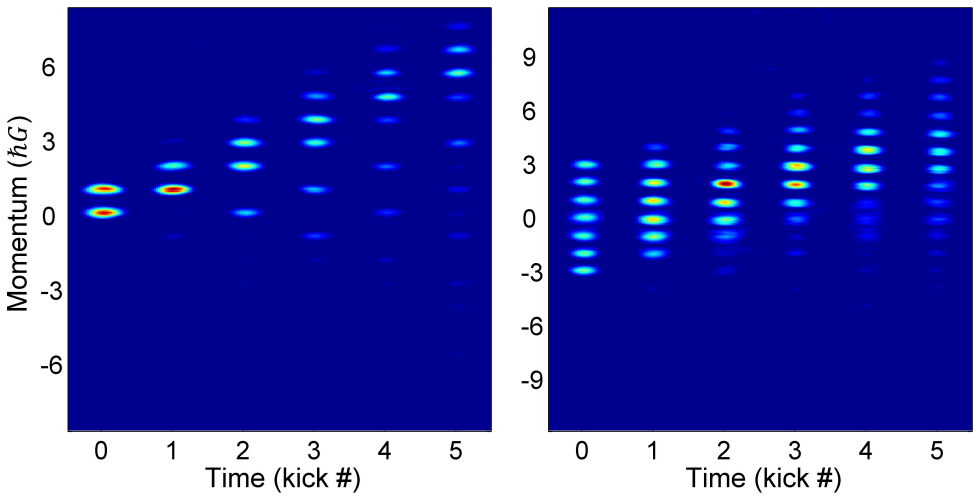

Figure 3.9: Experimental momentum distributions of the ratchets implemented with 2 (a) and 7 (b) initial states. The ratchet undergoes less dispersion when higher number of initial states are used.

in Eq. (3.47) by choosing $\phi_B = \pi/2$ and adjusting the Ω_B via the standing wave intensity, such that $\Omega_B t_B = \pi/2$ in Eq. (3.48) when $t_B = 103$ μs. By then applying the AOKR, the average momentum is shifted by an amount [52]

$$\langle \Delta\hat{p} \rangle = -\frac{k}{2}\sin(\phi) \tag{3.49}$$

after each pulse. Thus by choosing $\phi = \pi/2$ and $k \sim 2$, the average momentum can be either decreased or increased by one unit at each step of the walk depending on the sign of k. Recall that $k \propto 1/\delta_L$ in Eq. (3.32), so that with the light detuned with positive δ_L for $|1\rangle$ and negative δ_L for $|2\rangle$, these internal states experience ratchets in opposite directions, as can be seen in Figure (3.10) for a ratchet applied on the ^{87}Rb BEC with an equal superposition of internal states, $\frac{1}{\sqrt{2}}(|1\rangle + |2\rangle)$.

To realize the simplest quantum ratchet, the dynamics of the AOKR should meet the quantum resonance conditions that we achieve by applying the ratchet (kicking) pulses with $T = T_T = 103$ μs [45, 50, 51, 95].

3.4 Quantum Walk Sequence

We initialize the walks by starting from the state $\frac{1}{\sqrt{2}}\left(|n=0\rangle + e^{-i\pi/2}|n=1\rangle\right)$, prepared with a Bragg pulse, and then applying a $\pi/2$ MW pulse with phase $\chi = \pi$ (see Eq. (3.22)). This is a so-called

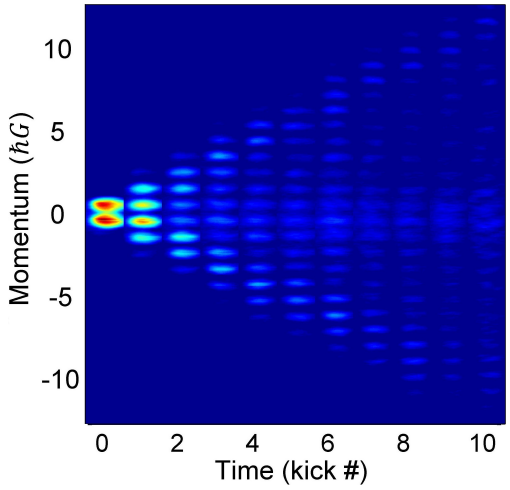

Figure 3.10: Opposite directions of the ratchet momentum currents each corresponding to one of the two internal states of ^{87}Rb atoms; $F = 1$ and $F = 2$. This bi-directional ratchet is realized using an initial state composed of an equal superposition of these two states; $\frac{1}{\sqrt{2}}(|1\rangle + |2\rangle)$.

Hadamard gate and gives an equal superposition of the internal states,

$$\hat{\mathbf{M}}(\pi/2, \pi)|1\rangle = \frac{1}{\sqrt{2}}(|1\rangle + |2\rangle), \tag{3.50}$$

at both external states, $|n = 0\rangle$ and $|n = 1\rangle$. Thereafter, we apply a coin toss pulse $\hat{\mathbf{M}}(\pi/2, -\pi/2)$ as presented in Eq. (3.27) after each shift operator (step of the walk). We note that these particular choices of gate and coin toss matrices will produce a symmetric walk. After each shift, the coin toss matrix acts on the internal state producing a strong mixing of internal and external degrees of freedom during the temporal evolution.

3.4.1 Standard Walk

In order to implement a standard quantum walk with j steps, we use a sequence of $\hat{\mathbf{U}}_{\text{step}}$ operators as:

$$\hat{\mathbf{U}}_{\text{walk}} = \left(\hat{\mathbf{U}}_{\text{step}}\right)^j = \left[\hat{\mathbf{T}}\hat{\mathbf{M}}(\pi/2, -\pi/2)\right]^{j-1}\left[\hat{\mathbf{T}}\hat{\mathbf{M}}(\pi/2, \pi)\right], \tag{3.51}$$

where $\hat{\mathbf{M}}(\pi/2, -\pi/2)$ and $\hat{\mathbf{M}}(\pi/2, \pi)$ are the Hadamard gate and coin toss operators and $\hat{\mathbf{T}}$ is the internal-state-dependent shift operator presented in Eq. (3.28). This operator, which affects the system

by applying each kick ($\hat{\mathcal{U}}_{\rm k}$ in Eq. (3.34)) can also be written in matrix representation as [96]:

$$\hat{\mathbf{T}} = e^{-ik[1+\cos(\hat{\theta})].\sigma_z} = \begin{pmatrix} e^{-ik[1+\cos(\hat{\theta})]} & 0 \\ 0 & e^{ik[1+\cos(\hat{\theta})]} \end{pmatrix}, \tag{3.52}$$

where either diagonal element addresses one of the internal state. Note that the signs of the kicking strengths are opposite due to the fact that the kicking light detuning is opposite with respect to either internal state (see Eq. (3.32) and discussion around Eq. (3.49)). Also as mentioned before, the $e^{\pm ik}$ prefactors in the kick operator introduce phases of $\phi_1 = -k$ and $\phi_2 = +k$ to either internal state. This imposes a phase difference of

$$\Delta\phi = \phi_2 - \phi_1 = 2k \tag{3.53}$$

between the $|1\rangle$ and $|2\rangle$ states [96]. If this phase difference is not compensated at each walk step, it will result in a phase distortion and adversely affect the symmetry of the walk. This issue was addressed by introducing an additional phase of $2k$ to the coin toss MW pulses. Then the remainder of the shift operator corresponding to the spatially periodic potential of the kicking operator will be:

$$\hat{\mathbf{T}} = \begin{pmatrix} e^{-ik\cos(\hat{\theta})} & 0 \\ 0 & e^{ik\cos(\hat{\theta})} \end{pmatrix}. \tag{3.54}$$

This operator, when used in a ratchet configuration, can shift the momentum by $\pm q$ depending on the internal state as [23]:

$$\hat{\mathbf{T}} = \begin{pmatrix} e^{iq\hat{\theta}} & 0 \\ 0 & e^{-iq\hat{\theta}} \end{pmatrix}, \tag{3.55}$$

with q being an integer in units of $\hbar G$. This operator is the matrix representation of Eq. (3.28) with position and momentum expressed in their re-scaled units. In our usual walk setup, $q = 1$ which corresponds to nearest neighbor coupling in momentum space. In other words, the unitary shift operator can be written as:

$$\hat{\mathbf{T}} = \begin{pmatrix} |n+1\rangle\langle n| & 0 \\ 0 & |n-1\rangle\langle n| \end{pmatrix}, \tag{3.56}$$

which can shift the external state by +1 (-1) when applied on a system with $|1\rangle$ ($|2\rangle$) internal stare. Figure (3.11.a) represents the timing scheme of the corresponding operators after preparing the initial state with a Bragg pulse. The entire experimental procedure of the standard quantum walk is also illustrated in Figure (3.11.b).

3.4.2 Walk Reversal

Since the walk evolves unitarily and coherently, it is possible to reverse all steps taken in the walk. If the walk has taken j steps, applying the Hermitian conjugate of the step operator $\hat{\mathbf{U}}^{\dagger}_{\text{step}} = \hat{\mathbf{M}}(\pi/2, \pi/2)\ \hat{\mathbf{T}}^{\dagger}$ for an additional j steps should revert the system to its original state. The conjugate of the shift operator can be realized using two Pauli-like (rotation) matrices as [52, 97]:

$$\hat{\mathbf{T}}^{\dagger} = \hat{\mathbf{M}}(\pi, \pi/2)\ \hat{\mathbf{T}}\ \hat{\mathbf{M}}(\pi, -\pi/2). \tag{3.57}$$

Thus a complete reversal of the walk will include:

$$\hat{\mathbf{U}}^{\dagger}_{\text{walk}}\ \hat{\mathbf{U}}_{\text{walk}} = \left\{ \left[\hat{\mathbf{M}}^{\dagger}(\pi/2, \pi)\ \hat{\mathbf{T}}^{\dagger}\right] \left[\hat{\mathbf{M}}(\pi/2, \pi/2)\ \hat{\mathbf{T}}^{\dagger}\right]^{j-1} \right\} \left\{ \left[\hat{\mathbf{T}}\hat{\mathbf{M}}(\pi/2, -\pi/2)\right]^{j-1} \left[\hat{\mathbf{T}}\hat{\mathbf{M}}(\pi/2, \pi)\right] \right\} \tag{3.58}$$

that after multiplying the intermediate $\hat{\mathbf{M}}$ operators leads to:

$$\begin{aligned} \hat{\mathbf{U}}^{\dagger}_{\text{walk}}\ \hat{\mathbf{U}}_{\text{walk}} = &\left[\hat{\mathbf{M}}^{\dagger}(\pi/2, \pi)\ \hat{\mathbf{M}}(\pi, \pi/2)\right] \left[\hat{\mathbf{T}}\ \hat{\mathbf{M}}(\pi/2, \pi/2)\right]^{j-1} \\ &\left[\hat{\mathbf{T}}\ \hat{\mathbf{M}}(\pi, -\pi/2)\right] \left[\hat{\mathbf{T}}\ \hat{\mathbf{M}}(\pi/2, -\pi/2)\right]^{j-1} \left[\hat{\mathbf{T}}\ \hat{\mathbf{M}}(\pi/2, \pi)\right] \\ = &\ \hat{\mathbb{I}} \end{aligned} \tag{3.59}$$

Thus in principle we are able to realize a walk reversal and recover the initial state of the system by applying the sequence of the operators given in Eq. (3.59). Figure 3.12 shows the timing scheme of the Bragg, ratchet, and MW pulses used in our quantum walk reversal experiments.

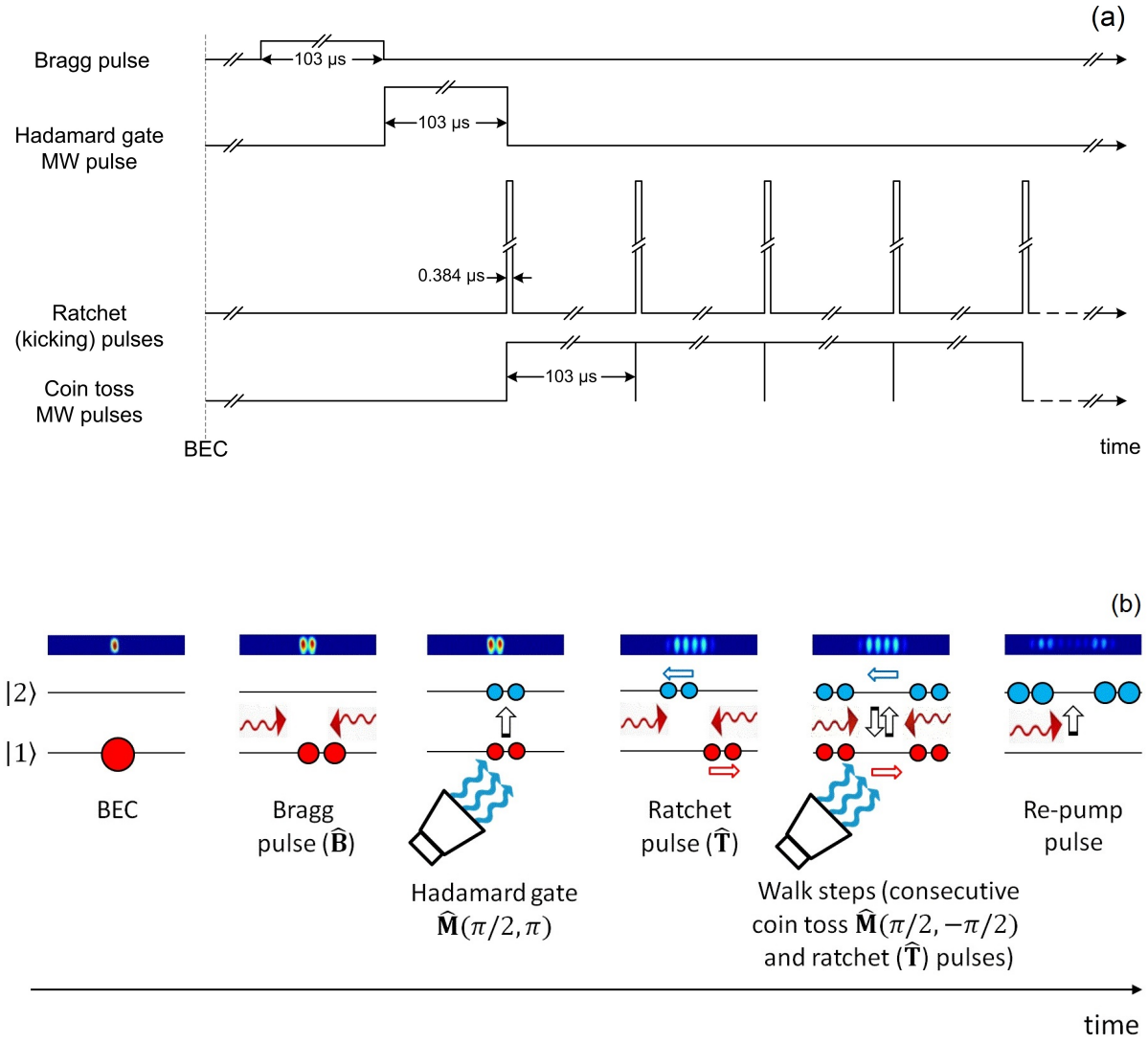

Figure 3.11: Panel (a) shows the timing scheme of the Bragg, ratchet, and MW pulses used in our quantum walk experiments. Panel (b) is the level diagram representation of the entire experimental procedure of these walks.

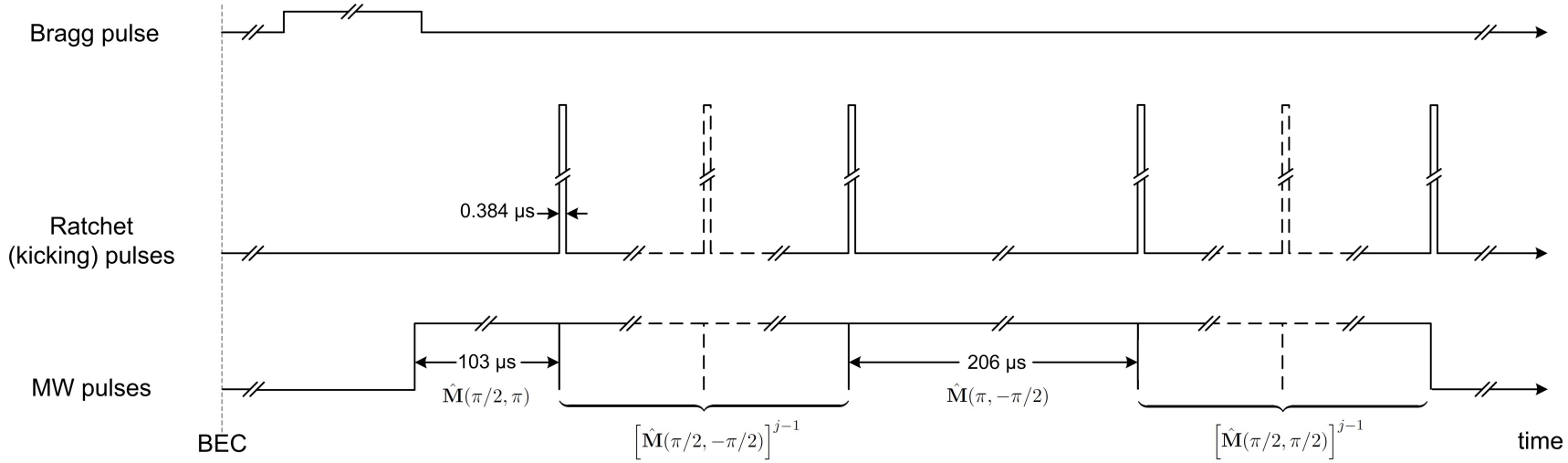

Figure 3.12: Timing scheme of the Bragg, ratchet, and MW pulses used in our quantum walk reversal experiments.

Chapter 4

Experimental Setup

With the advent of laser cooling and trapping as well as the evaporative technique, alkali atoms became the best candidates for realizing BEC since their optical transitions can be addressed by available lasers. In this regard, we used an atomic vapor of ^{87}Rb that could be trapped and cooled by using inexpensive diode lasers at a wavelength of 780 nm. The experimental procedure was composed of three main sequences including the BEC creation, quantum walk procedure (which itself consisted of different MW and optical standing wave pulses), and the imaging. Each sequence required a separate setup that will be described in the following sections.

4.1 BEC Creation

The BEC creation itself consisted of several consecutive phases, including the MOT creation with MOT and re-pump beams, Doppler cooling, loading of atoms into the dipole trap, and evaporative cooling. The setups to perform these steps are explained in the following subsections and the procedure to create the BEC is elaborated in Section 4.1.3.

The BEC setup was divided into two optical tables namely the “laser table” and the “BEC table”. The BEC table was isolated with thick curtains from the rest of the lab to minimize the insertion of stray lights into the BEC chamber, and therefore the MOT, re-pump, imaging and kicking laser light were all imported using optical fibers from the laser table located in a separate area.

4.1.1 Laser Table

MOT, Cooling, and Imaging Lasers

The three different laser frequencies required for MOT creation, Doppler cooling and the imaging were all generated in one optical setup. This setup was composed of two sets of lasers and optics including the master laser associated with its injection-locked slave lasers, and the re-pump laser. The latter will be described in the next subsection. The master laser was a grating stabilized TOPTICA, DL100 laser in a temperature-controlled housing. This laser, operating at continuous-wave mode with about 20 mW output power, was frequency-locked to the transition between the $5^2S_{1/2}, F = 2$ ground state and the crossover line between the $5^2P_{3/2}, F' = 2$ and $F' = 3$ excited states (Figure 4.1). Since the output power from the master laser was quite low, three other homemade diode lasers referred to as slave lasers were used as amplifiers. Each slave laser was a $\sim$100 mW continuous-wave laser diode in a temperature-controlled housing. Following the injection-locking techniques, modes of the slave lasers were identical to the mode of the master laser.

The optical setup used to generate the required detunings is shown in Figure 4.2. The collimated laser beam from the laser was initially elliptical in shape, passing through a pair of anamorphic prisms so as to change the profile into a circular shape. A half-wave ($\lambda/2$) plate placed immediately after the prism pair rotated the polarization of the light so that all the light went through a polarizing beam splitter cube (PBSC) that was placed with its rotation axis at 45° to the vertical. The light was then sent through a Faraday rotator which rotated the polarization of light coming from the left 45° clockwise, making it horizontally polarized. Any reflected horizontally polarized light passing from the right through the Faraday rotator had its plane of polarization rotated in the other direction so that the light was reflected (eliminated) by the PBSC placed in front of the laser. Thus the master laser was isolated from any reflected and scattered light. A small portion of light coming out from the master laser was used to perform saturation absorption spectroscopy, the basis of the frequency locking technique. The lasers were isolated from any reflected and scattered light by means of isolators (Faraday rotators) and half-wave plates.

About 10 mW of light of each laser was sent to the next laser for injection-locking by means of a beam splitter. In order to monitor whether each slave frequency followed the injection laser or not a small fraction of it ($\sim$ 200 μW) was directed through a ^{87}Rb vapor cell using a partial reflector. The

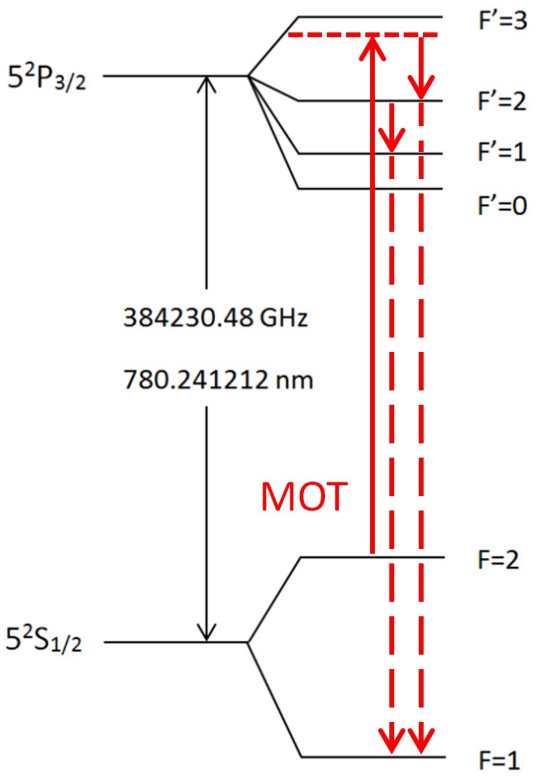

Figure 4.1: Optical transition used in ^{87}Rb MOT creation. Atoms are optically excited from $5^2S_{1/2}, F = 2$ to the crossover line between the $5^2P_{3/2}, F' = 2$ and $F' = 3$ levels. The excited atoms can then decay to the $5^2P_{3/2}, F' = 2$ and $F' = 1$ levels (due to the power broadening) and therefrom to the $5^2S_{1/2}, F = 1$ ground state.

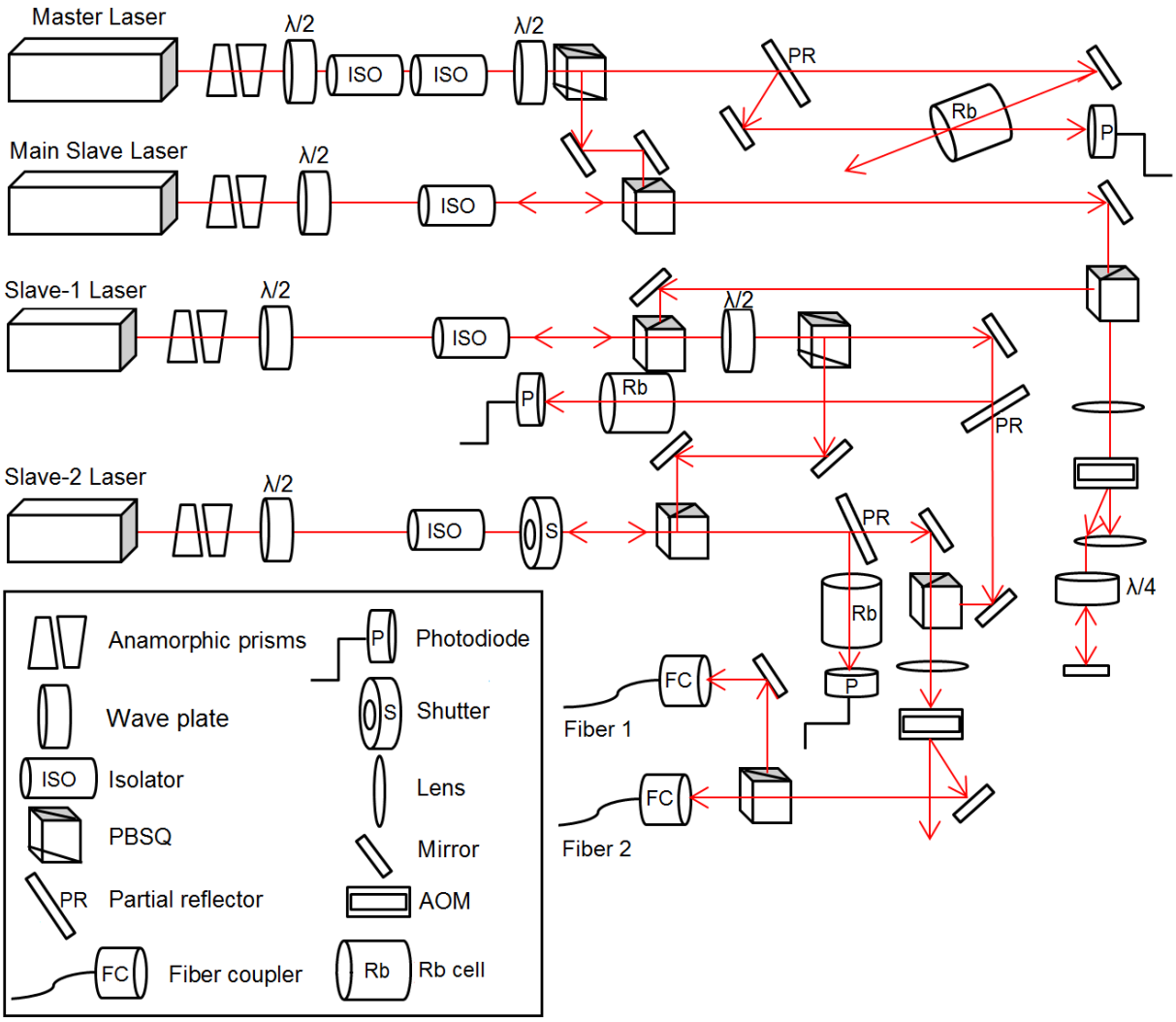

Figure 4.2: Optical setup on the "laser table" used to prepare the frequency-stabilized lights required for the MOT, cooling, and imaging. The laser beams were then coupled into polarization maintaining fibers and transferred to the "BEC table".

transmitted lights were then monitored using photodiodes (Thorlabs; DET-210, PDA-400, or homemade FDS010, FDS100) and the frequency was said to be following the injection if an absorption dip was observed on the oscilloscope.

In order to realize an appropriate BEC with a high signal-to-noise ratio, precise control of the laser frequency was crucial. Lasers stabilized at four different frequencies were required:

1. -15 MHz detuning from the $5^2S_{1/2}, F = 2 \rightarrow 5^2P_{3/2}, F' = 3$ transition to create the MOT,
2. -80 MHz detuning from the $5^2S_{1/2}, F = 2 \rightarrow 5^2P_{3/2}, F' = 3$ transition for optical molasses (Doppler cooling),
3. light on resonance with the $5^2S_{1/2}, F = 2 \rightarrow 5^2P_{3/2}, F' = 3$ transition for imaging the atoms,
4. light on resonance with the $5^2S_{1/2}, F = 1 \rightarrow 5^2P_{3/2}, F' = 2$ transition (re-pump light described in the next section).

The first three requirements were met by using several acousto-optic modulators (AOMs) controlled by LabView program; the master laser was locked at a frequency of 133.3 MHz below the MOT transition. After being injection-locked to the master laser, the light from the main slave was double-passed through an AOM (ISOMET 1205C-2) excited with an RF frequency of f_{AOM} as shown in Figure 4.3. This AOM was used to detune the stabilized frequency of the master laser by three different amounts as will be described shortly. Taking the positive first order on each pass through the AOM gave a frequency for the slave light of $f = f_0 + 2f_{\mathrm{AOM}}$, where f_0 was master laser's frequency. This light was then used for the injection locking of the other slave lasers referred to as slave-1 and slave-2. The advantage of using the double pass AOM was that use of different frequencies would not cause a deflection of the beam, which was very important in the alignment. A telescopic configuration of two lenses was used for this purpose so that the retro-reflected first order beam from the mirror after the second lens co-propagated with the original beam before the AOM.

The beams from the slave-1 and slave-2 lasers were sent together through another AOM (ISOMET 1205C-1) which was driven at frequency of 80 MHz. The negative first order ($f' = f$-80 MHz) was separated into two beams by using a PBSC and then sent to the BEC optical table by using two polarization-maintaining single-mode fibers referred to as fiber-1 and fiber-2. It is worthy of note that the coupling efficiency of the fiber depends on the shape and size of the laser beam. Thus using two lenses in a telescopic configuration before the fiber enhanced the coupling efficiency significantly. The final detun-

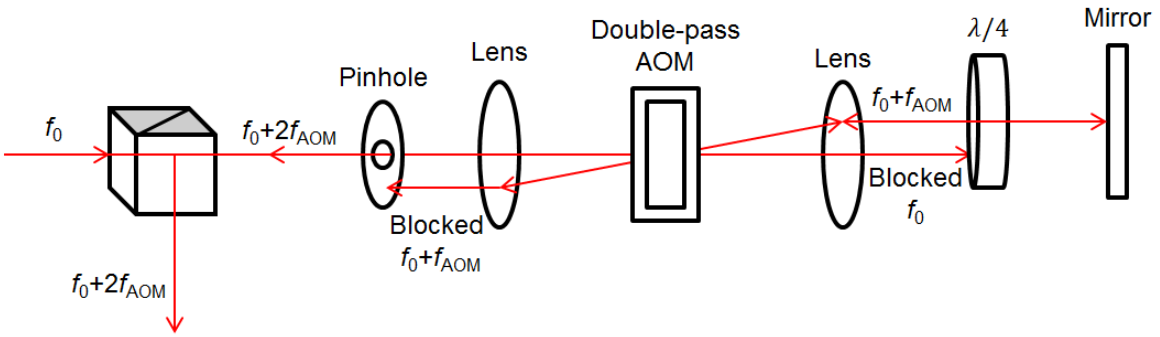

Figure 4.3: A double pass AOM setup. The first order diffracted beam from the AOM placed in between two lenses in a telescopic configuration is retro-reflected and passed through the AOM again. The first order diffracted beam after the second pass co-propagates with the original beam. This light was made orthogonally polarized by sending it twice through a quarter wave plate. It should be noted that the path of the diffracted beam in this setup does not deflect in position, a crucial requirement in the laser cooling and trapping setup.

ing from the $5^2S_{1/2}, F = 2 \rightarrow 5^2P_{3/2}, F' = 3$ transition achieved on the light entering the vacuum chamber can be calculated using the equation [72]:

$$\delta = -133.3\ (\text{MHz}) + 2f_{\text{AOM}} - 80\ (\text{MHz}). \tag{4.1}$$

Thus the f_{AOM} was adjusted at 99.15, 66.5 and 106.65 MHz to obtain the -15, -80, and 0 MHz detunings required for the MOT, Doppler cooling, and imaging, receptively.

Re-pump Laser

Due to the power broadening mechanism, there is always some possibility that atoms excited to the $5^2P_{3/2}, F' = 3$ state by the MOT light decay to the $5^2P_{3/2}, F' = 2$ and $F' = 1$ levels and therefrom to the $5^2S_{1/2}, F = 1$ ground state (see Figure 4.1). Thus, without further intervention the MOT would disappear quickly. To prevent this and maintain a closed "cycling" transition an additional laser called the re-pump laser is needed. The re-pump laser depopulates the $5^2S_{1/2}, F = 1$ state, as shown in Figure 4.4, in order to maintain the cycling transition for the MOT.

The re-pump laser was a grating stabilized TOPTICA, DL100 laser in a temperature controlled housing which was frequency-locked to the transition from the $5^2S_{1/2}, F = 1$ state to the crossover line between the $5^2P_{3/2}, F' = 1$ and $F' = 2$ states. The optical alignment of the re-pump laser was similar

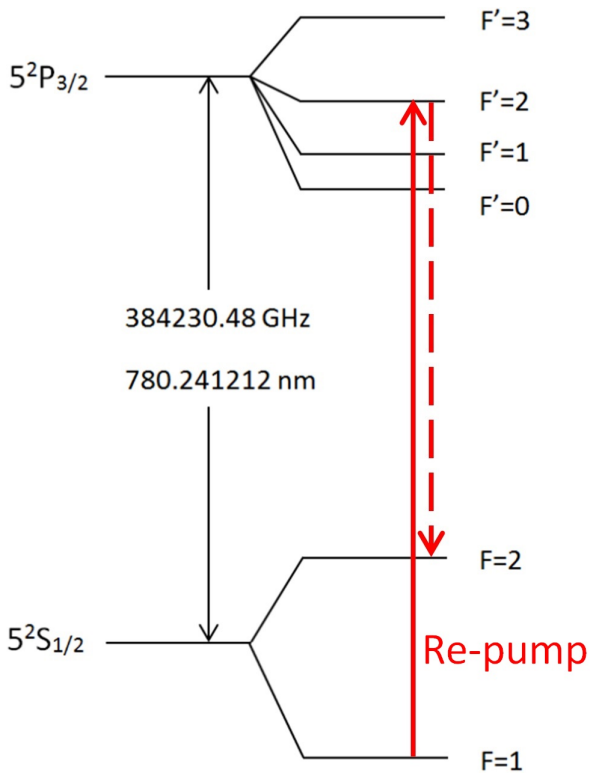

Figure 4.4: The re-pump transitions in ^{87}Rb atoms used for re-populating the $5^2S_{1/2}, F = 2$ state to maintain the MOT cycling. The $5^2S_{1/2}, F = 1$ atoms are excited to the $5^2P_{3/2}, F' = 2$ state by the re-pump laser and then decay to $5^2S_{1/2}, F = 2$ state to undergo the MOT transition. Without re-pumping, the MOT process would terminate quickly due to the decay of atoms (excited via MOT transition) to the $5^2S_{1/2}, F = 1$ state.

to that of the master laser as described above and is shown in Figure 4.5. The laser beam was double passed through an ISOMET 1205C-2 AOM and the positive first order beam after the second pass was coupled into the fiber-2 and delivered to the "BEC table" along with the MOT beam. This light enabled the atoms to be excited from the $5^2S_{1/2}, F = 1$ ground state to the $5^2P_{3/2}, F' = 2$ excited state and thus to eventually decay to the $5^2S_{1/2}, F = 2$ state.

4.1.2 BEC Optical Table

The heart of the experiment was located on the BEC optical table where all laser beams were sent into the vacuum chamber. Six main systems were located on this table; 1) the MOT and re-pump appendix setup to complete the MOT creation, 2) the CO_2 laser system used for loading and evaporative cooling, 3) the vacuum chamber in which the BEC was created associated with the magnetic coils, 4) the kicking setup, 5) the imaging setup and 6) the MW generator and transmitter. The first three configurations were

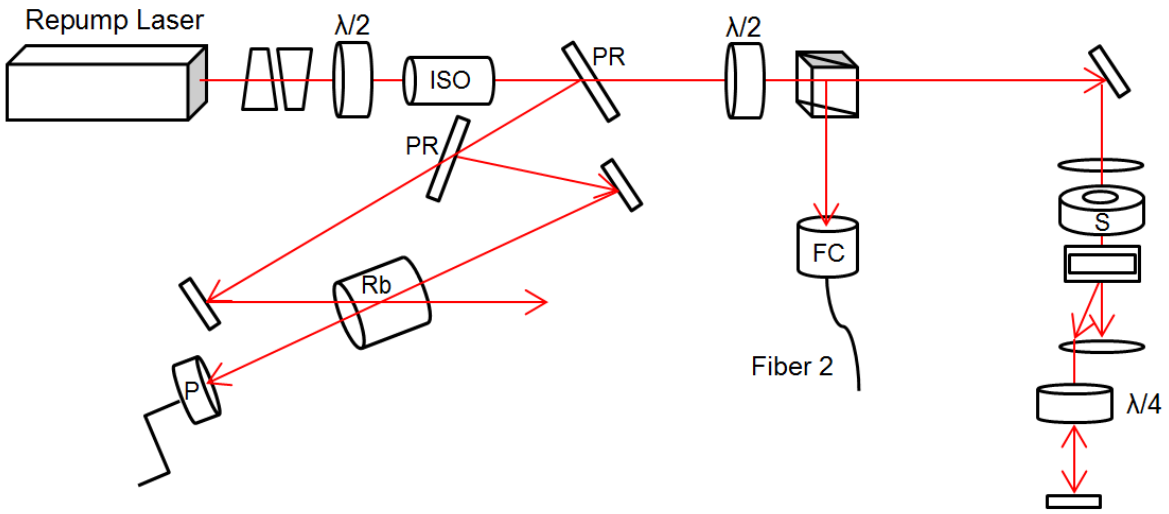

Figure 4.5: Optical setup for the re-pump laser.

used to complete the BEC process. The latter three setups will be described later in their corresponding sections.

MOT Completion Setup

The setup for completing the MOT process is shown in Figure 4.6. The main portion of the light exiting fiber-1 was used as the MOT beam and a small portion of that was taken as an imaging beam using a partial reflector. Fiber-2 contained the MOT beam (split into two by a polarizing beam splitter cube to form Beam 2 and Beam 3) and a re-pump beam. The MOT and re-pump beams were then expanded to $\sim$1 inch diameter by means of a combination of two lenses and were separately sent through quarter-wave ($\lambda/4$) plates to make the light circularly polarized. These three expanded MOT beams were sent into the vacuum chamber and were retro-reflected using mirrors. Each of the retro-reflected beams was sent through an additional $\lambda/4$ wave plate so that the three pairs of MOT beams would have correct $\sigma^+ - \sigma^-$ combinations. These three counter-propagating beams were aligned to intersect at the center of the chamber, with the MOT appearing at the intersection of the beams. During the experiment, the imaging, the MOT and the re-pump beams were blocked at different times. In order to facilitate this, these beams were passed through fast electronic shutters (UNIBLITZ, LS2T2) controlled by the LabView program.

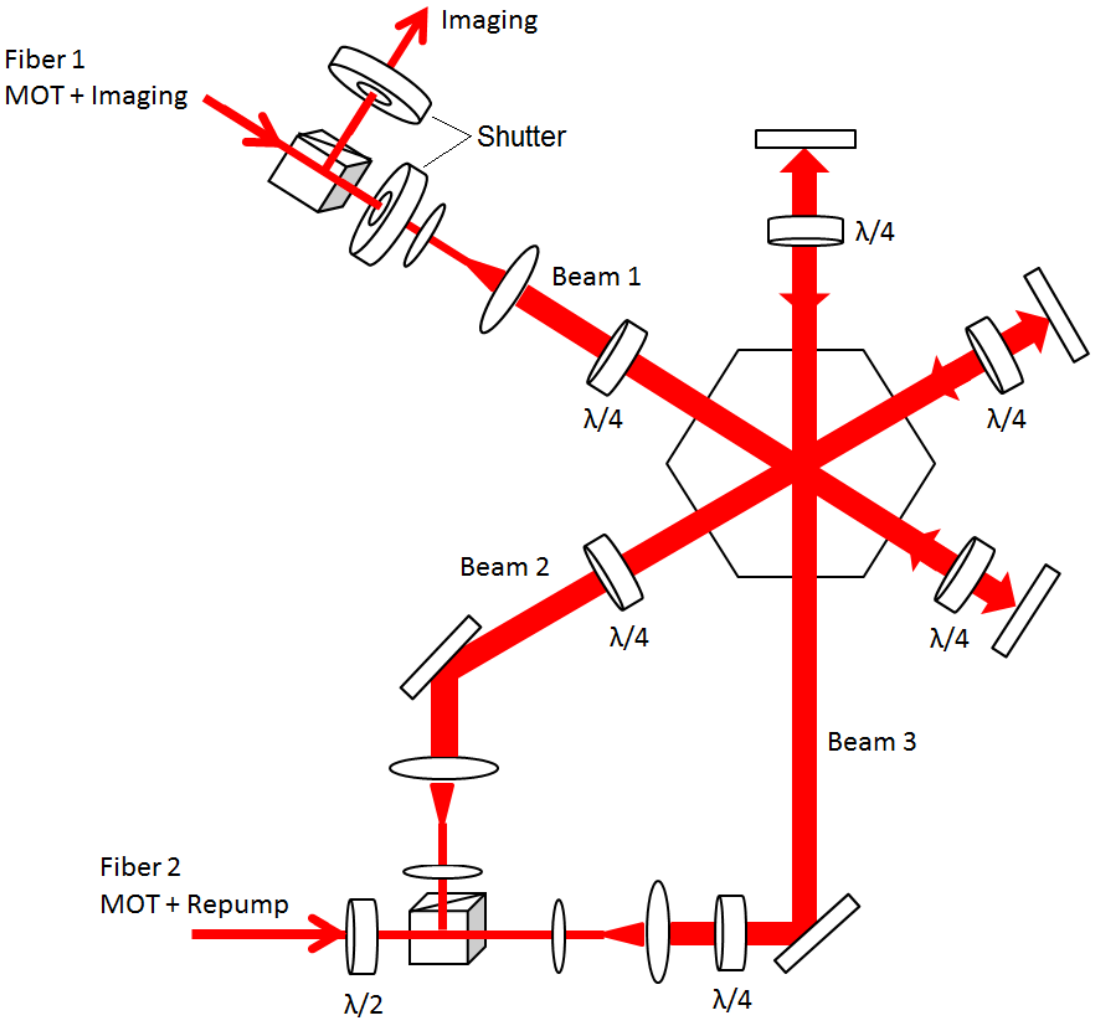

Figure 4.6: Setup on the "BEC table" for completing the MOT process.

CO_2 Laser System

A 50 W continuous-wave laser beam at 10.6 μm wavelength was used as a far-off-resonance trap (FORT) to perform the evaporative cooling. This beam originated from a COHERENT, GEM Select-50 CO_2 laser powered by an Agilent, 6573A DC power supply. Due to the high absorption coefficient of glass and quartz at 10.6 μm, the usual optics for the near infrared MOT lasers could not be used. One of the materials with the lowest absorption coefficient at this wavelength is Zinc-Selenide (ZnSe). Lenses and viewports were made of this material.

The FORT laser beam was directed to the vacuum chamber as shown in Figure 4.7. The beam was passed through a water cooled AOM (IntraAction Corp., AGM 406-B1) driven by an IntraAction Modulator Driver Model GE-4030H which was electronically controlled by using an analog voltage signal from the computer. The zeroth order AOM beam was sent to a beam dump and the first order beam ($\sim$30 W) was transported into the chamber through an assembly of three lenses. The first two lenses formed a beam expander in a telescopic configuration followed by a third focusing lens of 1.5 inches focal length which was installed inside the vacuum chamber. The beam was directed into the chamber through a 1 inch diameter ZnSe viewport. The final spot size of the beam at the center of the chamber is $w_0 = \lambda f/(\pi R)$ where R is the radius of the beam incident on the third lens and f is the focal length of the lens. For the loading and evaporative cooling phases, the beam waist (w_0) was set at either a large or small size respectively. In order to facilitate this, the second lens of the beam expander was mounted on a translation stage (Aerotech, 101SMB2-HM) controlled by a Soloist driver interface.

Vacuum Chamber

All experiments concerning the creation and manipulation of BEC were carried out inside the vacuum chamber. The vacuum system (MDC Vacuum Products), shown in Figure 4.8, consisted of a six-way cross made of stainless steel with an octagonal multiport chamber attached to one of its flanges. The chamber had four 2.0 inch diameter antireflection coated quartz viewports for the MOT and kicking beams, four 1.0 inch diameter ZnSe viewports for CO_2 beam, and two 5.0 inch diameter quartz viewports (one attached to the open side of the six-way cross and the other attached to the large opening on the orthogonal chamber) used for MOT and imaging beams. The vacuum system was previously assembled and pumped the chamber in several phases to attain the vacuum of $\sim 10^{-10}$ Torr.

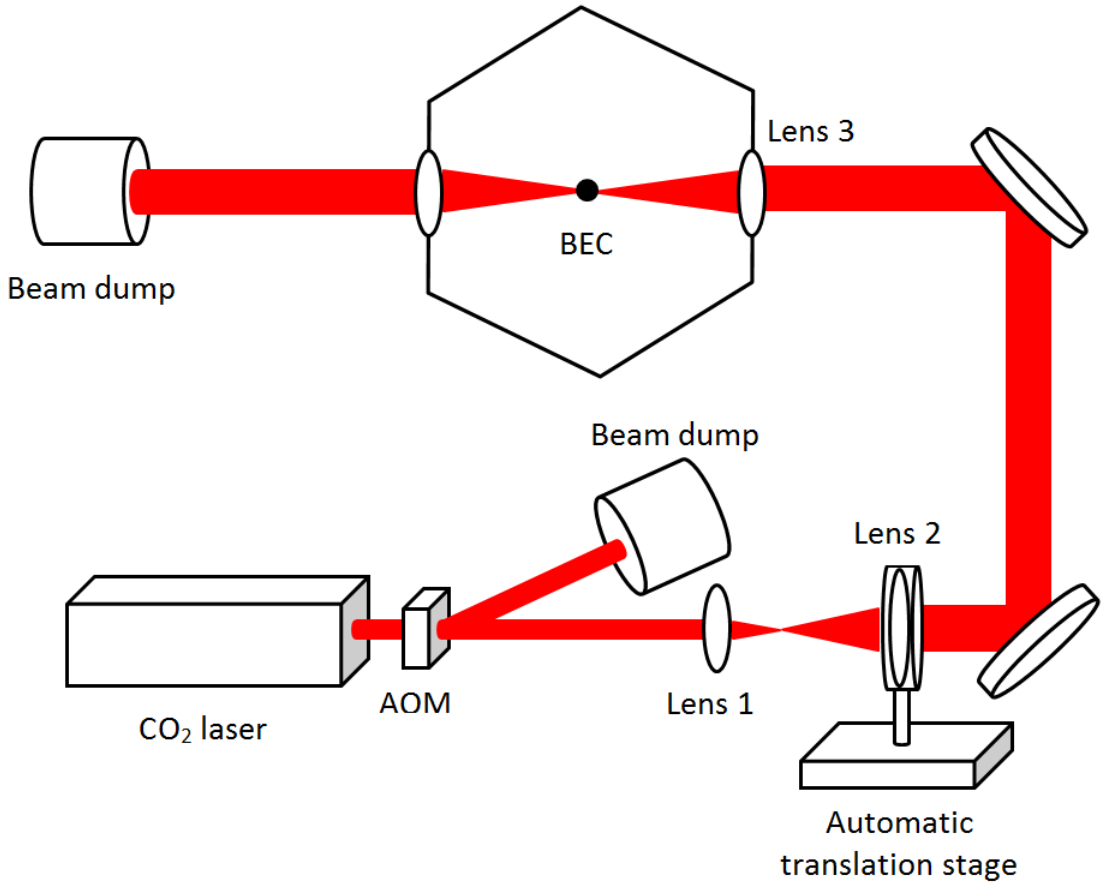

Figure 4.7: CO_2 laser setup used for loading the atoms into the dipole trap and evaporative cooling.

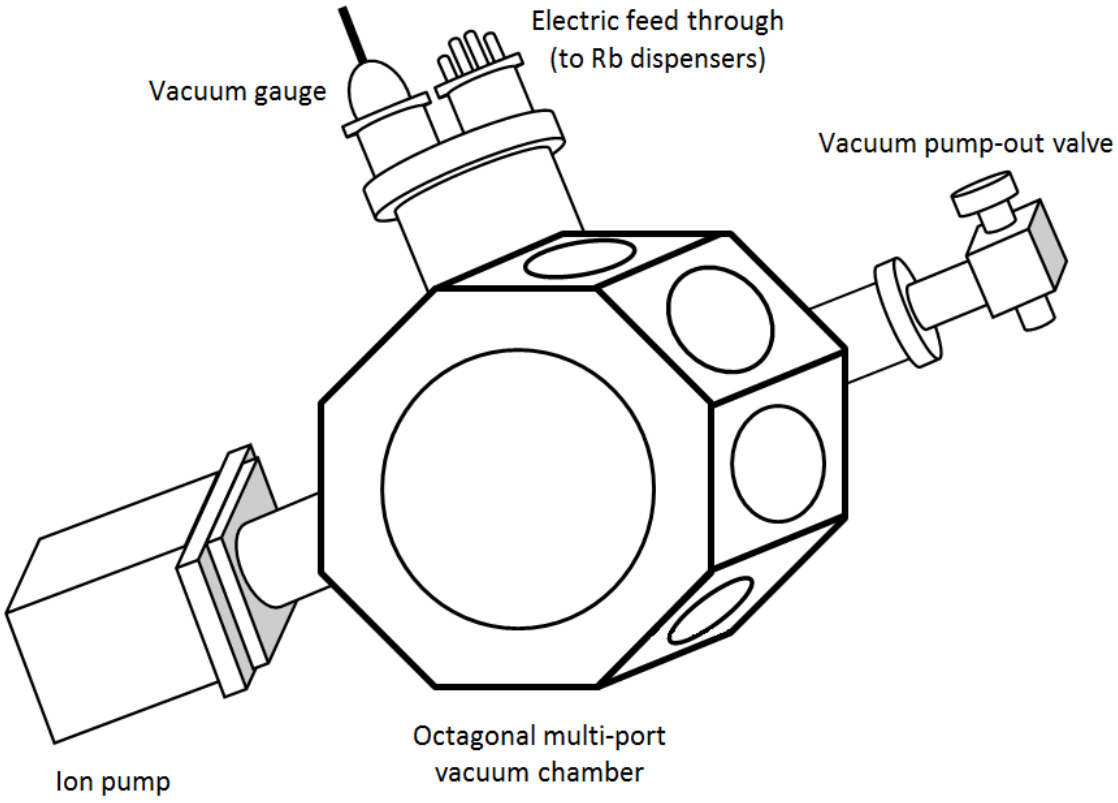

Figure 4.8: Schematic of the vacuum system showing the six-way cross and an octagonal multi-port chamber.

An automatic Varian style 8 liter/s ion pump powered by Terrenova-751 controller was attached to the system to keep the chamber at this pressure all the time. The vacuum chamber was shielded from the ion pump's magnetic field using μ-metal magnetic shields.

The magnetic field required for trapping of the atoms in the MOT was provided by a pair of coils, referred to as the main coils, in anti-Helmholtz configuration (two identical coils separated by a distance equal to their radius, and currents flowing in opposite directions as shown in Figure 4.9). The coils had a radius of 3.0 inches and consisted of 5×5 layers (25 turns) of copper tube with a square cross-section of external dimension of 0.125 inch and internal dimension 0.016 inch. These coils were mounted around the large viewports of the vacuum chamber with their common axis along the symmetry axis of the chamber. In order to create the MOT, about 16 A current was supplied to produce an inhomogeneous magnetic field between the coils ($\sim$ 16 G/cm) with a vanishing field at the center. This current was controlled with the LabView program by applying a 0-5 V analog signal to a 400-A DC current supply.

Additionally, three pairs of coils were positioned on all six sides of the vacuum chamber to nullify the Earth's magnetic field and any stray field produced by other sources, mainly the ion pump. Each pair of coils had currents flowing in the same direction fed by a separate voltage-to-current converter circuit that was controlled via LabView program.

4.1.3 BEC Creation Procedure

The BEC process started by creating a MOT of about 30 million atoms, and then a high power beam from CO_2 laser ($\sim$30 W) was directed to the MOT as described in Section 4.1.2. The focused CO_2 laser beam at a wavelength of 10.6μm, which was far detuned from the atomic transition, formed a far off-resonant trap (FORT) and overlapping this beam with the AOM for about 20 seconds loaded the atoms in the FORT.

Then the power on the re-pump laser beam, which was originally adjusted at $\sim$2 mW to create the MOT, was reduced by a factor of $\sim$100 to make a temporal dark SPOT [98]. This was a crucial step for effective loading, where the atoms started entering into a state that was "dark" to the cooling light. The resultant decrease in the recoil heating and the excited state collisions led to an increase in the phase space density. The detuning of the cooling light was then changed to -80 MHz so that even after the consideration of the ac-stark shift between the ground and the excited states which reduced their energy difference, the atoms still saw the MOT beams negatively detuned. About 60 ms later, the MOT beams

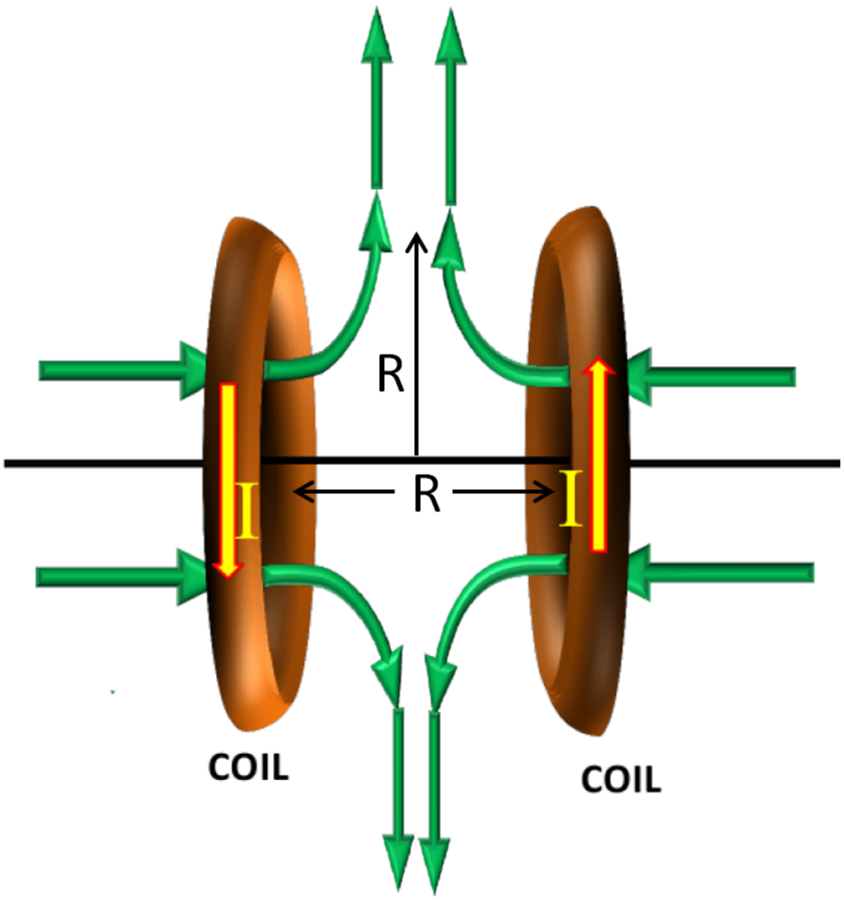

Figure 4.9: Schematic drawing of the MOT coil system. The pair of coils is placed in anti-Helmholtz configuration to produce a zero magnetic field and an approximately linear field gradient in all directions near the center.

and re-pump beam were extinguished by using fast electronic shutters and the magnetic field was turned off by reducing the current on the coils to zero. This finally gave about 6 million atoms loaded in the trap. Then to optimize the loading, the FORT beam waist which was about 100 μm during the loading, was compressed tightly to about 25 μm to increase the elastic collision rate and hence the efficiency of the evaporative cooling. This was done by using the beam expander geometry discussed in Section 4.1.2.

The next step was to implement a two-stage evaporative cooling (EVC) process. The first stage was an exponential ramp-down of the CO_2 laser power from 30 W to about 1 W with a time constant of 2 seconds. This was done by reducing the RF power driving the CO_2 AOM. The second stage involved the reduction of laser power in a series of short steps ($\sim$100 ms each) followed by a 100 ms time interval to allow re-thermalization. Eventually the power in the second stage was reduced to about 50 mW over $\sim$5 seconds, to produce a pure BEC of about 100,000 atoms in the $5^2S_{1/2}, F = 1$ state ready for applying the perturbation of the desired experiment and/or imaging the atoms.

4.2 Imaging Setup

In order to image the BEC, a destructive absorption method was used. After creating the BEC, turning off the dipole trap and applying the desired perturbations (quantum walks here), the re-pump light was turned on so that the atoms at the $5^2S_{1/2}, F = 1$ state were pumped to the $5^2S_{1/2}, F = 2$ state as described before. After about 10 ms of expansion (time of flight), the atoms were then exposed to a short pulse of light on resonance with the $5^2S_{1/2}, F = 2 \rightarrow 5^2P_{3/2}, F' = 3$ transition to complete the imaging process as illustrated in Figure 4.10.

Figure 4.11 shows a schematic for the imaging system. A small portion of light which was resonant with the $5^2S_{1/2}, F = 2 \rightarrow 5^2P_{3/2}, F' = 3$ transition exited from fiber-1 to form an imaging beam. It was then expanded to 1 cm diameter using a beam expander and passed through a quarter-wave plate to make it circularly polarized. An absorption imaging technique based on the resonant interaction of light with atoms was implemented. When the BEC (or the diffracted atoms) were exposed to a weak ($\sim$100 nW) and short pulse (50-60 μs) of resonant light they scattered photons and cast a shadow which was imaged onto a high resolution CCD camera (ANDOR DV437-BV). The operating temperature and camera shutter time were controlled electronically using the LabView program. Two inexpensive security CCD cameras were also used to monitor the MOT in real time. The number of atoms was

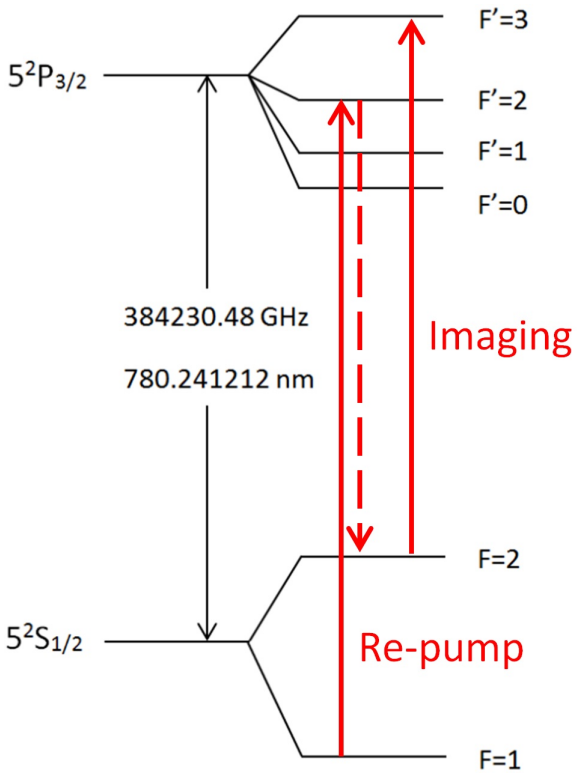

Figure 4.10: Optical transitions required for the imaging of the atoms. After being released from the dipole trap, the BEC atoms were applied the desired quantum walk perturbations and then given $\sim$10 ms time of flight to expand. Then a re-pump pulse was applied so that the atoms at the $5^2S_{1/2}, F = 1$ state were pumped to the $5^2S_{1/2}, F = 2$ state. The atoms were then imaged using a short pulse of light on resonance with the $5^2S_{1/2}, F = 2 \rightarrow 5^2P_{3/2}, F' = 3$ transition.

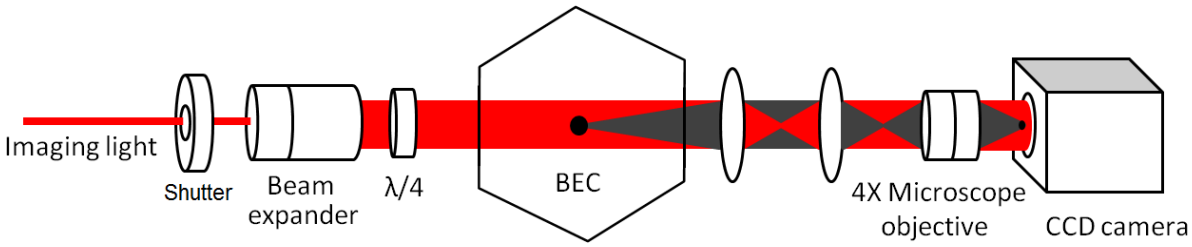

Figure 4.11: Schematic drawing of the imaging setup.

calculated from the image as follows: The loss in intensity I of a laser beam traveling in the z-direction which passes through a sample of atoms will be given by [72]

$$\frac{\mathrm{d}I}{\mathrm{d}z} = -\sigma n I. \tag{4.2}$$

Here n is the density of atoms, and $\sigma = \hbar\omega\gamma/2I_s$ is the scattering cross-section with ω the laser frequency, γ the natural linewidth and I_s the saturation intensity (see discussion around Eq. (2.30)). The solution of Eq. (4.2) is:

$$I(x,y) = I_0(x,y)\, e^{-\sigma\tilde{n}}, \tag{4.3}$$

where $\tilde{n}$ is the column density (number of atoms per unit area). The intensity $I(x,y)$ was found by taking two images. These images were taken with and without atoms giving intensities I_1 and I_0 respectively. The intensity profile $I(x,y)$ is then given by

$$I(x,y) = \frac{I_0}{I_1}. \tag{4.4}$$

The number of atoms can be calculated by integrating over the column density

$$N = -\frac{S}{\sigma}\sum_{\text{pixels}} \ln(I), \tag{4.5}$$

where $S = (13\ \mu\mathrm{m})^2$ is the scaled area of a pixel for the CCD camera and the sum is taken over all pixels.

4.3 Kicking Setup

The kicking laser was also a grating stabilized TOPTICA, DL100 laser in a temperature controlled housing. The frequency of this laser was stabilized at the transition from halfway between the $5^2S_{1/2}, F = 1$ and $F = 2$ hyperfine levels of the ground state to the $5^2P_{3/2}, F' = 3$ excited state as shown in Figure 4.12. The reason for using this laser frequency (that was dutuned by $\pm$3.4 GHz from either level of the ground state) was to address the atoms at both levels with the same kicking strengths (see Eq. (3.32) and discussion around Eq. (3.49)).

The alignment of the main kicking laser to perform the frequency stabilization and injection into its slave laser was similar to that of the master laser. As can be seen in Figure 4.13, a small portion of the main kicking laser was used to obtain the saturated absorption spectrum of ^{87}Rb for frequency locking, and the rest was used to injection-lock the frequency of a homemade slave laser to amplify the power. Then the amplified kicking beam of the slave laser was divided into two using a 50-50 beam splitter cube. Each beam had $\sim$13 mW power and was separately passed through ISOMET, 40N AOMs. The first order beam diffracted by each AOM was directed into the vacuum chamber through two viewports shared with a pair of MOT beams. Each kicking beam made 53° with the vertical forming a horizontal standing wave of wavelength $\lambda_G = \lambda/(2\sin 53^\circ)$, where λ=780 nm.

Each AOM was driven by an RF electrical signal which was supplied by a programmable arbitrary waveform generator (HP, HP8770A) and then passed through a 1-W amplifier. One of the AOMs was driven by the waveform generator at a fixed 30 MHz frequency while the other was driven at a variable frequency by another HP8770A waveform generator which was phase-locked to the first one. Each of these waveform generators was programmed using a GPIB interface card allowing for control of all RF waveform properties directly from the LabView program.

Standing wave pulses were engineered by controlling the phase, intensity, pulse length, and the relative frequency between the two laser beams. This was realized by running the standing wave's constituent laser beams through AOMs, each driven by an arbitrary waveform generator. The nodes of the standing wave were displaced with velocity $v = 2\pi\Delta f/G$ with Δf being the frequency difference between the two beams. Since the quasimomentum β of the BEC relative to the standing wave is proportional to v, changing Δf enabled the value of β to be systematically controlled. The duration of the kicking pulses was adjusted as short as 384 ns to ensure that the experiments were performed in the

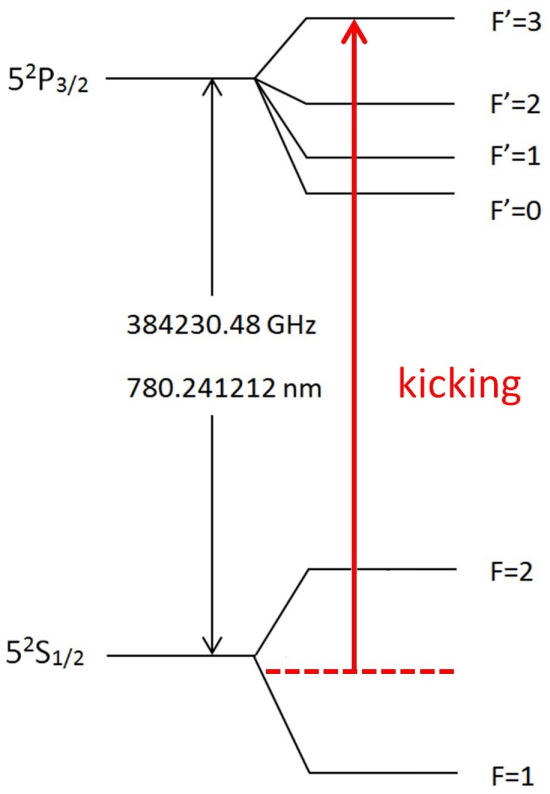

Figure 4.12: Kicking laser was frequency-stabilized to the transition from halfway between the $5^2S_{1/2}, F = 1$ and $F = 2$ hyperfine levels of the ground state to the $5^2P_{3/2}, F' = 3$ excited state. Thus the atoms at either internal state were kicked with the same $|k|$.

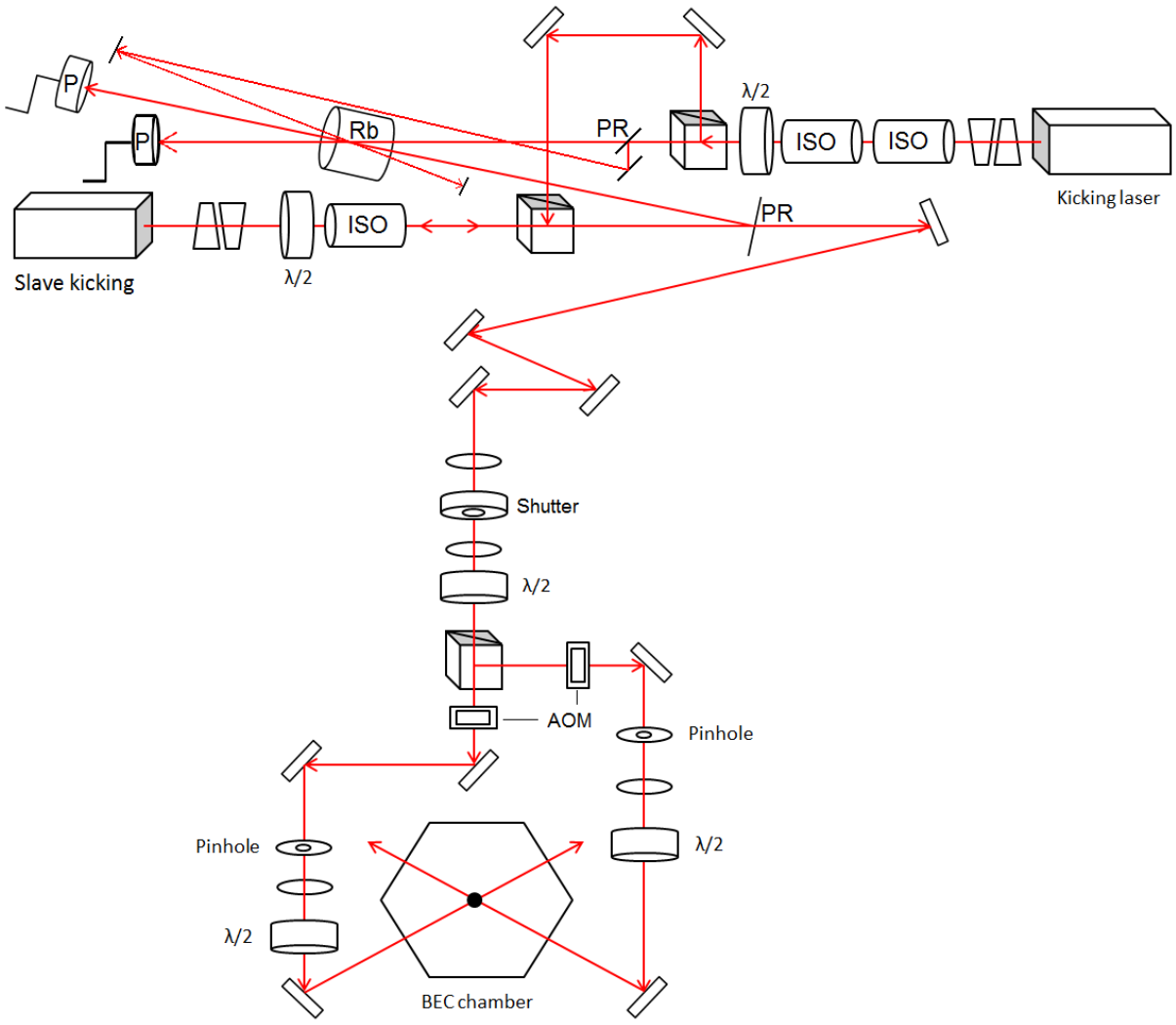

Figure 4.13: Optical setup for the kicking standing wave.

Raman-Nath regime [90]. That is, the distance the atoms traveled during the pulse was much smaller than the spatial period of the potential.

4.4 Microwave Setup

A schematic of the configuration used for MW pulse generation is shown in Figure 4.14. The MW pulses were generated by mixing two signals; a continuous MW signal with a constant frequency (6.8 GHz) and a pulsed RF signal with a tunable frequency ($\sim$34.682610 MHz). A rubidium atomic clock generating a 10 MHz reference was used to supply both the locking signal for a 6.80-GHz crystal oscillator (Microwave Dynamics; PLO-4000) and the external clock for the programmable waveform generator (HP, HP8770A). The latter synthesized the RF pulses with the desired length, phase, and frequency. It was also programmatically synchronized with the two other kicking waveform generators to ensure that the phase and timing of the MW and kicking pulses were as desired for the quantum walk experiments.

The final MW signal was the result of combining the crystal and waveform generator outputs in a frequency mixer (Marki Microwave) giving pulses of $\sim$6.834682610 GHz radiation. This frequency, which corresponds to the $5^2S_{1/2}, F = 1,\ m_F = 0 \leftrightarrow 5^2S_{1/2}, F = 2,\ m_F = 0$ transition in ^{87}Rb atoms (Figure 4.15), was also verified using an Agilent, E4407B spectrum analyzer. After being amplified to $\sim$30 dBm by a Terrasat Communications, ED-0278-4 amplifier, the output of the mixer was sent to a C-band horn antenna positioned close to the viewport of the vacuum chamber of the BEC. The desired intensity of the MW radiation was achieved by adjusting the amplification on the amplifier using a 0-5 V analog voltage controlled on a LabView program.

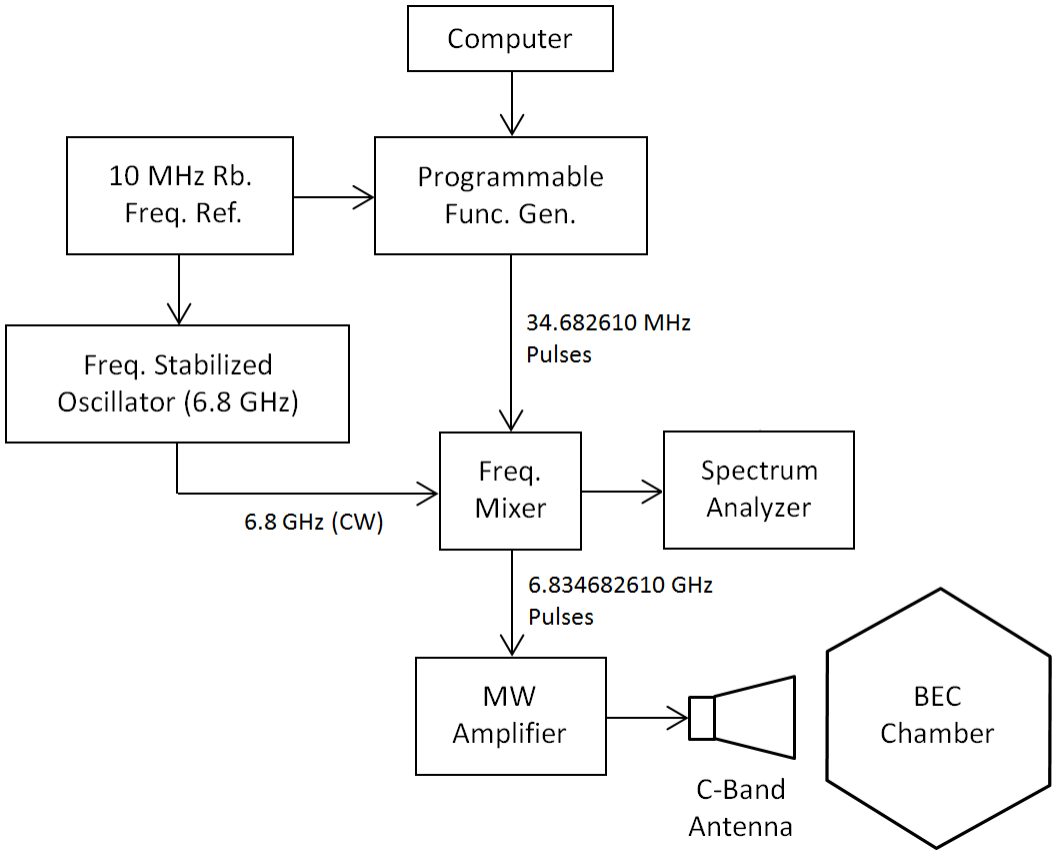

Figure 4.14: Schematic of the configuration used for generating the required MW pulses

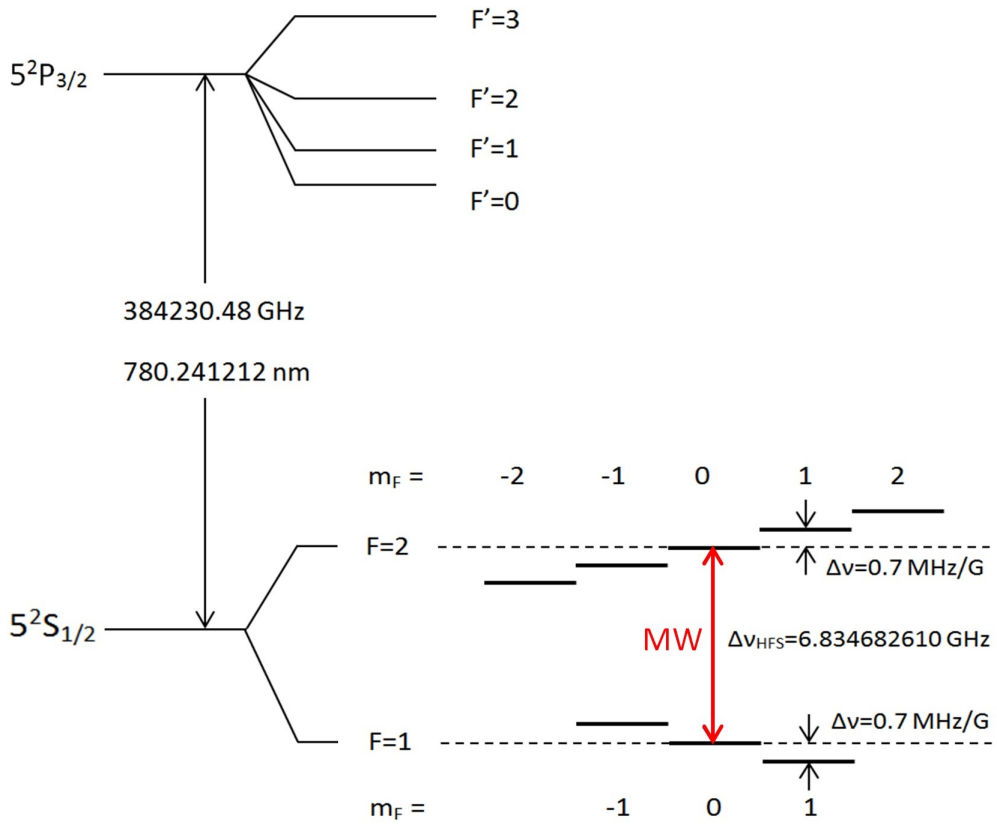

Figure 4.15: Atomic transition between the ^{87}Rb hyperfine levels of the ground state, $5^2S_{1/2}, F = 1,\ m_F = 0$ and $F = 2,\ m_F = 0$. This transition was addressed by means of the MW pulses tuned to the frequency of this transition.

Chapter 5

Results and Discussion

5.1 Standard Quantum Walk

This section elaborates the realization of standard quantum walks using the procedure described in Section 3.4.1. These walks were implemented by preparing superpositions of external and internal states using Bragg (Eq. (3.47)) and Hadamard (Eq. (3.50)) pulses, followed by successive coin toss and ratchet pulses working as the walk steps. In all experiments, we used unbiased coins, such that the MW pulses produced equal superpositions of internal states, and unbiased ratchets, such that the kicking light was detuned exactly halfway between the internal states and addressed them with equal strengths, $|k|$. Overall, the experimental results show the features expected of an ideal quantum walk, with a momentum distribution which diverges ballistically such that the spacing between its maxima is linearly proportional to the number of steps. In the following we discuss how different features of the experiment, such as the ratchet strength, coin choice, global phase compensation, external states preparation, BEC quasimomentum and thermal cloud, and spontaneous emission can influence the walk.

5.1.1 Ratchet Strength

We investigated the effects of the ratchet strength on the walk momentum distribution and its corresponding mean energy variation. The ratchet strength was essentially the strength of the AOKR, k, adjusted by tuning the intensity of the optical standing waves (see Eq. (3.32)). Three values of the ratchet strength were examined; $|k| = 1.2$, 1.45, and 1.8. Figure 5.1 shows experimental (1^{st} and 3^{rd} rows) and simulated (2^{nd} and 4^{th} rows) results for the momentum distribution of the quantum walks

realized with these kicking strengths. As can be seen, the characteristic standard deviation of the walk (spacing between the maxima) for all three cases grows linearly with time (number of steps). However, the case $|k| = 1.45$ best matched the standard quantum walk (with $q = 1$ in Eq. (3.55)) by coupling neighboring momentum states. The $|k| = 1.2$ walk was associated with less fluctuations in the momentum distribution and thus the energy, but with a slower growth of this parameter as shown in Figure 5.2. On the other hand, the $|k| = 1.8$ case showed a faster splitting of the walk peaks and hence a faster growth of momentum and energy. However there are hints that in the this case the walk has begun to suffer from decoherence and dephasing induced by the more intense light (note the saturation of the energy for this case in Figure 5.2). Thus, we employed the strength $|k| = 1.45$ for investigating different aspects of our quantum walks in the subsequent experiments.

5.1.2 Coin Choice

In this section we illustrate how the choice of the coins for initialization (gate) and mixing between subsequent steps can affect the symmetry of the walk. Although the coins affect the internal states only, the coin choice can eventually change the walk pattern, because the direction of the shifts in external states at each step is determined by the internal state of the walker. As mentioned earlier in Section 3.4, the symmetric walk is only obtained with the choice of gate and coin operators with phase differences of odd multiples of $\pi/2$, e.g. $\hat{\mathbf{M}}(\pi/2, \pi)$ and $\hat{\mathbf{M}}(\pi/2, -\pi/2)$ that we use as Hadamard gate and coin toss operators (see Eqs. (3.26) and (3.27) for the matrix representations). For the sake of simplicity, we only consider the initial external state $|n = 0\rangle$ and assume the ratchet can still be achieved without a broken spatial symmetry, i.e. without a Bragg pulse been applied. Thus, for a BEC originally at $|1\rangle$ internal state, the initial state of the system can be represented as

$$|\Psi_0\rangle = |n = 0\rangle \otimes |1\rangle = \begin{pmatrix} |n = 0\rangle \\ 0 \end{pmatrix}, \tag{5.1}$$

where either vector element represents one internal state (here only the $|1\rangle$ internal state is occupied with atoms at $|n = 0\rangle$ external state). We now consider two choices of coin operators; coin tosses different from the gate, i.e. $\hat{\mathbf{M}}(\pi/2, -\pi/2)$, and coins similar to the gate, i.e. $\hat{\mathbf{M}}(\pi/2, \pi)$ (Hadamard coins). It is not hard to show that applying the gate operator in the first step and either of these coin choices in the

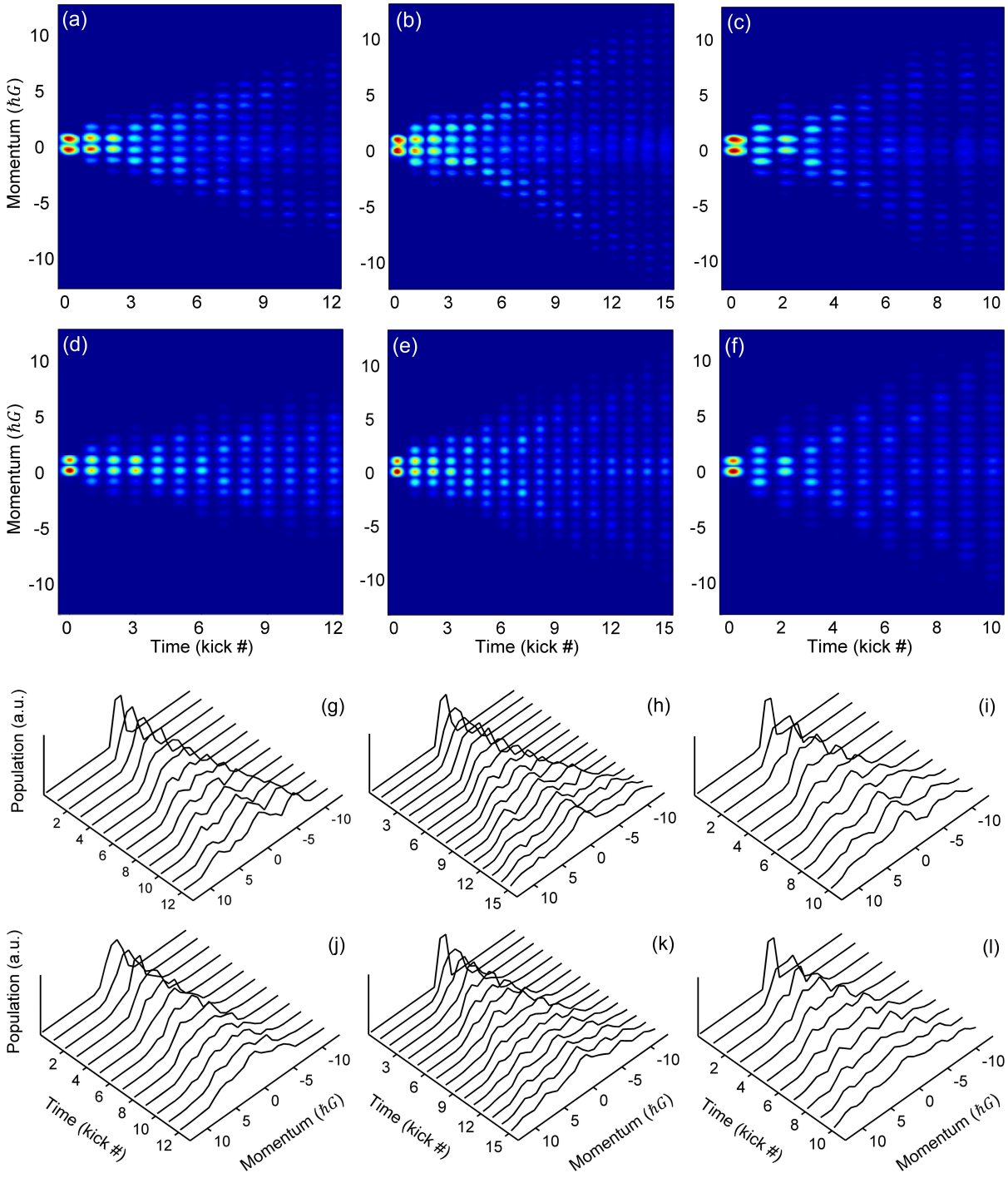

Figure 5.1: Experimental (1^{st} and 3^{rd} rows) and simulated (2^{nd} and 4^{th} rows) momentum distributions of the standard quantum walks with kicking strengths $|k| = 1.2$ (1^{st} column), 1.45 (2^{nd} column), and 1.8 (3^{rd} column). Each time (kick $\#$) represents one step of the walk, i.e one realization of the experiment (or simulation).

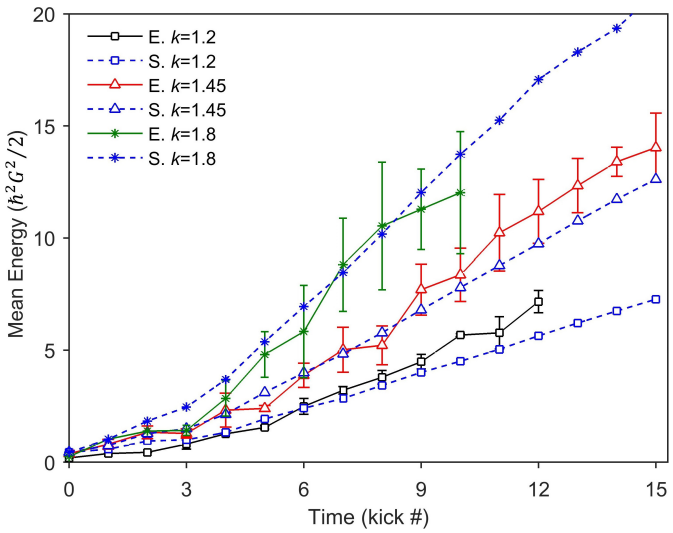

Figure 5.2: Experimental (E.) and simulated (S.) mean energy growth of the walk vs. kicking strength. The $|k| = 1.8$ walk has only been performed up to 10 steps because it spreads wider than the momentum detection window of the imaging system.

subsequent steps (along with the shift operators shown in Eq. (3.56)) yields the wave functions for the first three steps as:

for different coins:

$$\begin{aligned}
\text{step 1 (gate)}: \quad & |\Psi_1\rangle = \hat{\mathbf{T}}\hat{\mathbf{M}}(\pi/2,\pi)|\Psi_0\rangle = \frac{1}{\sqrt{2}}\begin{pmatrix} |n=1\rangle \\ |n=-1\rangle \end{pmatrix}, \\
\text{step 2}: \quad & |\Psi_2\rangle = \hat{\mathbf{T}}\hat{\mathbf{M}}(\pi/2,-\pi/2)|\Psi_1\rangle = \frac{1}{2}\begin{pmatrix} i|n=0\rangle + |n=2\rangle \\ |n=-2\rangle + i|n=0\rangle \end{pmatrix}, \\
\text{step 3}: \quad & |\Psi_3\rangle = \hat{\mathbf{T}}\hat{\mathbf{M}}(\pi/2,-\pi/2)|\Psi_2\rangle = \frac{1}{2\sqrt{2}}\begin{pmatrix} i|n=-1\rangle + (i-1)|n=1\rangle + |n=3\rangle \\ |n=-3\rangle + (i-1)|n=-1\rangle + i|n=1\rangle \end{pmatrix},
\end{aligned} \tag{5.2}$$

j/n	-4	-3	-2	-1	0	1	2	3	4
Different coins									
0					1				
1				$\frac{1}{2}$	0	$\frac{1}{2}$			
2			$\frac{1}{4}$	0	$\frac{1}{2}$	0	$\frac{1}{4}$		
3		$\frac{1}{8}$	0	$\frac{3}{8}$	0	$\frac{3}{8}$	0	$\frac{1}{8}$	
4	$\frac{1}{16}$	0	$\frac{6}{16}$	0	$\frac{2}{16}$	0	$\frac{6}{16}$	0	$\frac{1}{16}$
Similar coins									
0					1				
1				$\frac{1}{2}$	0	$\frac{1}{2}$			
2			$\frac{1}{4}$	0	$\frac{1}{2}$	0	$\frac{1}{4}$		
3		$\frac{1}{8}$	0	$\frac{1}{8}$	0	$\frac{5}{8}$	0	$\frac{1}{8}$	
4	$\frac{1}{16}$	0	$\frac{1}{8}$	0	$\frac{1}{8}$	0	$\frac{5}{8}$	0	$\frac{1}{16}$

Table 5.1: The probability distributions of the first three steps of the quantum walks when using the coin operators that are different from or similar to the gate operator. The walk starts to be asymmetric at the third step when the latter case is implemented.

and for similar coins:

$$\text{step 1 (gate)}: \quad |\Psi_1\rangle = \hat{\mathbf{T}}\hat{\mathbf{M}}(\pi/2,-\pi/2)|\Psi_0\rangle = \frac{1}{\sqrt{2}}\begin{pmatrix} |n=1\rangle \\ i|n=-1\rangle \end{pmatrix},$$

$$\text{step 2}: \quad |\Psi_2\rangle = \hat{\mathbf{T}}\hat{\mathbf{M}}(\pi/2,-\pi/2)|\Psi_1\rangle = \frac{1}{2}\begin{pmatrix} -|n=0\rangle + |n=2\rangle \\ i|n=-2\rangle + i|n=0\rangle \end{pmatrix},$$

$$\text{step 3}: \quad |\Psi_3\rangle = \hat{\mathbf{T}}\hat{\mathbf{M}}(\pi/2,-\pi/2)|\Psi_2\rangle = \frac{1}{2\sqrt{2}}\begin{pmatrix} -|n=-1\rangle - 2|n=1\rangle + |n=3\rangle \\ i|n=-3\rangle + i|n=1\rangle \end{pmatrix}. \quad (5.3)$$

Table 5.1 shows the population of different external states (momentum orders) corresponding to the wave functions derived for these first three steps. As can be seen, while using different gate and coin pulses, results in a symmetric distribution of external states, applying similar gate and coin pulses starts producing an asymmetric distribution with a nonzero mean momentum. This is due to the fact that, in the case of differently chosen coins, the $|1\rangle$ and $|2\rangle$ states carry both real and imaginary amplitudes, and thus when affected by the real and imaginary elements of the coin operator, no interference takes place in neither direction. This gives a walk with a symmetric probability distribution of the external states.

On the other hand, if the similar coins are chosen, the $|1\rangle$ and $|2\rangle$ trajectories stay either pure real or pure imaginary, and thus when affected by the coin operator, constructive and destructive interference take place at some external states. This results in an asymmetry propagating through the constructive steps of the walk as shown in Figure 5.3 where $\hat{\mathbf{M}}(\pi/2, -\pi/2)$ pulses have been used for both gate and coin tosses.

5.1.3 Global Phase Effect

As mentioned in Section 3.4.1, the $e^{\pm ik}$ prefactors in the kicking terms of the shift operator (Eq. (3.52)) introduce a phase difference of $\Delta\phi = 2k$ between the $|1\rangle$ and $|2\rangle$ states. This is due to the DC component of the intensity of the optical standing wave (Eq. (3.33)) that we use for kicking the atoms in the ratchet process. If this phase difference is not compensated properly at each walk step, it will result in a phase distortion and adversely affect the symmetry of the walk as shown in Figure 5.4. The experimental conditions applied to implement the walk in this figure are similar to those of Figure 5.1.b except that in this case the $\Delta\phi$ has not been compensated at each step. As can clearly be seen, the momentum distribution of the walk without the phase compensation is quite distorted and the pair of diverging momentum currents, which are the signatures of a standard walk are smeared out. To verify the value ($2k$) of the phase to be compensated, the walk was implemented for step numbers 2 and 5 by scanning the compensating phase applied on the coin toss MW pulses at each step. Results are shown in Figures 5.5.a,b for these two cases as the momentum distribution versus the applied phase and in Figure 5.5.c as the variation of their corresponding mean momenta. The gradual transfer of the weight of the walk from one side to other by varying the phase is quite clear in these figures. As one would expect, the symmetry was achieved only when $2k$ or $2k+\pi$ (rad) phases were applied on the MW pulses to properly cancel the $\Delta\phi$ effect. Thus an additional phase of $2k$ was added to all MW pulses in the the experiments to maintain the symmetry of the walk at each step.

5.1.4 Initial State Effect

As can be seen in the time of flight images of the walks in Figure 5.1, almost all momentum classes between the diverging currents are populated. This shows that, regardless of the applied ratchet strengths, the walks undergo a diffusion that limits the quality of the walk. Since our walk steps work based on the

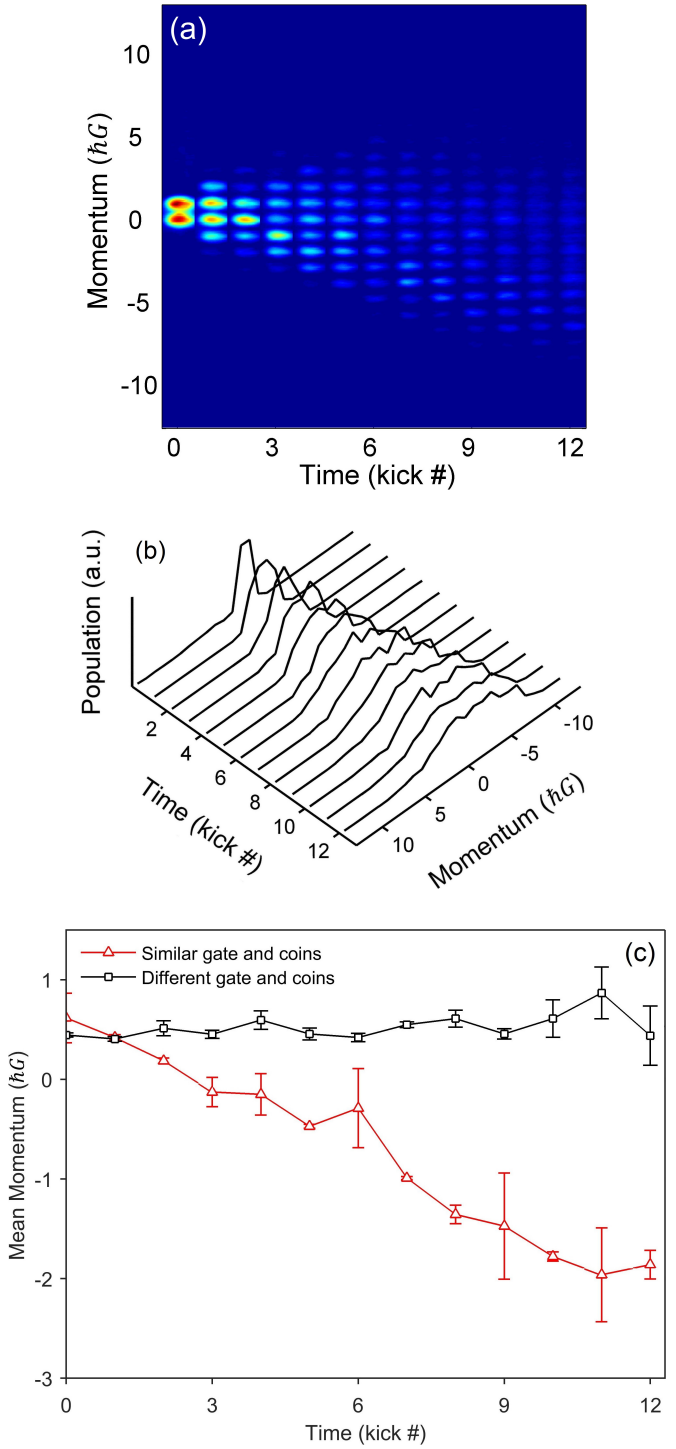

Figure 5.3: Momentum distribution of an asymmetric walk implemented by using $\hat{\mathbf{M}}(\pi/2, -\pi/2)$ pulses as both gate and coin toss operators (a,b). Panel (c) compares the mean momentum variation of this walk with that of a symmetric one achieved by using the coin pulses different from the gate.

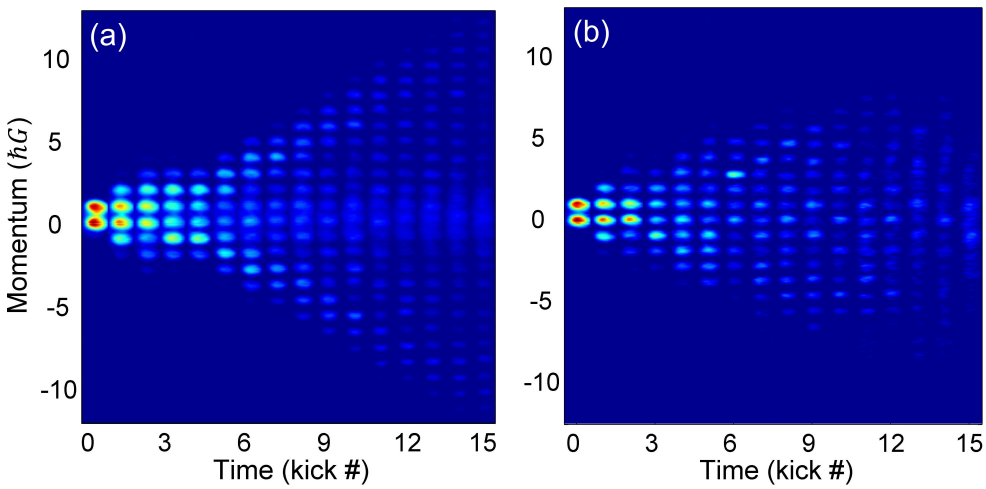

Figure 5.4: Quantum walks implemented with (a) and without (b) compensating the global phase introduced by the DC component of the optical standing wave at each step ($|k| = 1.45$). Smearing out of the momentum currents as a result of this dephasing is quite clear in panel (b).

quantum ratchets, we should be able to address this issue using the same idea described for the ratchets in Section 3.3.2; by increasing the number of components contributing to the initial momentum state, one can achieve narrower spatial wave functions that result in "cleaner" ratchet currents [50]. Therefore, while not done here, in principle, walks with less diffusion between the diverging momentum currents, can be achieved through the choice of an initial state composed of more momentum states [52].

5.1.5 Thermal Cloud Effect

Throughout our experimental walk images, there appears to be an "amorphous" population signal about the center of the momentum distribution (see for example Figure 5.1). This is the effect of the residual atomic thermal cloud that, unlike the BEC, does not respond to the optical pulses and therefore remains unaffected throughout the walk. This is due to the fact that the cloud includes a wide range of quasimomenta which is mostly off-resonant (contrary to the narrow range of the BEC quasimomenta) and thus it does not respond to the kicking scheme. Recall that the quantum resonance conditions are met only for quasimomenta very close to zero (see discussion around Eq. (3.44)). We checked this aspect of the thermal cloud by applying a strong Bragg pulse on a BEC with different contributions of the thermal cloud. As can be seen in Figure 5.6, the strong Bragg pulse can entirely move the BEC from $|n = 0\rangle$ state to the $|n = 1\rangle$ state, but the thermal cloud does not contribute to the Bragg diffraction and remains

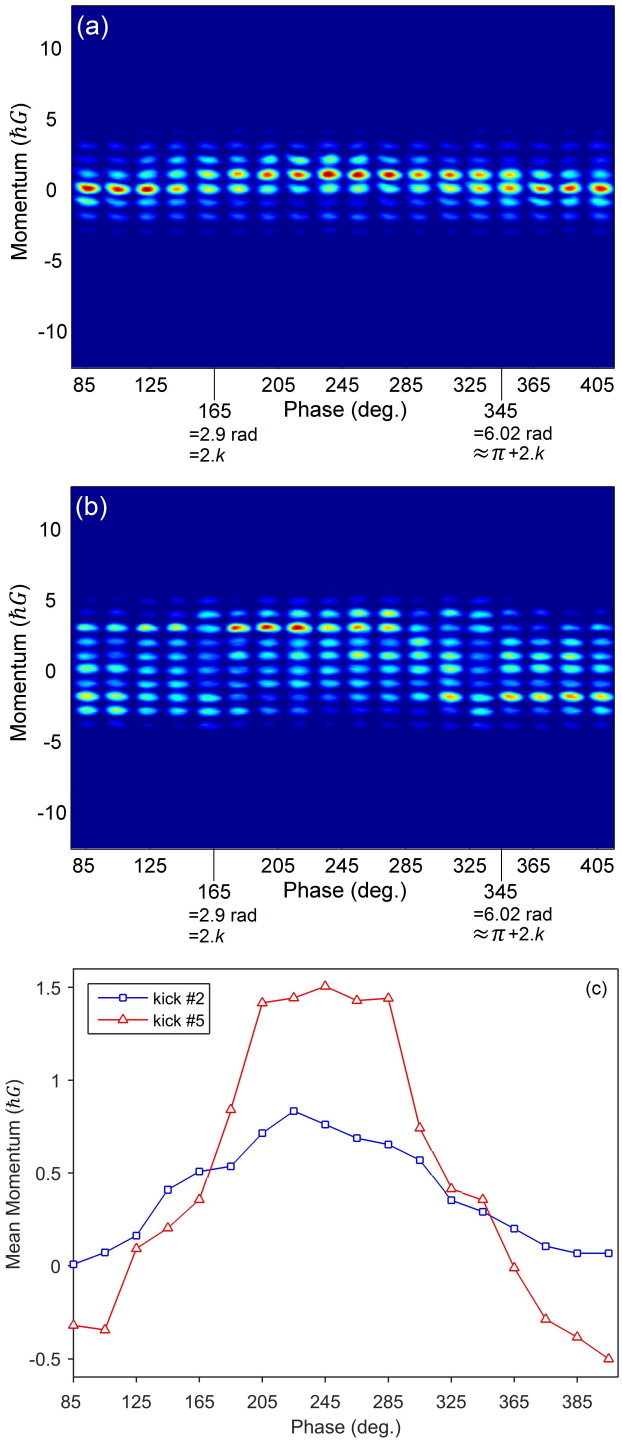

Figure 5.5: Scanning the phase of MW pulses to find the exact value of the global phase to be compensated at each step. Panels (a) and (b) show the 2^{nd} and 5^{th}-step momentum distributions versus the applied phase and panel (c) shows the variation of their corresponding mean momenta. The gradual transfer of the weight of the walk from one side to other by varying the phase is quite clear in these figures. As expected, the symmetry (mean momentum≈0.5) was achieved only at $2k$ or $2k + \pi$ (rad) phases.

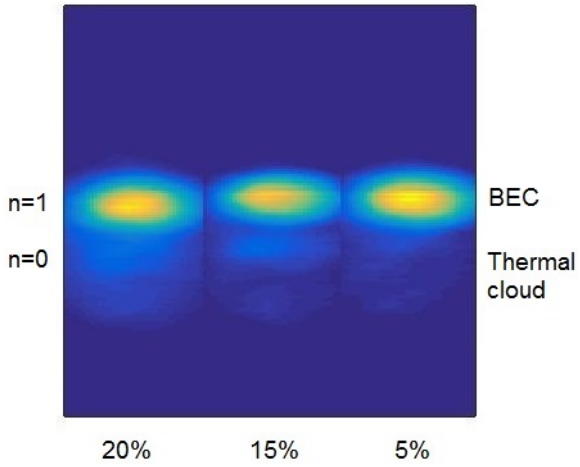

Figure 5.6: A strong Bragg pulse applied on a BEC with different contributions of the thermal cloud. This pulse can entirely move the BEC from $|n = 0\rangle$ state to the $|n = 1\rangle$ state, but the thermal cloud does not contribute to the Bragg diffraction and remains unaffected.

untouched.

The thermal cloud present in the experiments was taken into account in our simulations as well. It was modeled by a Gaussian distribution with a width of half the Brillouin zone for the initial quasimomenta [97]. We estimated its ratio compared to the number of atoms in the BEC to be $10 - 15\%$ by comparing the experimental data with our simulations. Note that the lower cloud contribution in our experiments was achievable only with a significantly lower BEC population which itself caused a poor signal-to-noise ratio of the walk images. This trade off limited our ability to reduce the cloud contribution further. The results as compared to the ideal case without the thermal cloud are shown in the Figure 5.7.

5.1.6 Quasimomentum Effect

Another aspect of the experiment that limits the implementation of our quantum walks for high number of steps is the near-resonant quasimomentum of the BEC. This is due to the fact that the BEC created in the experiment is not an ideal delta function in momentum space and in fact a broadening, so called the near-resonant quasimomentum, is always associated with the BEC distribution. This momentum distribution follows the resonant AOKR only for a few steps until the dephasing induced by the imperfect resonance becomes strong enough to freeze the quasimomentum into a broad Gaussian which is no longer affected by the kicking process.

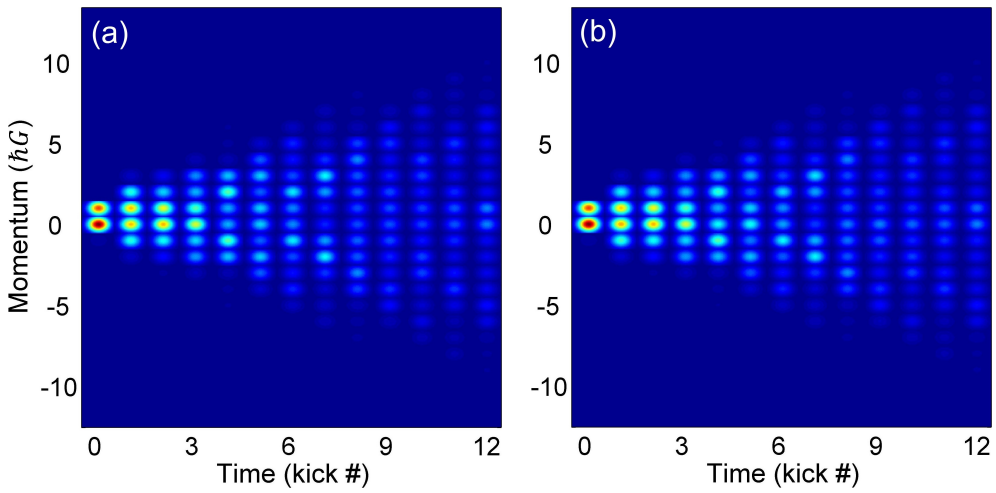

Figure 5.7: Simulated images for the effects of the thermal cloud on the momentum distributions of a standard quantum walk ($|k| = 1.45$ and $\delta\beta_{\mathrm{FWHM}} = 0.025$). Panel (a) shows the walk of an ideal BEC with no thermal cloud, and panel (b) includes a 15% contribution of thermal in the center around zero momentum. Note the appearance of a weak signal about the center of the walk in the latter.

Figure 5.8 compares two standard walks implemented under similar experimental conditions except that the BECs with different quasimomenta, $\delta\beta_{\mathrm{FWHM}} = 0.025$ and $0.04\ \hbar G$ have been used. As can be seen, the walk initiated with a high quasimomentum BEC (Figure 5.8.b) undergoes a decoherence that prevents a large extent of the atomic population from being driven along the walk currents. These atoms remain quite unaffected in the states around the center and slow down the growth of mean energy as shown in Figure 5.8.c. This might encourage one to use a BEC with a minimum achievable quasimomenta to implement the quantum walk. However, this raises another difficulty. Since the walk itself is always associated with a gradual reduction of atomic population, using a BEC with minimum quasimomenta (thus with lower population) results in the lack of visibility on the detection system and adversely affects the signal-to-noise ratio of the images.

5.1.7 Spontaneous Emission Effect

The last investigated effect was the spontaneous emission which can decoherently destroy the walk spread until it approaches a Gaussian distribution and thus a classical walk at higher number of steps (see Section 5.4). A comprehensive theoretical treatment of the spontaneous emission is developed in [96]. We simulated the effects of spontaneous emission using a quantum jump method [99] and estimated its per-kick probability from the experimental parameters to be below 1% for each atom. For such low

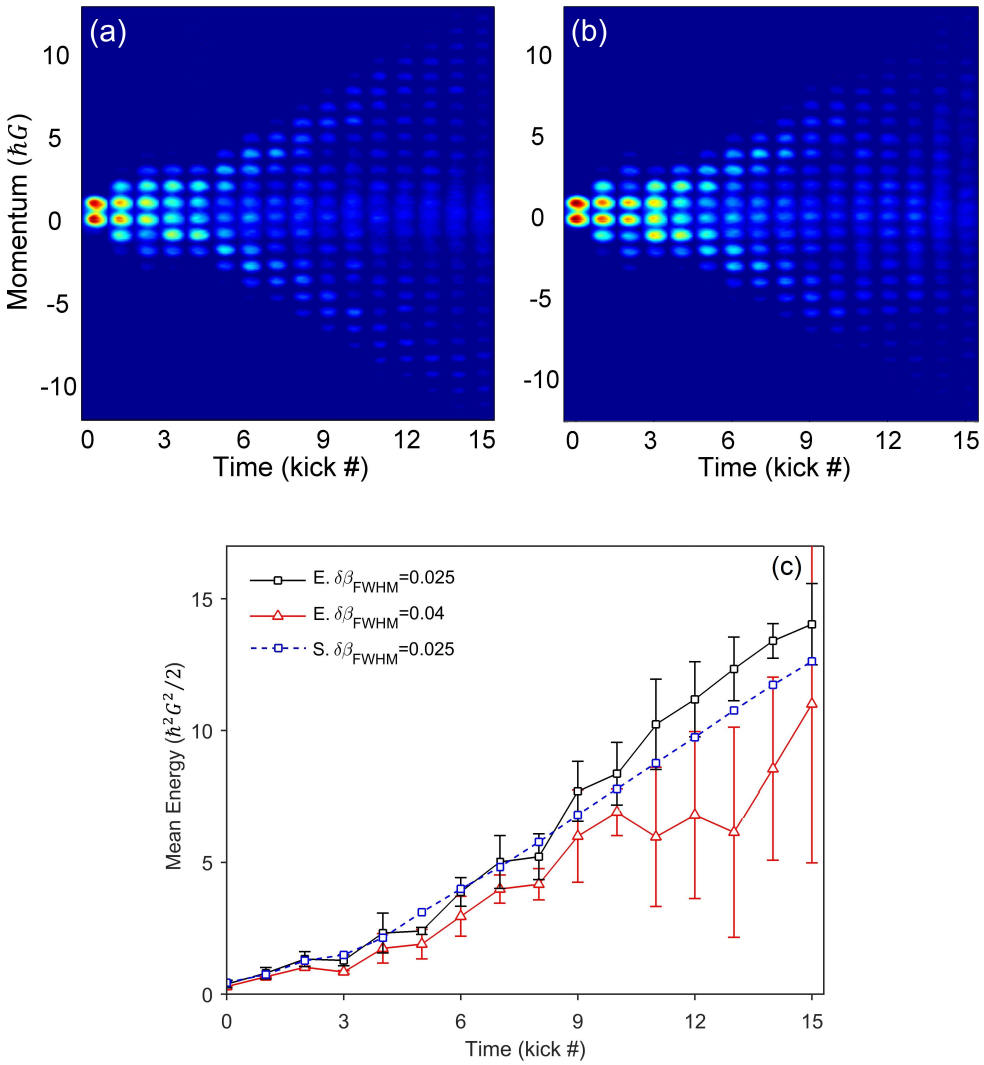

Figure 5.8: Comparison of two standard walks implemented using the BECs with different quasimomenta, $\delta\beta_{\mathrm{FWHM}} = 0.025\ \hbar G$ (a) and $0.04\ \hbar G$ (b). Kicking strength is $|k| = 1.45$ in both cases. Panel (c) shows the slower growth of the mean energy due to the accumulation of atoms around the center in case of using a BEC with a large quasimomentum, $\delta\beta_{\mathrm{FWHM}} = 0.04$.

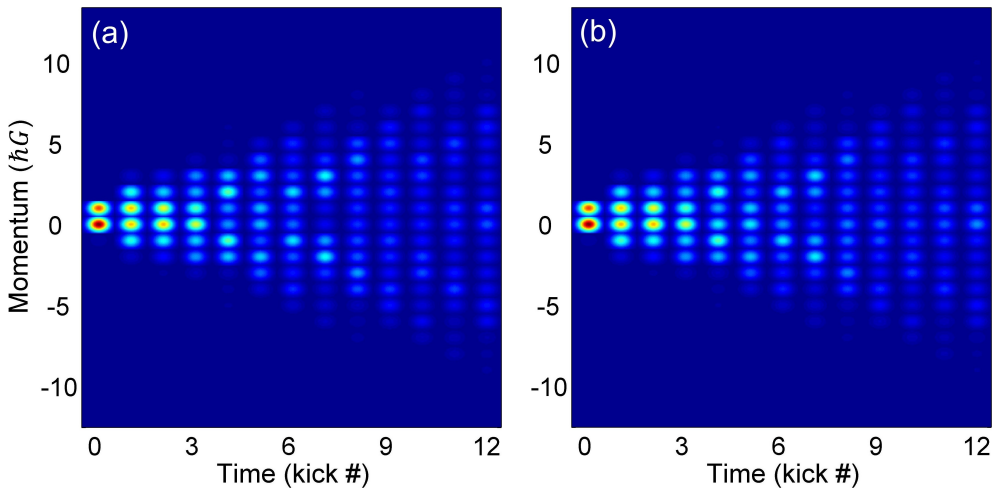

Figure 5.9: Comparison of the quantum walks simulated for the kick strength $|k|$=1.45 and $\delta\beta_{\mathrm{FWHM}} \approx 0.025\ \hbar G$, with (a) and without (b) including the spontaneous emission with approximately 0.5% of event probability per kick and per atom.

rates, spontaneous emission does not contribute to walks up to 20 steps, as can be inferred by comparing panels (a) and (b) in Figure 5.9. Since no visible change occurs we may safely neglect spontaneous emission at such expected low rates. Higher emission rates would, however, induce decoherence into the walk since they would lead to an early collapse of the wave function and consequently they would destroy the entanglement between both degrees of freedom [97].

5.2 Steered Quantum Walk

In previous section we described the walks that were symmetric around the initial momentum states $|n = 0\rangle$ and $|n = 1\rangle$ due to the choice of unbiased coins and ratchets. The former was achieved using the exact $\pi/2$ MW pulses to mix the states at each step, and the latter was achieved by stabilizing the frequency of the kicking laser exactly halfway between the $5^2S_{1/2}, F = 1$ and $5^2S_{1/2}, F = 2$ hyperfine levels, so that the absolute value of the kicking strength was equal for both internal states. Our experimental setup also permitted us to investigate biased quantum walks in momentum space. In this section we describe how we steered the walks in a preferred direction by biasing either coin or shift (ratchet) operators, i.e. by constantly manipulating either of internal or external degrees of freedom. The controllability of the walk direction is particularly interesting for actual implementations and use in quantum information applications.

5.2.1 Biased Coin

We realizes the biased coins (BC) by altering the power of the MW pulses from the $\pi/2$ scheme, so that unequal superpositions of internal states were obtained. This change affects the balance of the gate and coin operators in Eqs. (3.26) and (3.27) by introducing a bias factor ρ such that [97]

$$\text{Biased gate}: \qquad \hat{\mathbf{M}}_{\rho}(\pi) = \begin{pmatrix} \sqrt{\rho} & -\sqrt{1-\rho} \\ \sqrt{1-\rho} & \sqrt{\rho} \end{pmatrix}, \tag{5.4}$$

and,

$$\text{Biased coin}: \qquad \hat{\mathbf{M}}_{\rho}(-\pi/2) = \begin{pmatrix} \sqrt{\rho} & i\cdot\sqrt{1-\rho} \\ i\cdot\sqrt{1-\rho} & \sqrt{\rho} \end{pmatrix}. \tag{5.5}$$

This means that one internal state was constantly assigned a higher population than the other. Figure 5.10 demonstrates the experimental and simulated results of the steered walk in momentum space for a BC case at the kicking strength $|k| = 1.45$. Here the coin tosses were biased by $\rho = 0.7$ so as to produce the internal state $\sqrt{0.7}|1\rangle + \sqrt{0.3}|2\rangle$ rather than $\sqrt{0.5}(|1\rangle + |2\rangle)$. Figure 5.10.c presents a comparison of the mean momentum of this BC walk to an unbiased walk. As can be inferred, both the direction and speed of the walk can be manipulated by altering the value of ρ in the coins.

5.2.2 Biased Ratchet

We also implemented steered walks via the use of non-symmetric walk steps (i.e. the walk's left or right shifts were not identical). In this case, a biased ratchet (BR) was achieved by detuning the kicking laser so that the laser frequency was no longer halfway between the ground state hyperfine levels. Since the ratchet strength is inversely proportional to the detuning, this shift in the laser frequency results in unequal ratchet potentials addressing each state. This generalizes the one-step shift operator from Eq. (3.54) into [23]

$$\hat{\mathbf{T}} = \exp\left[-i\cos(\hat{\theta})\begin{pmatrix} k_1 & 0 \\ 0 & k_2 \end{pmatrix}\right], \tag{5.6}$$

where the bias is controlled by k_2/k_1. Figure 5.11, shows the experimental and simulated results of a BR steered walk realized with an unbiased kicking strengths $k_1 = -1.7$, $k_2 = +1.0$ instead of $k_1 = -1.45$, $k_2 = +1.45$. Figure 5.11.c compares the mean momentum of this walk to an unbiased

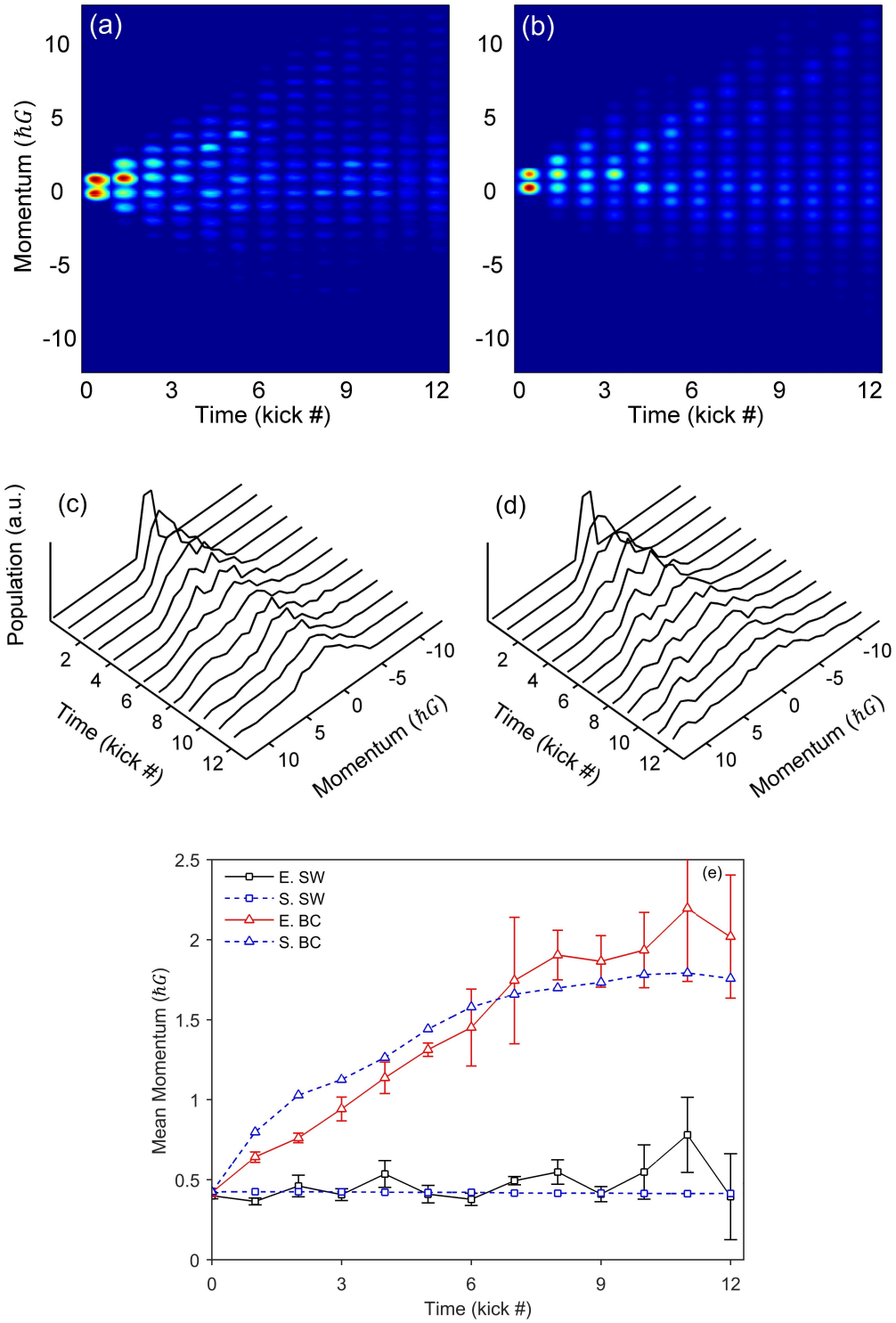

Figure 5.10: Steered quantum walk with biased coin (BC) tosses ($\rho = 0.7$) each giving a $\sqrt{0.7}|1\rangle + \sqrt{0.3}|2\rangle$ superposition of internal states (a,c experimental and b,d simulation, $|k| = 1.45$). Panel (e) shows the experimental (E.) and simulated (S.) variation of the mean momentum for the corresponding BC walk compared to the symmetric walk (SW).

walk with $|k| = 1.45$. Intuitively, the direction and speed of the walk can be controlled by the difference of kick strengths between the two internal states; i.e., the larger the difference, the faster the momentum current moves in the desired direction.

5.3 Quantum Walk Reversal

In previous section one of the controllability aspects of the walk was demonstrated by steering it into one of two possible directions. In this section we describe the reversibility as another control feature of our momentum-based quantum walks. More specifically, we were able to manipulate our walks with diverging momentum currents to refocus and retrieve the initial state of the system by reversing the steps taken. This control feature of our walk was a consequence of the unitary nature of the walk and the entanglement between the internal and external degrees of freedom (see Eq. (3.28)) which can be achieved only in quantum systems; since the classical walks are not unitary and entangled, reverting the walk is not possible.

After a certain number of walk steps $\hat{\mathbf{U}}_{\text{step}} = \hat{\mathbf{M}}\hat{\mathbf{T}}$ are taken (8 steps here), applying their Hermitian conjugate, $\hat{\mathbf{U}}^{\dagger}_{\text{step}} = \hat{\mathbf{T}}^{\dagger}\hat{\mathbf{M}}^{\dagger}$, for the same number of steps reverts the system to its origin [52]. Details of $\hat{\mathbf{U}}^{\dagger}_{\text{step}}$ and the walk reversal experimental procedure are described in Section 3.4.2. Figure 5.12 shows the experimental (a,c) and simulated (b,d) momentum distributions of our walk reversal. The mean energy of the system corresponding to this procedure is also shown in Figure 5.12.e. The downturn of the mean energy due to the refocusing of the momentum currents is quite clear in this figure. However, as can be seen, the energy does not completely return to its original value. This is due to the fact that the extent of the initial state recovery depends on the fractions of quasimomentum and thermal cloud, and since the BEC is always inevitably associated with these parameters, the full system recovery is impossible in reality. However, contrary to the standard walks, we were able to minimize the quasi-momentum and thermal cloud contributions (to 0.02 $\hbar G$ and 10% respectively) in this particular case to maximize the initial system recovery. This was because losing the signal-to-noise ratio due to the gradual atomic loss was less of a concern, since the refocusing of momentum currents enhanced the visibility and hence conserved the signal-to-noise ratio. One potential application of these "driven" walks [56, 57] is in quantum algorithms, e.g. searches of marked momentum states, as in [60] but by adjusting the coin degree of freedom.

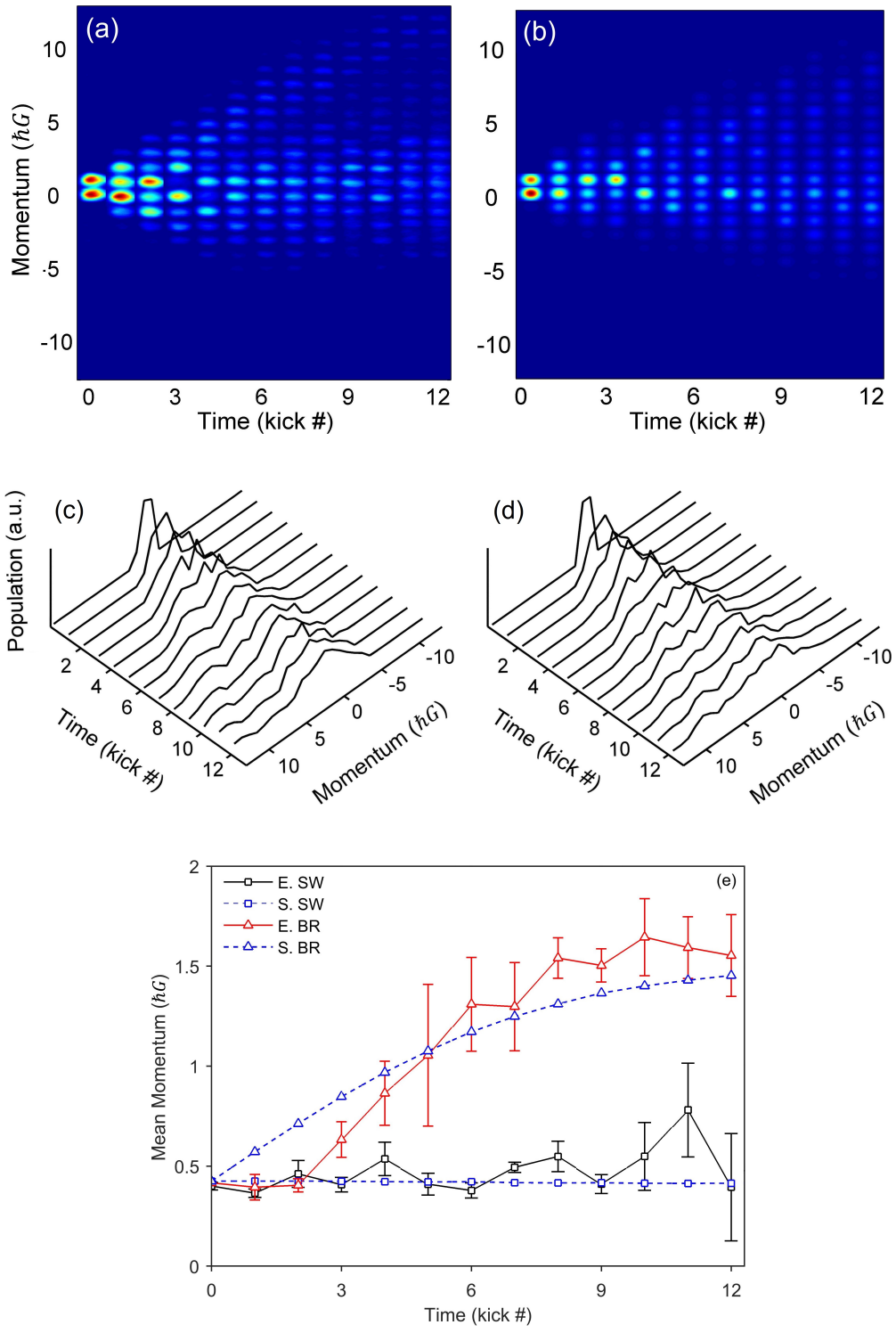

Figure 5.11: Steered quantum walks with biased ratchet (BR) strengths $k_1 = -1.7$ and $k_2 = +1.0$ (a,c experimental and b,d simulation). Panel (e) shows the experimental (E.) and simulated (S.) variation of the mean momentum for corresponding BR walk compared to the symmetric walk (SW).

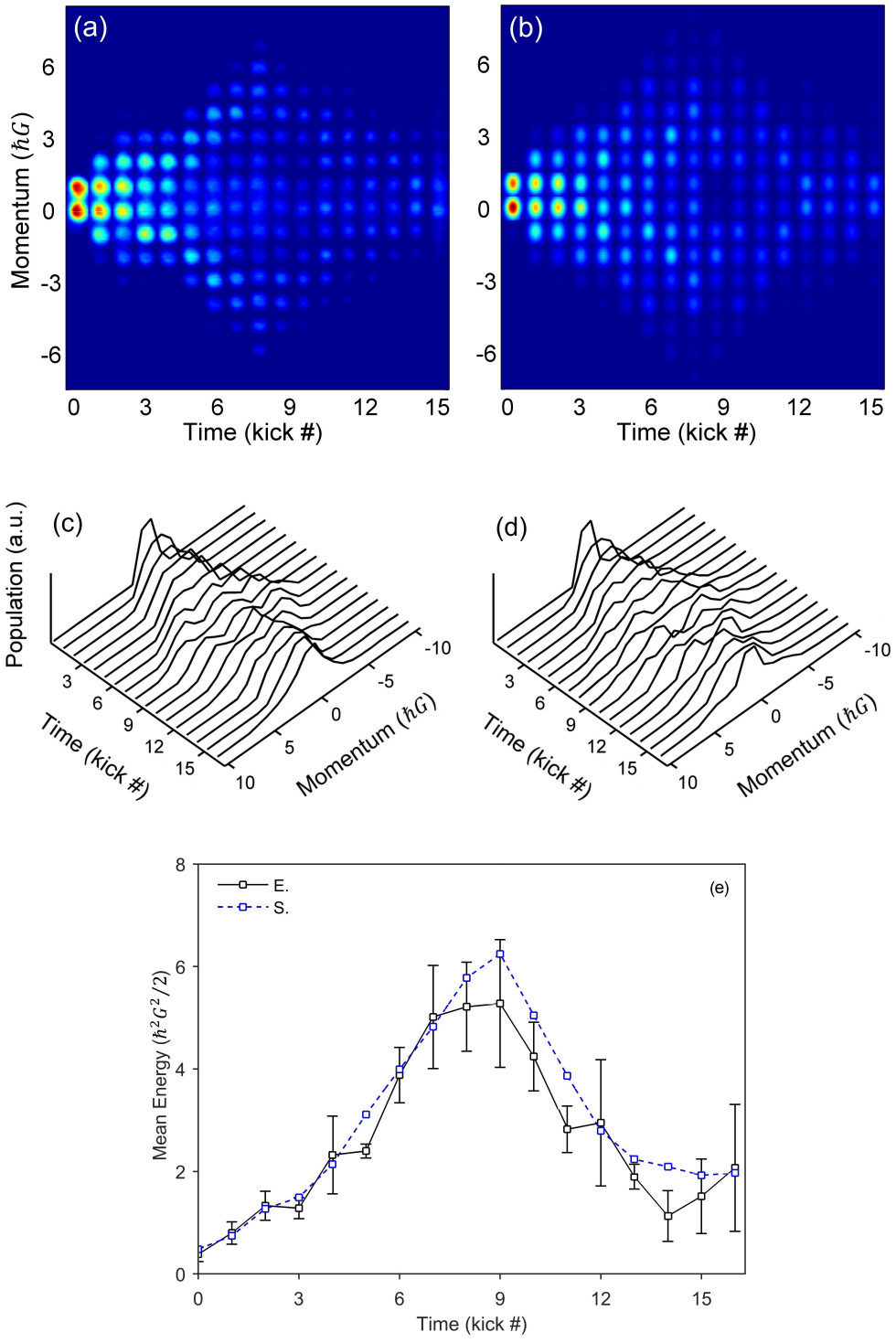

Figure 5.12: Experimental (a,c) and simulated (b,d) momentum distributions of a reversed quantum walk with $|k| = 1.45$. The extent of the initial state recovery depends on the fractions of quasimomentum and thermal cloud in the BEC. Panel (e) shows the experimental (E.) and simulated (S.) mean energy for a walk with quasimomentum and thermal cloud fractions of 2% and 10% respectively.

5.3.1 Ratchet Reversal

In addition to the quantum search algorithms, one would make use of the reversible quantum walks in atom interferometry [100]. The interference signal of the recombining momentum currents is a factor of their phase difference (not shown here) and can be used to precisely detect any quantum behavior [26, 27, 33, 58, 59]. Atomic interferometers can also be realized simply by using the momentum currents of a bi-directional ratchet as the arms of the interferometer (see discussion around Figure 3.10 for details if a bi-directional ratchet). In this type of interferometer, after separating the internal states with a gate pulse (a beam splitter), the momentum currents start diverging due to the ratchet kicks. Note that the internal states do not need to be mixed using MW coin pulses at each step, so that each momentum current will purely carry either of the internal states. Then, these internal states can be simply swapped out using a MW π pulse after a certain number of steps. This π pulse acts as the mirrors of an optical interferometer shifting the phase of the beams by π. Thereafter, the spatial distribution of each internal state will see the subsequent set of ratchet potentials shifted by π (see Figure 3.8) and thus will move in exactly opposite directions. A protocol of such a procedure would then be:

$$\hat{\mathbf{M}}(\pi/2,\chi)\ \hat{\mathbf{T}}^{j}\ \hat{\mathbf{M}}(\pi,\pi/2)\ \hat{\mathbf{T}}^{j}\ \hat{\mathbf{M}}(\pi/2,\pi) \tag{5.7}$$

with $\hat{\mathbf{M}}(\pi/2,\chi)$ being the recombiner $\pi/2$ MW pulse applied at the end of the ratchet reversal process. Clearly, the final population of either internal state will oscillate by scanning the phase of the recombiner pulse, χ, which was examined as the proof of principle (not shown here). This population will also alter as a result of the phase shifts on the internal states caused by any perturbations during the ratchets. As mentioned before, one can use this to detect or measure the quantum effects.

Figure 5.13 is a generic demonstration of the reversal of ratchets with 6 and 10 total number of steps. As in quantum walk reversals, the full recovery of the initial state heavily depends on the BEC quasimomentum which results in a dephasing with not perfectly fulfilling the quantum resonance ratchet scheme. This effect gets more prominent at higher number of steps as can be seen by comparing the final momentum distributions of Figures 5.13.a and 5.13.b. However, the ratchet reversal itself can be used to precisely measure the extent of the quasimomentum; Figure 5.14 shows the simulated populations of both internal states as a function of recombiner phase, χ, for different amounts of quasimomentum, $\delta\beta_{\mathrm{FWHM}}$ [97]. Thus by matching the visibility of the oscillations in experimental data with simulated

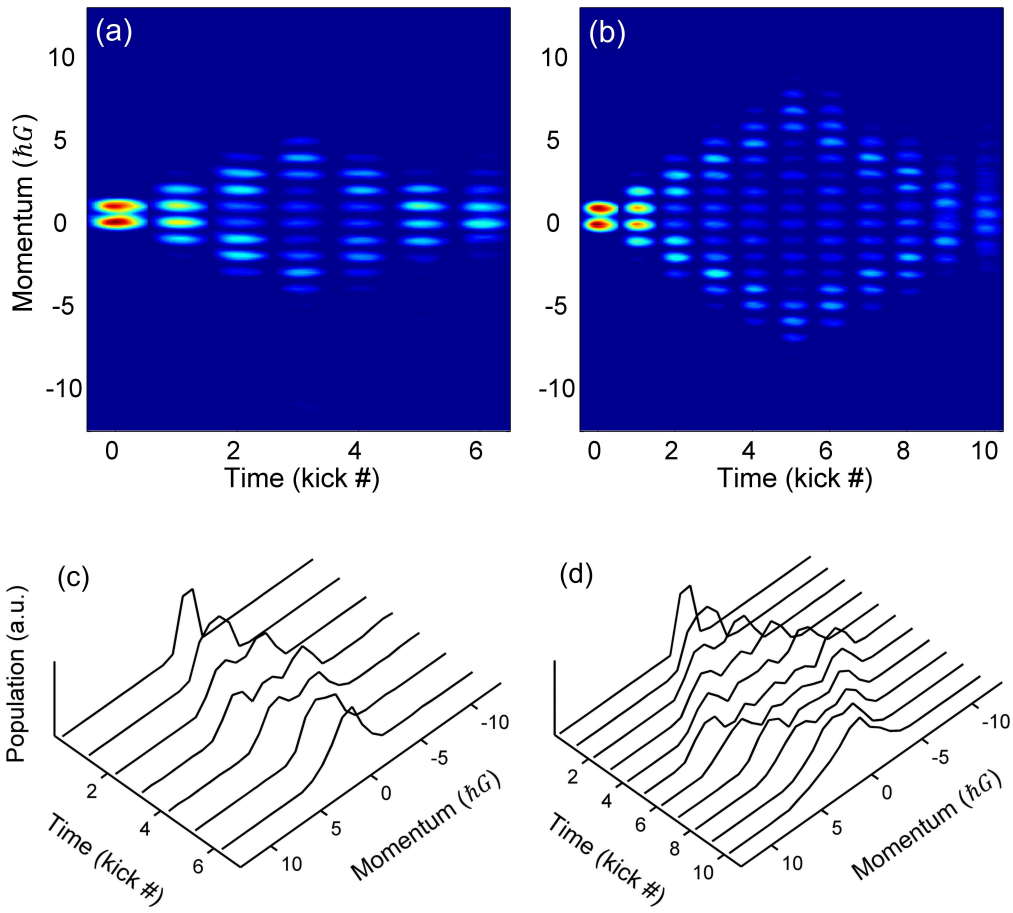

Figure 5.13: Ratchet reversals implemented with 6 (a,c) and 10 (b,d) total number of steps ($|k| = 1.45$). Due to the BEC quasimomentum which results in a dephasing of the system, the full recovery of the initial state is not possible. This effect gets more prominent at higher number of steps as can be seen by comparing the final momentum distributions of the two cases.

ones, one can find out the contribution of quasimomentum to the BEC.

5.4 Quantum-to-Classical Transition

The transition of quantum to classical behavior was another interesting aspect that we studied in our momentum-based walks. We investigated this transition, which is in principle manifested by the appearance of a Gaussian distribution around zero momentum (see Section 3.1.1) by adding noise to the system. More specifically, we achieved this via randomizing the mixing between the two internal states during each coin toss by adding a uniformly-distributed random phase to the fixed phase of the MW pulses.

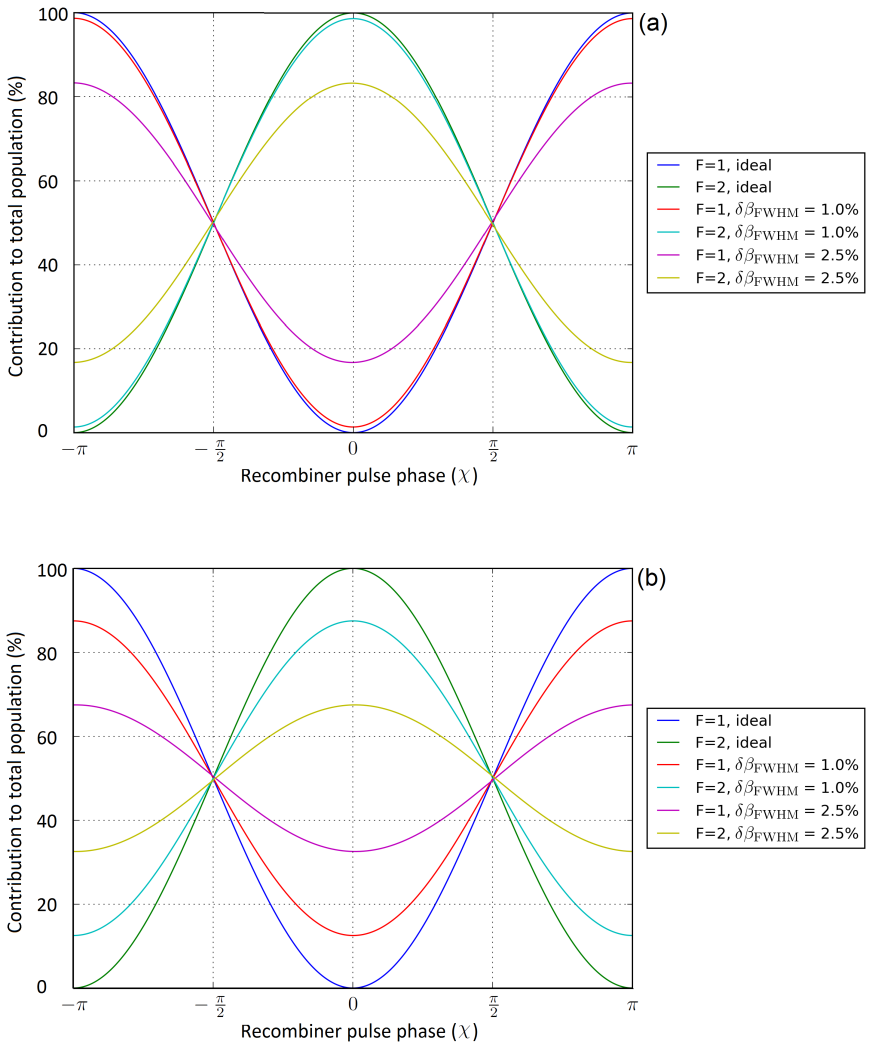

Figure 5.14: Simulated final populations of both internal states versus the phase of the recombiner pulse at the end of the ratchet reversals with 6 (a) and 10 (b) total number steps. Graphs are plotted for various amounts of quasimomenta, $\delta\beta_{\mathrm{FWHM}}$. The visibility of the oscillations reduces with the number of steps as well as the contributions of the quasimomenta to the BEC; the narrower the BEC (in momentum space), the more successful recovery of the initial state at the end of process [97].

Figure 5.15 demonstrates our experimental implementation of the quantum-to-classical transition for several different amounts of coin toss phase randomness; Figures 5.15.a, e represent the previously introduced fully unbiased quantum walk with the characteristic standard deviation of the momentum distribution $\propto j$. This was conducted by keeping the coin toss phases fixed at $\chi = -\pi/2$ and with $|k| = 1.45$. As can be seen in Figures 5.15.b, f, the classical walk starts to emerge by adding as little as 8% randomness to these phases. Note how the ballistic peaks become less prominent after a few steps and that a Gaussian-like peak starts to emerge in the center. The walk becomes predominantly classical with no quantum walk ballistic peaks at 20% phase randomness (Figures 5.15.c, g) and fully classical (Figures 5.15.d, h) with the characteristic momentum standard deviation growing as $\propto\sqrt{j}$ (not shown here) when the phase is randomized within a full 2π.

Figure 5.16.a summarizes this complete transition by illustrating the momentum distributions at the 8^{th} step of the walk: The disappearance of the quantum walk peaks and emergence of a classical Gaussian-like peak is quite clear. In addition, as seen in Figure 5.16.b, with larger amounts of phase randomness the mean energy of the system grows at a slower rate and displays behavior characteristic of a classical walk.

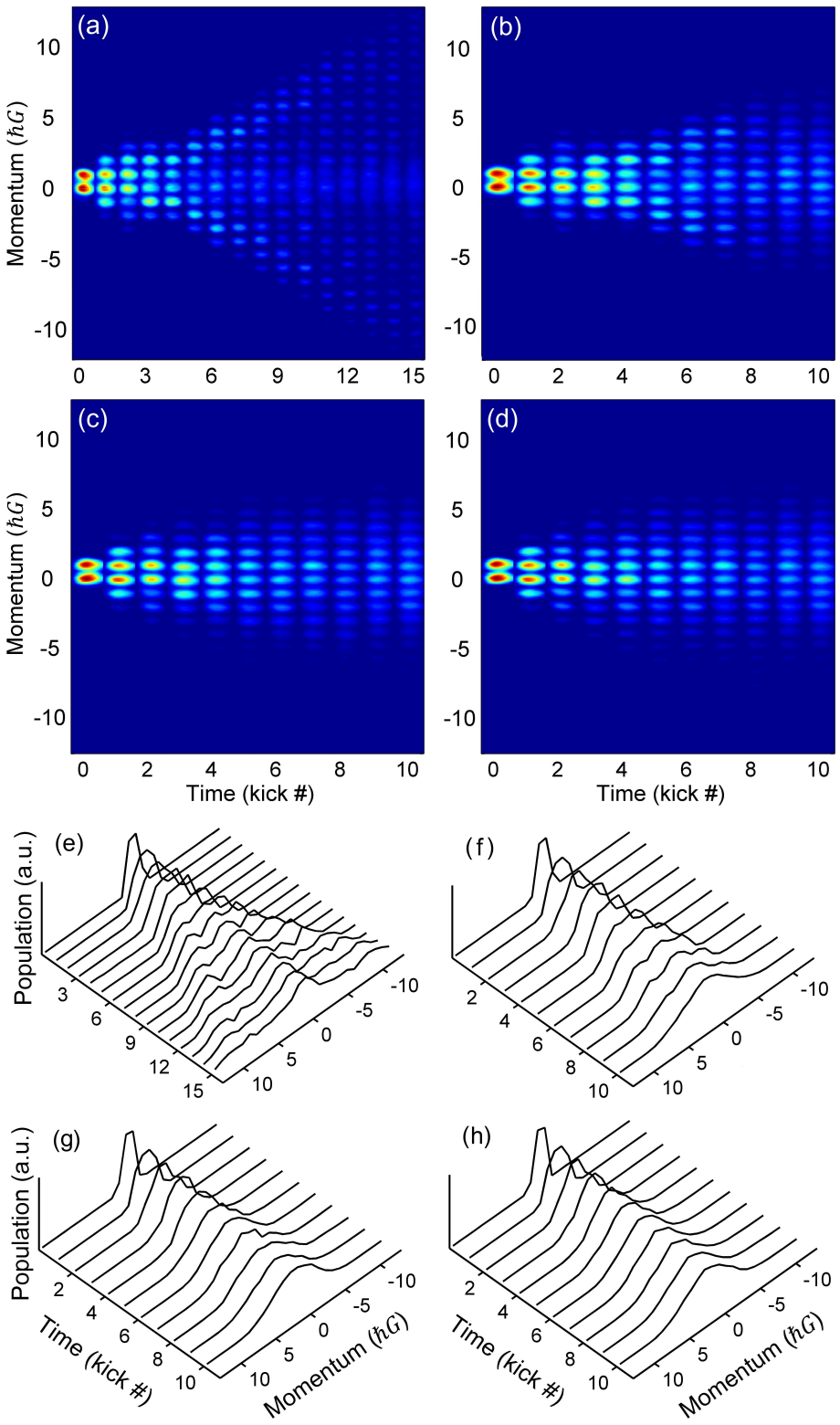

Figure 5.15: Quantum-to-classical transition as a result of enhancing the noise (coin toss phase randomness). Panels (a,e) show the standard quantum walk with $|k| = 1.45$ conducted with a fixed coin toss phase. Signatures of a classical walk emerge at 8% phase randomness (b,f). The walk becomes dominantly classical when randomizing the phase by 20% (c,g), and turns into fully classical when the phase is allowed to vary randomly within 2π (d,h).

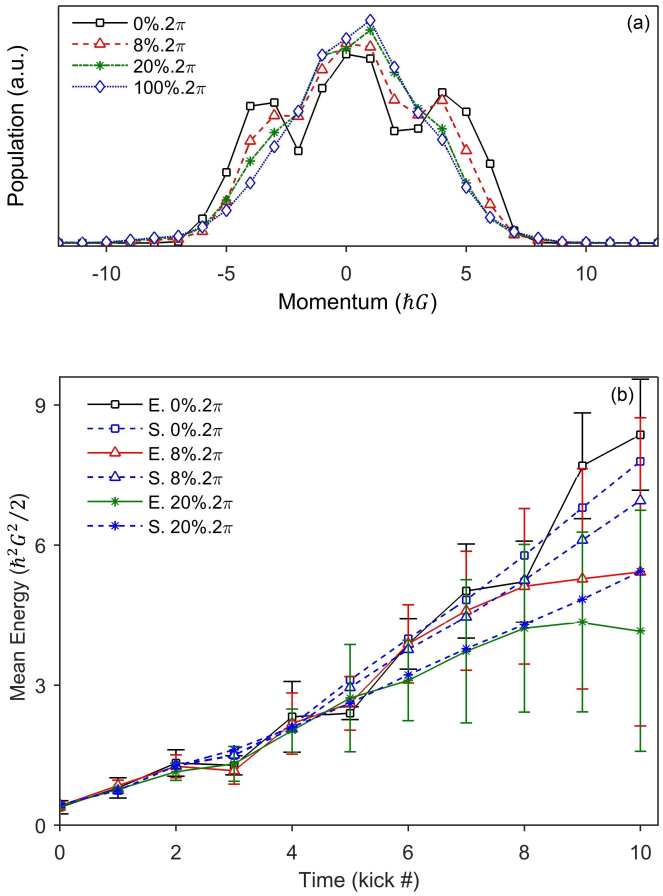

Figure 5.16: Signatures of quantum-to-classical transition; Panel (a) shows the evolution of momentum distribution pattern at the 8^{th} step of the walk as a result of enhancing the phase randomness. The corresponding mean energy variations are shown in panel (b).

Chapter 6

Conclusion

We have reported on the realization of a fully controllable discrete-time quantum walk in momentum space with ultra-cold ^{87}Rb atoms. This walk was an adoption of the discrete-time classical walk into the quantum regime, and hence it consisted of two degrees of freedom; a space in which the walk takes place, and a coin which selects the path of the system through the walk space. We realized the former by using a quantum resonant ratchet in momentum space and the latter by using the internal states of the atoms that determined the direction of the walk at each step. In Chapter 3 we described in detail how we realized the coin operators by manipulating the ^{87}Rb ground hyperfine levels with MW pulses. We also elaborated the shift operator of the walk that was a quantum resonant ratchet derived from the AOKR. Our quantum walk provided a straightforward and independent access to both internal and external degrees of freedom of the walker.

Our quantum coin operator produced a superposition of two (internal) states that caused an entanglement between the internal and external degrees of freedom. We showed how the quantum walk can be heavily affected by this entanglement leading to interference between the multitude of paths that the walker can take in the walk space. In Chapter 5 we showed how this interference results in a quantum walk manifested by a pair of ballistically diverging peaks which differentiates the probability distribution of this walk from the slowly-varying Gaussian distribution of a classical walk.

With our present setup, we could experimentally implement quantum walks up to 20 steps. This range was sufficiently large to observe the quantum walk and investigate different features of it as described in detail in Chapter 5. In Section 5.1 we demonstrated the effects of ratchet strength on the characteristics of a standard quantum walk and showed how the speed and stability of the walk

can change by varying this parameter. We also described theoretically and experimentally how the coin choice can change the symmetry of the walk. Following in the same section we investigated the effects of several parameters on the qualitative features of the walk. These parameters were the global phase introduced by the DC component of the optical standing wave, number of momentum classes contributing to the initial state, BEC thermal cloud and quasimomentum, and the spontaneous emission.

In Section 5.2 we demonstrated the realization of the steered quantum walks using biased coins or biased ratchets. In the former, we constantly applied biased MW coin operators that gave unequal superpositions of the internal states at each step. This caused a preferred direction for the atoms after each coin toss that eventually led to an asymmetric walk, the direction and speed of which were determined by the bias factor of the coins. On the other hand, we realized the latter via the use of non-symmetric walk steps. We achieved these biased ratchets by detuning the kicking laser frequency, so that unequal kicking strengths were obtained at the shift operators addressing either internal state. This caused the walk's left or right shifts not to be identical, as opposed to a symmetric walk achieved with unbiased ratchets. One can use these features to steer the walk in the desired direction or to compensate for the probable biases in the dynamics of the quantum transport.

We also investigated the reversability as another control feature of our quantum walks in Section 5.3. We analytically proved that the quantum walks, due to the unitary nature of their operators, can be reversed at any step by applying the Hermitian conjugates of the coin and shift operators to recover the initial state. Our experimental results were in excellent agreement with the simulations and we observed that the extent of the initial state recovery strongly depends of the BEC quasimomentum and thermal cloud. In addition, we showed how a regular bidirectional ratchet can be more straightforwardly reversed to retrieve the initial state and proposed the use of walk or ratchet reversals as sensitive detectors in atom interferometry applications [26, 27, 33, 58, 59, 100].

Quantum-to-classical transition was another aspect of the walk that we investigated in our scheme. We demonstrated the gradual transition of the walk from fully quantum, manifested by diverging momentum currents, to fully classical with a Gaussian momentum distribution. We achieved this by introducing a certain amount of noise to the phase of the coin operators at each step and highlighted the noise range in which the ballistic peaks of quantum walk become less prominent and a classical walk starts to emerge in the center of the momentum space. We showed that, as the walk becomes more classical, the energy of the system grows at a slower rate, verifying that the information transfer in quantum walk is

faster than in its classical version [3, 11].

Our scheme had several other advantages with respect to previous implementations of a quantum walk. In contrast to previous works, our quantum walk is realized using a BEC that allows for investigating the quantum walks with many-body correlations [14, 18, 101, 102, 103, 104]. Further applications in driven walks [56, 57] and quantum algorithms, e.g. searches of marked momentum states, as in [60] but by adjusting the coin degree, seem possible. Another promising application of our quantum walks relates to the observation of topological phases [62, 63] and systems that can simulate the integer quantum hall effect [105]. Finally, as a result of the fact that the quantum walk takes place in momentum space [51, 58, 59], our walk should also be readily extendable to higher dimensions [60, 106, 107] to implement the multi-dimensional walks.

Bibliography

[1] R. P. Feynman, "Simulating physics with computers," *International journal of theoretical physics*, vol. 21, no. 6-7, pp. 467–488, 1982.

[2] M. A. Nielsen and I. L. Chuang, *Quantum computation and quantum information*. Cambridge university press, 2010.

[3] P. W. Shor, "Algorithms for quantum computation: Discrete logarithms and factoring," in *Foundations of Computer Science, 1994 Proceedings., 35th Annual Symposium on*, pp. 124–134, Ieee, 1994.

[4] B. C. Travaglione and G. J. Milburn, "Implementing the quantum random walk," *Physical Review A*, vol. 65, no. 3, p. 032310, 2002.

[5] L. K. Grover, "Quantum mechanics helps in searching for a needle in a haystack," *Physical review letters*, vol. 79, no. 2, p. 325, 1997.

[6] T. Yamasaki, H. Kobayashi, and H. Imai, "An analysis of absorbing times of quantum walks," in *Unconventional Models of Computation*, pp. 315–329, Springer, 2002.

[7] J. Kempe, "Discrete quantum walks hit exponentially faster," *Probability theory and related fields*, vol. 133, no. 2, pp. 215–235, 2005.

[8] W. Paul and J. Baschnagel, *Stochastic processes*. Springer, 2013.

[9] N. G. Van Kampen, *Stochastic processes in physics and chemistry*, vol. 1. Elsevier, 1992.

[10] M. N. Barber and B. W. Ninham, *Random and restricted walks: Theory and applications*, vol. 10. CRC Press, 1970.

[11] Y. Aharonov, L. Davidovich, and N. Zagury, "Quantum random walks," *Physical Review A*, vol. 48, no. 2, p. 1687, 1993.

[12] E. Farhi and S. Gutmann, "Quantum computation and decision trees," *Physical Review A*, vol. 58, no. 2, p. 915, 1998.

[13] J. Kempe, "Quantum random walks: an introductory overview," *Contemporary Physics*, vol. 44, no. 4, pp. 307–327, 2003.

[14] P. M. Preiss, R. Ma, M. E. Tai, A. Lukin, M. Rispoli, P. Zupancic, Y. Lahini, R. Islam, and M. Greiner, "Strongly correlated quantum walks in optical lattices," *Science*, vol. 347, no. 6227, pp. 1229–1233, 2015.

[15] S. E. Venegas-Andraca, "Quantum walks: a comprehensive review," *Quantum Information Processing*, vol. 11, no. 5, pp. 1015–1106, 2012.

[16] N. Shenvi, J. Kempe, and K. B. Whaley, "Quantum random-walk search algorithm," *Physical Review A*, vol. 67, no. 5, p. 052307, 2003.

[17] A. M. Childs, "Universal computation by quantum walk," *Physical review letters*, vol. 102, no. 18, p. 180501, 2009.

[18] A. M. Childs, D. Gosset, and Z. Webb, "Universal computation by multiparticle quantum walk," *Science*, vol. 339, no. 6121, pp. 791–794, 2013.

[19] A. M. Childs, R. Cleve, E. Deotto, E. Farhi, S. Gutmann, and D. A. Spielman, "Exponential algorithmic speedup by a quantum walk," in *Proceedings of the thirty-fifth annual ACM symposium on Theory of computing*, pp. 59–68, ACM, 2003.

[20] A. M. Childs and J. Goldstone, "Spatial search by quantum walk," *Physical Review A*, vol. 70, no. 2, p. 022314, 2004.

[21] A. Ambainis, J. Kempe, and A. Rivosh, "Proceedings of the sixteenth annual acm-siam symposium on discrete algorithms," 2005.

[22] A. Ambainis, E. Bach, A. Nayak, A. Vishwanath, and J. Watrous, "One-dimensional quantum walks," in *Proceedings of the thirty-third annual ACM symposium on Theory of computing*, pp. 37–49, ACM, 2001.

[23] G. Summy and S. Wimberger, "Quantum random walk of a bose-einstein condensate in momentum space," *Physical Review A*, vol. 93, no. 2, p. 023638, 2016.

[24] W. Dür, R. Raussendorf, V. M. Kendon, and H.-J. Briegel, "Quantum walks in optical lattices," *Physical Review A*, vol. 66, no. 5, p. 052319, 2002.

[25] K. Eckert, J. Mompart, G. Birkl, and M. Lewenstein, "One-and two-dimensional quantum walks in arrays of optical traps," *Physical Review A*, vol. 72, no. 1, p. 012327, 2005.

[26] A. Steffen, A. Alberti, W. Alt, N. Belmechri, S. Hild, M. Karski, A. Widera, and D. Meschede, "Digital atom interferometer with single particle control on a discretized space-time geometry," *Proceedings of the National Academy of Sciences*, vol. 109, no. 25, pp. 9770–9774, 2012.

[27] T. Groh, S. Brakhane, W. Alt, D. Meschede, J. K. Asbóth, and A. Alberti, "Robustness of topologically protected edge states in quantum walk experiments with neutral atoms," *Physical Review A*, vol. 94, no. 1, p. 013620, 2016.

[28] M. Karski, L. Förster, J.-M. Choi, A. Steffen, W. Alt, D. Meschede, and A. Widera, "Quantum walk in position space with single optically trapped atoms," *Science*, vol. 325, no. 5937, pp. 174–177, 2009.

[29] C. Chandrashekar, "Implementing the one-dimensional quantum (hadamard) walk using a bose-einstein condensate," *Physical Review A*, vol. 74, no. 3, p. 032307, 2006.

[30] F. Zähringer, G. Kirchmair, R. Gerritsma, E. Solano, R. Blatt, and C. Roos, "Realization of a quantum walk with one and two trapped ions," *Physical review letters*, vol. 104, no. 10, p. 100503, 2010.

[31] H. Schmitz, R. Matjeschk, C. Schneider, J. Glueckert, M. Enderlein, T. Huber, and T. Schaetz, "Quantum walk of a trapped ion in phase space," *Physical review letters*, vol. 103, no. 9, p. 090504, 2009.

[32] D. J. Wineland, C. Monroe, W. M. Itano, D. Leibfried, B. E. King, and D. M. Meekhof, "Experimental issues in coherent quantum-state manipulation of trapped atomic ions," *Journal of Research of the National Institute of Standards and Technology*, vol. 103, no. 3, p. 259, 1998.

[33] F. Cardano, A. D'Errico, A. Dauphin, M. Maffei, B. Piccirillo, C. de Lisio, G. De Filippis, V. Cataudella, E. Santamato, L. Marrucci, *et al.*, "Detection of zak phases and topological invariants in a chiral quantum walk of twisted photons," *Nature communications*, vol. 8, p. 15516, 2017.

[34] H. B. Perets, Y. Lahini, F. Pozzi, M. Sorel, R. Morandotti, and Y. Silberberg, "Realization of quantum walks with negligible decoherence in waveguide lattices," *Physical review letters*, vol. 100, no. 17, p. 170506, 2008.

[35] M. A. Broome, A. Fedrizzi, B. P. Lanyon, I. Kassal, A. Aspuru-Guzik, and A. G. White, "Discrete single-photon quantum walks with tunable decoherence," *Physical review letters*, vol. 104, no. 15, p. 153602, 2010.

[36] A. Peruzzo, M. Lobino, J. C. Matthews, N. Matsuda, A. Politi, K. Poulios, X.-Q. Zhou, Y. Lahini, N. Ismail, K. Wörhoff, *et al.*, "Quantum walks of correlated photons," *Science*, vol. 329, no. 5998, pp. 1500–1503, 2010.

[37] Z. Bian, J. Li, H. Qin, X. Zhan, R. Zhang, B. C. Sanders, and P. Xue, "Realization of single-qubit positive-operator-valued measurement via a one-dimensional photonic quantum walk," *Physical review letters*, vol. 114, no. 20, p. 203602, 2015.

[38] J. O. Owens, M. A. Broome, D. N. Biggerstaff, M. E. Goggin, A. Fedrizzi, T. Linjordet, M. Ams, G. D. Marshall, J. Twamley, M. J. Withford, *et al.*, "Two-photon quantum walks in an elliptical direct-write waveguide array," *New Journal of Physics*, vol. 13, no. 7, p. 075003, 2011.

[39] A. Schreiber, K. N. Cassemiro, V. Potoček, A. Gábris, P. J. Mosley, E. Andersson, I. Jex, and C. Silberhorn, "Photons walking the line: a quantum walk with adjustable coin operations," *Physical review letters*, vol. 104, no. 5, p. 050502, 2010.

[40] A. Schreiber, K. Cassemiro, V. Potoček, A. Gábris, I. Jex, and C. Silberhorn, "Decoherence and disorder in quantum walks: from ballistic spread to localization," *Physical review letters*, vol. 106, no. 18, p. 180403, 2011.

[41] M. G. Raizen, "Quantum chaos with cold atoms," *Advances in Atomic, Molecular, and Optical Physics*, vol. 41, no. 43, p. 199, 1999.

[42] B. G. Klappauf, W. H. Oskay, D. A. Steck, and M. G. Raizen, "Observation of noise and dissipation effects on dynamical localization," *Physical review letters*, vol. 81, no. 6, p. 1203, 1998.

[43] H. Ammann, R. Gray, I. Shvarchuck, and N. Christensen, "Quantum delta-kicked rotor: Experimental observation of decoherence," *Physical review letters*, vol. 80, no. 19, p. 4111, 1998.

[44] G. Behinaein, V. Ramareddy, P. Ahmadi, and G. S. Summy, "Exploring the phase space of the quantum δ-kicked accelerator," *Physical review letters*, vol. 97, no. 24, p. 244101, 2006.

[45] I. Dana, V. Ramareddy, I. Talukdar, and G. S. Summy, "Experimental realization of quantum-resonance ratchets at arbitrary quasimomenta," *Physical review letters*, vol. 100, no. 2, p. 024103, 2008.

[46] I. Talukdar, R. Shrestha, and G. Summy, "Sub-fourier characteristics of a δ-kicked-rotor resonance," *Physical review letters*, vol. 105, no. 5, p. 054103, 2010.

[47] R. Shrestha, J. Ni, W. Lam, S. Wimberger, and G. Summy, "Controlling the momentum current of an off-resonant ratchet," *Physical Review A*, vol. 86, no. 4, p. 043617, 2012.

[48] R. Shrestha, J. Ni, W. Lam, G. Summy, and S. Wimberger, "Dynamical tunneling of a bose-einstein condensate in periodically driven systems," *Physical Review E*, vol. 88, no. 3, p. 034901, 2013.

[49] R. Shrestha, S. Wimberger, J. Ni, W. Lam, and G. Summy, "Fidelity of the quantum δ-kicked accelerator," *Physical Review E*, vol. 87, no. 2, p. 020902, 2013.

[50] J. Ni, W. K. Lam, S. Dadras, M. F. Borunda, S. Wimberger, and G. S. Summy, "Initial-state dependence of a quantum resonance ratchet," *Physical Review A*, vol. 94, no. 4, p. 043620, 2016.

[51] J. Ni, S. Dadras, W. K. Lam, R. K. Shrestha, M. Sadgrove, S. Wimberger, and G. S. Summy, "Hamiltonian ratchets with ultra-cold atoms," *Annalen der Physik*, vol. 529, no. 8, 2017.

[52] S. Dadras, A. Gresch, C. Groiseau, S. Wimberger, and G. S. Summy, "Realization of a quantum walk in momentum space with a bose-einstein condensate," *arXiv preprint arXiv:1802.08160*, 2018.

[53] T. A. Brun, H. A. Carteret, and A. Ambainis, "Quantum to classical transition for random walks," *Physical review letters*, vol. 91, no. 13, p. 130602, 2003.

[54] M. Nizama and M. O. Cáceres, "Non-equilibrium transition from dissipative quantum walk to classical random walk," *Journal of Physics A: Mathematical and Theoretical*, vol. 45, no. 33, p. 335303, 2012.

[55] M. Weiß, C. Groiseau, W. Lam, R. Burioni, A. Vezzani, G. S. Summy, and S. Wimberger, "Steering random walks with kicked ultracold atoms," *Physical Review A*, vol. 92, no. 3, p. 033606, 2015.

[56] D. Witthaut, "Quantum walks and quantum simulations with bloch-oscillating spinor atoms," *Physical Review A*, vol. 82, no. 3, p. 033602, 2010.

[57] C. S. Hamilton, S. Barkhofen, L. Sansoni, I. Jex, and C. Silberhorn, "Driven discrete time quantum walks," *New Journal of Physics*, vol. 18, no. 7, p. 073008, 2016.

[58] T. Kovachy, P. Asenbaum, C. Overstreet, C. Donnelly, S. Dickerson, A. Sugarbaker, J. Hogan, and M. Kasevich, "Quantum superposition at the half-metre scale," *Nature*, vol. 528, no. 7583, p. 530, 2015.

[59] H. Ahlers, H. Müntinga, A. Wenzlawski, M. Krutzik, G. Tackmann, S. Abend, N. Gaaloul, E. Giese, A. Roura, R. Kuhl, *et al.*, "Double bragg interferometry," *Physical review letters*, vol. 116, no. 17, p. 173601, 2016.

[60] M. Sadgrove, S. Wimberger, and K. Nakagawa, "Phase-selected momentum transport in ultracold atoms," *The European Physical Journal D*, vol. 66, no. 6, p. 155, 2012.

[61] P. R. Giri and V. E. Korepin, "A review on quantum search algorithms," *Quantum Information Processing*, vol. 16, no. 12, p. 315, 2017.

[62] L. Zhou and J. Gong, "Floquet topological phases in a spin-1/2 double kicked rotor," *arXiv preprint arXiv:1803.00350*, 2018.

[63] T. Kitagawa, M. S. Rudner, E. Berg, and E. Demler, "Exploring topological phases with quantum walks," *Physical Review A*, vol. 82, no. 3, p. 033429, 2010.

[64] W. Pauli, "Exclusion principle and quantum mechanics," in *Writings on Physics and Philosophy*, pp. 165–181, Springer, 1994.

[65] H. J. Metcalf and P. Van der Straten, *Laser cooling and trapping of neutral atoms*. Wiley Online Library, 2007.

[66] M. Ueda, *Fundamentals and new frontiers of Bose-Einstein condensation*. World Scientific, 2010.

[67] K. Huang, "Statistical mechanics, 2nd," *Edition (New York: John Wiley & Sons)*, 1987.

[68] L. Allen and J. H. Eberly, *Optical resonance and two-level atoms*. Courier Corporation, 1975.

[69] P. F. Bernath, *Spectra of atoms and molecules*. Oxford University Press, 2015.

[70] S. Chu, L. Hollberg, J. E. Bjorkholm, A. Cable, and A. Ashkin, "Three-dimensional viscous confinement and cooling of atoms by resonance radiation pressure," *Physical review letters*, vol. 55, no. 1, p. 48, 1985.

[71] D. A. Steck, "Rubidium 87 d line data," 2001.

[72] R. K. Shrestha, *Applications of the atom-optical kicked rotor*. PhD thesis, Oklahoma State University, 2013.

[73] J. Dalibard and C. Cohen-Tannoudji, "Laser cooling below the doppler limit by polarization gradients: simple theoretical models," *JOSA B*, vol. 6, no. 11, pp. 2023–2045, 1989.

[74] E. Raab, M. Prentiss, A. Cable, S. Chu, and D. E. Pritchard, "Trapping of neutral sodium atoms with radiation pressure," *Physical Review Letters*, vol. 59, no. 23, p. 2631, 1987.

[75] H. F. Hess, "Evaporative cooling of magnetically trapped and compressed spin-polarized hydrogen," *Physical Review B*, vol. 34, no. 5, p. 3476, 1986.

[76] J. Miller, R. Cline, and D. Heinzen, "Far-off-resonance optical trapping of atoms," *Physical Review A*, vol. 47, no. 6, p. R4567, 1993.

[77] A. Nayak and A. Vishwanath, "Quantum walk on the line," *arXiv preprint quant-ph/0010117*, 2000.

[78] D. Aharonov, A. Ambainis, J. Kempe, and U. Vazirani, "Quantum walks on graphs," in *Proceedings of the thirty-third annual ACM symposium on Theory of computing*, pp. 50–59, ACM, 2001.

[79] A. Waxman, "Coherent manipulations of the rubidium atom ground state," Master's thesis, Ben Gurion University, 2008.

[80] R. W. Boyd, *Nonlinear optics*. Academic press, 2003.

[81] S. Kuhr *et al.*, *A controlled quantum system of individual neutral atoms*. PhD thesis, Universitäts- und Landesbibliothek Bonn, 2003.

[82] M. Sadgrove, M. Horikoshi, T. Sekimura, and K. Nakagawa, "Rectified momentum transport for a kicked bose-einstein condensate," *Physical review letters*, vol. 99, no. 4, p. 043002, 2007.

[83] M. Sadgrove and S. Wimberger, "A pseudoclassical method for the atom-optics kicked rotor: from theory to experiment and back," in *Advances in Atomic, Molecular, and Optical Physics*, vol. 60, pp. 315–369, Elsevier, 2011.

[84] R. Gommers, S. Denisov, and F. Renzoni, "Quasiperiodically driven ratchets for cold atoms," *Physical review letters*, vol. 96, no. 24, p. 240604, 2006.

[85] F. M. Izrailev, "Simple models of quantum chaos: spectrum and eigenfunctions," *Physics Reports*, vol. 196, no. 5-6, pp. 299–392, 1990.

[86] M. C. Gutzwiller, *Chaos in classical and quantum mechanics*, vol. 1. Springer Science & Business Media, 2013.

[87] B. V. Chirikov, "A universal instability of many-dimensional oscillator systems," *Physics reports*, vol. 52, no. 5, pp. 263–379, 1979.

[88] H. F. Talbot, "Lxxvi. facts relating to optical science. no. iv," *The London and Edinburgh Philosophical Magazine and Journal of Science*, vol. 9, no. 56, pp. 401–407, 1836.

[89] C. Kittel, P. McEuen, and P. McEuen, *Introduction to solid state physics*, vol. 8. Wiley New York, 1996.

[90] P. L. Gould, G. A. Ruff, and D. E. Pritchard, "Diffraction of atoms by light: The near-resonant kapitza-dirac effect," *Physical review letters*, vol. 56, no. 8, p. 827, 1986.

[91] A. Derevianko and H. Katori, "Colloquium: Physics of optical lattice clocks," *Reviews of Modern Physics*, vol. 83, no. 2, p. 331, 2011.

[92] L. Deng, E. W. Hagley, J. Denschlag, J. Simsarian, M. Edwards, C. W. Clark, K. Helmerson, S. Rolston, and W. D. Phillips, "Temporal, matter-wave-dispersion talbot effect," *Physical Review Letters*, vol. 83, no. 26, p. 5407, 1999.

[93] M. Lepers, V. Zehnlé, and J. C. Garreau, "Kicked-rotor quantum resonances in position space," *Physical Review A*, vol. 77, no. 4, p. 043628, 2008.

[94] S. Wimberger, I. Guarneri, and S. Fishman, "Quantum resonances and decoherence for δ-kicked atoms," *Nonlinearity*, vol. 16, no. 4, p. 1381, 2003.

[95] M. Sadgrove and S. Wimberger, "Pseudo-classical theory for directed transport at quantum resonance," *New Journal of Physics*, vol. 11, no. 8, p. 083027, 2009.

[96] C. Groiseau, "Discrete-time quantum walks in momentum space," Master's thesis, University of Heidelberg, 2017.

[97] A. Gresch, "The quasi-momentum in an experimentally implemented quantum walk," Master's thesis, University of Heidelberg, 2017.

[98] S. Kuppens, K. Corwin, K. Miller, T. Chupp, and C. Wieman, "Loading an optical dipole trap," *Physical review A*, vol. 62, no. 1, p. 013406, 2000.

[99] K. Mølmer, Y. Castin, and J. Dalibard, "Monte carlo wave-function method in quantum optics," *JOSA B*, vol. 10, no. 3, pp. 524–538, 1993.

[100] A. D. Cronin, J. Schmiedmayer, and D. E. Pritchard, "Optics and interferometry with atoms and molecules," *Reviews of Modern Physics*, vol. 81, no. 3, p. 1051, 2009.

[101] L. Sansoni, F. Sciarrino, G. Vallone, P. Mataloni, A. Crespi, R. Ramponi, and R. Osellame, "Two-particle bosonic-fermionic quantum walk via integrated photonics," *Physical review letters*, vol. 108, no. 1, p. 010502, 2012.

[102] A. Schreiber, A. Gábris, P. P. Rohde, K. Laiho, M. Štefaňák, V. Potoček, C. Hamilton, I. Jex, and C. Silberhorn, "A 2d quantum walk simulation of two-particle dynamics," *Science*, vol. 336, no. 6077, pp. 55–58, 2012.

[103] J. D. Meinecke, K. Poulios, A. Politi, J. C. Matthews, A. Peruzzo, N. Ismail, K. Wörhoff, J. L. O'Brien, and M. G. Thompson, "Coherent time evolution and boundary conditions of two-photon quantum walks in waveguide arrays," *Physical Review A*, vol. 88, no. 1, p. 012308, 2013.

[104] D. Morita, T. Kubo, Y. Tokura, and M. Yamashita, "Spin-1 quantum walks," *Physical Review A*, vol. 93, no. 6, p. 063625, 2016.

[105] Y. Chen and C. Tian, "Planck's quantum-driven integer quantum hall effect in chaos," *Physical review letters*, vol. 113, no. 21, p. 216802, 2014.

[106] M. Gräfe, A. Solntsev, R. Keil, A. Sukhorukov, M. Heinrich, A. Tünnermann, S. Nolte, A. Szameit, and Y. S. Kivshar, "Biphoton generation in quadratic waveguide arrays: A classical optical simulation," *Scientific Reports*, vol. 2, p. 562, 2012.

[107] K. Poulios, R. Keil, D. Fry, J. D. Meinecke, J. C. Matthews, A. Politi, M. Lobino, M. Gräfe, M. Heinrich, S. Nolte, *et al.*, "Quantum walks of correlated photon pairs in two-dimensional waveguide arrays," *Physical review letters*, vol. 112, no. 14, p. 143604, 2014.

VITA

SIAMAK DADRASMARANI

Candidate for the Degree of

Doctor of Philosophy

Dissertation:

DISCRETE-TIME QUANTUM WALK OF A BOSE-EINSTEIN CONDENSATE IN MOMENTUM SPACE

Major Field:

PHOTONICS

Biographical:

Personal Data: Born in Tehran, IRAN on September 11, 1980.

Education:

Received the B.S. degree from K.N. Toosi University of Technology, Tehran, Iran, 2002, in Physics

Received the M.S. degree from Shahid Beheshti University, Tehran, Iran, 2005, in Photonics

Completed the requirements for the degree of Doctor of Philosophy with a major in Photonics from Oklahoma State University in May, 2018.

Experience:

Teaching/Research Assistant at Oklahoma State University, August 2012 - May 2018

Developed quantum random walk, quantum ratchet, and quantum fidelity experiments using ultra-cold rubidium-87 atoms

Improved all-optical atom cooling setup to enhance atomic population in the generated rubidium-87 Bose-Einstein condensate

Developed computer-controlled microwave pulse generator used in quantum random walk and quantum fidelity experiments

Mentored undergraduate and graduate students in Bose-Einstein Condensate and Quantum Chaos Research Group at OSU

Mentored undergraduate students in Physics-I laboratory at OSU